Two-Phase Flow In Microchannels:
Morphology And Interface Phenomena

By

Alexandru Herescu

A DISSERTATION

Submitted in partial fulfillment of the requirements for the degree of

DOCTOR OF PHILOSOPHY

In Mechanical Engineering – Engineering Mechanics

MICHIGAN TECHNOLOGICAL UNIVERSITY

2013

UMI Number: 3565323

UMI

Dissertation Publishing

UMI 3565323

ProQuest

www.manaraa.com

This dissertation has been approved in partial fulfillment of the requirements for the Degree of DOCTOR OF PHILOSOPHY in Mechanical Engineering – Engineering Mechanics.

Department of Mechanical Engineering – Engineering Mechanics

Dissertation Advisor: Dr. Jeffrey S. Allen

Committee Member: Dr. Amitabh Narain

Committee Member: Dr. DeSheng Meng

Committee Member: Dr. Robert Kolkka

Department Chair: Professor William W. Predebon

To my wonderful daughters, Ilinca and Mara

CONTENTS

ix

LIST OF FIGURES

xiv

LIST OF TABLES

PREFACE

Present manuscript includes a series of republished articles in the areas of micro-scale flow and capillary phenomena with application to fluid management in micro-systems. The author elaborated on these papers under the advice of Dr. Jeff Allen, listed as the second author. Introductory concepts and the interrelation between different aspects of capillary two-phase flow are discussed in the first chapter, *Introductory Notes*. The second chapter contains republished research which addresses fluid management issues in the gas flow channels of Proton Exchange Membrane fuel cells. The third chapter presents two-phase flow morphology investigated by high-speed microscopy, the two constitutive sections are separate papers reprinted by permission. *Section 4.2* of chapter four, republished, investigates the effects of surface wetting on two-phase flow in microchannels. Chapter five, reprinted, continues the investigation of micro-scale flow through film deposition experiments performed in wetting and non-wetting capillary tubes. Chapter six comprises of unpublished research targeting film deposition processes in non-wetting capillary tubes, and also investigates an interface phenomenon taking the form of a hydraulic jump in an annular liquid film.

ACKNOWLEDGMENTS

The support coming from my family is priceless. My wife Nicoleta has been always by my side all these years, my thanks and admiration go to her for her courage and endurance... I am grateful to my parents for their encouragement and support. My thoughts are always with those whom I owe so much but are no longer here, my grandparents and my aunt Adriana. *Non omnis moriar.*

Many thanks to my colleagues at the Microfluidics and Interfacial Transport Laboratory for their suggestions and support.

Nomenclature

GDL	Gas Diffusion Layer
PEM	Proton Exchange Membrane
$PEMFC$	PEM Fuel Cell
Bo	Bond number
c	Theoretical shock velocity
c^*	Critical shock velocity
Ca	Capillary number
Ca^*	Critical Capillary number
e	Meniscus film thickness
h	Film thickness
h_R	Non-dimensional film thickness
k	Meniscus curvature
l	Transitional meniscus length
L	Transition length
L_c	Capillary length
Ma	Mach number
Re	Reynolds number
R	Radius of capillary tube
U_S	Measured shock velocity
U	Meniscus velocity
U_{CL}	Contact line velocity
$U_{G,S}$	Gas superficial velocity
$U_{L,S}$	Liquid superficial velocity
V_2	Film velocity (adjacent to the ridge)
V_{CR}	Critical plug volume
We	Weber number

α	Channel bend dihedral
μ	Viscosity
ρ	Mass density
σ	Surface tension
θ	Contact angle
Subscripts	
wet	Wetting
$nonwet$	Non-wetting
R	Scaled by radius

ABSTRACT

The existence and morphology, as well as the dynamics of micro-scale gas liquid-interfaces is investigated numerically and experimentally. These studies can be used to assess liquid management issues in microsystems such as PEMFC gas flow channels, and are meant to open new research perspectives in two-phase flow, particularly in film deposition on non-wetting surfaces. For example the critical plug volume data can be used to deliver desired length plugs, or to determine the plug formation frequency. The dynamics of gas-liquid interfaces, of interest for applications involving small passages (e.g. heat exchangers, phase separators and filtration systems), was investigated using high-speed microscopy - a method that also proved useful for the study of film deposition processes.

The existence limit for a liquid plug forming in a mixed wetting channel is determined by numerical simulations using Surface Evolver. The plug model simulate actual conditions in the gas flow channels of PEM fuel cells, the wetting of the gas diffusion layer (GDL) side of the channel being different from the wetting of the bipolar plate walls. The minimum plug volume, denoted as critical volume is computed for a series of GDL and bipolar plate wetting properties. Critical volume data is meant to assist in the water management of PEMFC, when corroborated with experimental data. The effect of cross section geometry is assessed by computing the

critical volume in square and trapezoidal channels. Droplet simulations show that water can be passively removed from the GDL surface towards the bipolar plate if we take advantage on differing wetting properties between the two surfaces, to possibly avoid the gas transport blockage through the GDL.

High speed microscopy was employed in two-phase and film deposition experiments with water in round and square capillary tubes. Periodic interface destabilization was observed and the existence of compression waves in the gas phase is discussed by taking into consideration a naturally occurring convergent-divergent nozzle formed by the flowing liquid phase. The effect of channel geometry and wetting properties was investigated through two-phase water-air flow in square and round microchannels, having three static contact angles of 20°, 80° and 105°. Four different flow regimes are observed for a fixed flow rate, this being thought to be caused by the wetting behavior of liquid flowing in the corners as well as the liquid film stability. Film deposition experiments in wetting and non-wetting round microchannels show that a thicker film is deposited for wetting conditions departing from the ideal 0° contact angle. A film thickness dependence with the contact angle θ as well as the Capillary number in the form $h_R \approx Ca^{2/3}/cos\theta$ is inferred from scaling arguments, for contact angles smaller than 36°. Non-wetting film deposition experiments reveal that a film significantly thicker than the wetting Bretherton film is deposited. A hydraulic jump occurs if critical conditions are met, as given by a proposed non-dimensional parameter similar to the Froude number. Film thickness correlations are also found by matching the measured and the proposed velocity derived in the shock theory. The surface wetting as well as the presence of the shock cause morphological changes in the Taylor bubble flow.

1. Introductory Notes

Capillarity is omnipresent in nature, in rain drops, a foggy window or the ripples on the surface of a lake. The droplets hanging on the rails of my balcony will eventually fall when a certain volume of water is accumulated. But is it going to matter for the size of the falling drops if the rail is round or square, or if it is painted or not? The sciences that study capillarity examine the interface between a gas (vapor) and a liquid, or between two immiscible liquids. An interface, such as the surface of a hanging drop can be subjected to forces caused by an acceleration or a magnetic field, it deforms and takes a shape that corresponds to a state of minimum energy. Interfaces can become unstable under certain circumstances. Their behavior is of major importance to chemical industry or to soil science, to numerous engineering applications old and new.

Two phase flow, a gas or vapor flowing together with a liquid in a passage, is important to macro and micro-scale technologies such as fuel cells, heat exchangers, phase separators and bioreactors. These applications commonly incorporate multiple channels, complex flow paths or manifolds. Microscale applications, lab-on-chip technology and MEMS exhibit this type of flow. PEM fuel cells are macroscale applications which are dependent upon two-phase flow for effective water management of the product water. Coating industrial processes are based on capillary phenomena,

1

they require precise knowledge of the parameters controlling the film thickness which is also important in oil recovery. Challenges brought by miniaturization, the development of micro-scale technologies and a good amount of curiosity towards capillary phenomena constitute the sole motivation for this work, the expected result being more questions than answers.

1.1   Wetting, Microscale and Microchannels

Capillary phenomena are a consequence of an interface property, the *surface tension* σ, which is measured in units of N/m. In many situations the interface makes contact with a surface at a measurable angle, which is a property dependent on the surface tension and the energy of the solid surface. This angle is denoted as the *static contact angle* if the line of contact does not move, or *dynamic contact angle* otherwise. A defining length scale is the *capillary length*, or Laplace constant, $L_c = \sqrt{\sigma/\rho g}$. A channel having a characteristic length, typically the hydraulic diameter, smaller than the capillary length is regarded as a microchannel. A microchannel is a microscale or a capillary scale system, which is often defined by the Bond number Bo « 1, where Bo $= \rho g L^2/\sigma$. The type of wetting is specified by the contact angle θ, *perfect wetting* if $\theta = 0°$, *wetting* if $\theta < 90°$ or *non-wetting* if $\theta > 90°$.

1.2   Two-Phase Flow in Microchannels

Two-phase flows can be categorized in a number of *flow regimes* which attempt to group them into distinct morphological categories. The flow morphology can

change dramatically the way capillary scale devices operate and in spite of sustained research efforts it is still not well understood. The way a gas and a liquid occupy the space while they flow together through a microchannel is the result of a complex interaction between the two phases. The geometry and wetting properties of the channel are crucial to flow morphology as well as to the transition between flow regimes. The investigations presented throughout this work aim to characterize two-phase flow morphology and the behavior of the gas-liquid interface under various wetting conditions and geometries in microchannels.

Two-phase morphology is described in a variety of terminologies, which could be summarized as intermittent (plug/slug) flow, annular, bubbly, churn/dispersed rivulet/wavy and separated/stratified [3]. The existence of different morphologies is typically presented as two-phase flow maps having the gas and liquid superficial velocities ($U_{G,S}$, $U_{L,S}$) as abscissa and ordinate, respectively. The *superficial velocity* is defined as the volumetric flow rate divided by the cross-sectional area. There are numerous microchannel flow regime maps (Hassan, Damianides, Triplett, Coleman, Kawaji, Kawahara [1, 2, 9–12]) which attempt to give universal transition criteria using the classical macroscale parameters, the superficial velocities. These studies were not successful due to the fundamental differences between macroscale and interface dominated microscale flows. Other authors took a different approach using dimensional analysis to devise transition criteria (Waelchli, Tabatabai, Akbar [7, 13, 14]). Although these studies bring us closer to a physical understanding of capillary scale two-phase flow they cannot be extended to other cases. There is a need of fundamental knowledge of the interface behavior.

A *high-speed microscopy* experimental setting consisting of two setups is designed

3

and used for the purpose of two-phase characterization:(i) a two-phase setup with interface tracking and pressure measurements capability, and (ii) a film deposition setup with simultaneous interface tracking and liquid film thickness measurement capability. The visualization data is obtained via a high speed CMOS camera (Photron FASTCAM Ultima APX-RS) coupled to an inverted compound microscope (Nikon Eclipse TE-2000U) using an up to 20X objective and a 100 Watt halogen light source. The images are acquired at a rate of up to 15,000 frames per second with exposure times down to 1 μs. Both the high image acquisition rate and the low exposure time are crucial for successful interface tracking and morphological characterization of capillary scale phenomena which often span less than 1 ms. These setups were used for the investigations presented in *Chapters 3 - 6*.

A periodic flow regime characterized through liquid lobe formation and sudden collapse, as well as the effect of gas phase compressibility manifested through compression waves are presented in *Chapter 3*. Barajas and Panton[3]were the first to note a shift in the flow regime transition lines in round 1.6 mm diameter tubes as the contact angle is changed. Herescu and Allen[15] showed that the flow regime in square and round 0.5 mm tubes changes with the contact angle θ, four morphologies being observed at the same flow rate. These findings presented in *Chapter 4* prove that both cross-sectional geometry and contact angle change the flow morphology. This behavior is summarized in Figures 4.1 and 4.2, where experimental results from literature are grouped by geometry (round and square) and the transition lines are shown for different wetting cases (wetting $\theta < 45°$, intermediate wetting $45° < \theta < 90°$ and nonwetting $\theta > 90°$) .

4

1.3   Water Management in PEM Fuel Cells

PEM fuel cells operate by splitting hydrogen atoms into electrons and protons, the protons passing through a polymeric membrane to recombine with oxygen and produce water and heat. The membrane blocks the electrons which travel from the anode to the cathode generating electrical power. The Membrane Electrode Assembly (MEA) consists of a gas-diffusion anode, a proton-conducting membrane, and a gas-diffusion cathode. The MEA is placed between two plates, bipolar plates, which have embedded gas flow channels to allow for the transport of gas and water.

A balance must be achieved between water production and removal such that the membrane is hydrated while the passage of gases and water is not obstructed. Water may accumulate in the porous cathode and block the transport of oxygen to the membrane, a condition known as flooding. Liquid holdup is a condition which occurs when the gas flow channels become completely blocked due to water accumulation and represents an acknowledged barrier in the way of reliable PEM fuel cell development and the main motivation for the study presented in *Chapter 1*. The reader is referred to Bazylak, Mukundan [16, 17], and Trabold [18] for reviews of water visualization and quantification methods, as well as Li [19] for a summary of water management issues in PEM fuel cells.

The wetting properties play a major role in establishing the two-phase flow morphology in a microchannel of a given geometry. Experiments conducted by Owejan [20] concluded that the effect of flow field channel properties on water accumulation are important. They noted that a PTFE coated channel demonstrated smaller, more uniformly distributed liquid plugs when compared to an uncoated channel.

5

The better performance yielded by the non-wetting channel suggests the opportunity of further optimization through surface wettability and geometry manipulation. A better understanding of the static plug morphology can assist in the design and optimization of the gas flow channels. The minimum volume required to form a plug in a channel of mixed wettability, critical volume, is computed for a number of wetting configurations. The wetting properties of the GDL are different than those of the bipolar plate, the plug model presented in *Chapter 2* captures this configurations through numerical simulations using Surface Evolver [21]. The volumes can be further used for PEMFC development, when corroborated with experimental data. Additional simulations provide water management guidance showing how the water can be passively removed from the GDL to the channel walls by making use of differing surface wetting properties, to avoid the reactant gas transport blockage through the porous layer.

1.4   Film Deposition in Round Capillary Tubes

This topic is addressed in *Chapters 5 - 6.*

Finite length gas bubbles longer than the tube diameter alternating with liquid plugs is defined as plug flow. The study of the film deposition problem representing the infinite bubble case is a necessary step in understanding the interface behavior associated with the plug flow regime. Fairbrother and Stubbs[22] first noted that a bubble passing through a liquid-filled tube would move at a velocity higher than the average liquid velocity. Later on Landau, Levich[23] and Derjaguin[24] proposed a model for evaluating the thickness of a viscously deposited film as a

6

function of Capillary number ($Ca = \mu U/\sigma$). Bretherton[25] proposed a similar law for a film deposited inside a capillary, valid for thin films and Ca smaller than 0.005. He also found experimentally that aniline ($\theta_{\mathrm{aniline}} = 36°$) does not follow the predicted behavior and the deviation becomes increasingly important as the Capillary number decreases. Teletzke[26] proposed a theory which accounts for the conjoining/disjoining pressure potential to explain the behavior of films thinner than one micron. Aussillous and Quere[8] examined the role of inertia and extended Bretherton's law for higher Ca by matching own and Taylor's experimental data.

Snoeijer[27] showed recently that the thickness of a film coating a plate withdrawn from a liquid reservoir depends on surface wettability. He proved that the film thickness can have two solutions for the partial wetting case. Schwartz et. al.[28] examined the infinite and finite bubble in low Ca flow and found that the short bubble film obeys Bretherton's law while the long bubble film is almost twice as thick; for intermediate bubble length the film thickness presented multiple solutions possibly due to instabilities. Herescu and Allen[29] observed that the film thickness increases with the contact angle. Marangoni effects caused by contamination induced surface tension gradients was studied by Ratulowski[30], Ramdane and Quere [31] as well as Krechetnikov and Homsy [32], no general agreement exists concerning the thickening or thinning of the deposited film.

The results of film thickness deposition experiments in wetting and non-wetting capillary tubes, performed by means of high speed microscopy, are presented in *Chapter 5*. A scaling is proposed to account for the thicker film deposited on a partially wetting surface, a case generally not accounted for in classical film deposition which considers an infinite bubble with no influence from the trailing end of the film.

7

Film deposition experiments in non-wetting capillary tubes are performed in an attempt to understand unresolved issues with this process, as presented in Chapter 5. These results are discussed in *Chapter 6*, where a shock theory is developed and non-wetting film thickness correlations are proposed.

2. The Influence of Channel Wettability and Geometry on Water Plug Formation and Drop Location in a Proton Exchange Membrane Fuel Cell Flow Field

Chapter reprinted by permission.[*]

The critical volume of liquid water required to form a plug in a channel having mixed wettability similar to that found in the flow field of a proton exchange membrane (PEM) fuel cell is computed for a range of gas diffusion layer (GDL) and bipolar plate wettabilities and channel bend dihedral angles. Three gas diffusion layers (GDL) with 80, 110 and 150° contact angles are considered while the bipolar plate wettabilities are varied with static contact angles ranging from 50 to 130°. The critical volume is an intrinsic property of the channel-GDL configuration and has direct implications for the liquid holdup, the water distribution in the flow fields of

PEM fuel cells as well as on the pumping parasitic power loss. The plug volume correlations may be used as an optimization tool for water management in channels of mixed wettability. The effect of cross-section geometry on the critical volume is also investigated through a comparison between a square and a trapezoidal channel. Mixed wettability drop simulations reveal that water can be passively removed from the GDL surface to the bipolar plate if the latter has a lower contact angle, potentially avoiding the flooding of the porous electrodes.

2.1   Introduction

Proton Exchange Membrane (PEM) fuel cells convert chemical energy into electrical energy through an electrochemical reaction between hydrogen and air. Protons resulting from the oxidation of hydrogen pass from the anode through a polymeric membrane to the cathode and combine with oxygen to produce water and heat. Catalyst layers on either side of the membrane are required to enable the half-reactions due to the low operating temperature of PEM fuel cells. A single cell of a fuel cell stack is comprised of a porous anode, a proton-conducting membrane, and a porous cathode, the assembly of which is compressed between two plates (bipolar plates) that have embedded gas flow channels to allow for the transport of reactants and water.

A balance must be achieved between water production and removal such that the membrane is hydrated while the passage of gases and water is not obstructed. Water may accumulate in the porous cathode and block the transport of oxygen to the membrane, a condition known as flooding. At high current densities, the production

of liquid water may exceed the capacity of the gas streams to remove the water. The resulting decrease in electric potential is known as concentration polarization. Liquid holdup is a condition which occurs when the gas flow channels become completely blocked due to water accumulation and represents an acknowledged barrier to reliable PEM fuel cell development and is the primary motivation for this study. The reader is referred to Bazylak [16], Mukundan and Borup [17], and Trabold et al. [18] for reviews of water visualization and quantification methods, as well as Li et al. [19] in which the water management issues in PEM fuel cell are summarized.

Flooding of the flow fields occurs when liquid drops can no longer be evacuated and sufficient liquid volume accumulates to form water plugs. Flow field flooding occurs at relatively low air/H_2 stoichiometry, for which a plug/slug flow regime has been observed in operating fuel cells [33–36]. From microscale two-phase flow studies [1, 4] performed in semi-triangular and rectangular microchannels having a hydraulic diameter of 1 mm, it can also be concluded that a plug/slug flow regime is most likely to occur at low gas flow rates that correspond to low stoichiometry (≤ 2). Two-phase flow regimes in the gas channels and their relevance for the PEM fuel cell operation was reviewed by Anderson [37], who concluded that more optimization work is still needed.

Wetting properties have a significant effect on two-phase flow morphology in a microchannel where gravity is negligible and surface tension is important [3, 38]. Wettability is measured by the static contact angle with a 0° indicating a perfectly wetting fluid; that is the fluid spontaneously spreads over a solid surface. A contact angle of 90° is the transition between wetting and nonwetting fluids on a flat surface. The presence of a corner formed by two surfaces presents additional criteria for

11

defining wettability [39]. Liquid can spontaneously wick into or out of a corner due to capillary pressure gradients. The condition under which spontaneous wicking occurs is a combination of corner angle and static contact angle known as the Concus-Finn criteria, $\pi/2 > \alpha + \theta$, where α is the half-angle of the corner and θ is the static contact angle [40]. For the purposes of this discussion, when the channel contact angle for a square cross section is less than $90°$ but greater than $45°$ the configuration is considered partially wetting. When, for a square cross section, the contact angle is greater than $90°$ but less than $135°$ the configuration is considered partially nonwetting. This designation is based on whether there is an underpressure or overpressure in the water (relative to the gas phase) due to surface curvature. The wetting-nonwetting limits of the channel contact angle $(45°, 90°, 135°)$ will change if the corner angle changes as found in a triangular cross section.

Experiments conducted by Owejan et al. [20] concluded that the effect of flow field channel properties on water accumulation in operational fuel cells are important. They reported that a PTFE coated channel (contact angle $\theta_w = 95°$) demonstrated smaller, more uniformly distributed liquid plugs as compared to an 'uncoated' channel (contact angle $\theta_w = 40°$). Experiments performed by Bazylak et al. [41] reported that partially nonwetting gas channels may enhance drop formation and detachment, at the same time water was not collected under the channel lands. The better performance yielded by the partially nonwetting channels suggests the opportunity of further optimization through surface wettability and geometry. Numerical simulations performed by Ding et al. [42] showed that a less wetting GDL helps in expelling water from its surface while a partially wetting channel increases the GDL water coverage and the water residence time. On the other hand, simulations per-

12

formed by Cai et al. [43] concluded that partially wetting channels perform better for water discharge and gas diffusion. Quan and Lai [44] reported that for wetting surfaces and edges water transport is facilitated. The enhanced water transport results from corner flow. Ex-situ experiments by Lu et al. [45] reached the conclusion that wetting channels are advantageous over partially wetting or partially nonwetting channels, yielding less flow maldistribution and more stable operation due to a film flow regime. Wetting channels were observed to have draw-backs however, such as enhanced water retention. No general agreement exists for the use of wetting or nonwetting channels and it is clear that more research is necessary to be able to predict the behavior of liquid water in these types of microsystems.

Much of the research on liquid water in the reactant flow fields has been focused on water removal under operating conditions; either experimentally or using computational fluid dynamic (CFD) simulations. A complete review of these studies is beyond the scope of this paper. In general, it is difficult to compare experimental results from different researchers due to subtle differences in cell assembly, operating conditions, and material sets; all of which have a significant effect on water morphology in channels. CFD simulations have attempted to examine the dynamics of plug motion in channels, but have generally been limited to a single plug for which the volume is prescribed due to computational demands and the results remain qualitative [46]. CFD has not been able to predict the size of the plug formed.

Static configuration of liquid water in the flow field for a fuel cell that is not operating can provide useful information on water behavior under the action of capillary forces, at a very modest computational cost. A more thorough understanding of static configuration of water in the flow field will assist in development of material,

geometric, and operational strategies for improved water management. Colosqui et al. [47] proposed an analytical method to estimate liquid plug volumes formed under uniform wetting conditions in square acrylic channels. Their observations show that the size of the plug exhibits minimal dependence on the gas and liquid flow rates; indicating that a static calculation of plug volume is appropriate for some fuel cell operating conditions.

Previously, the volume and configuration of a static liquid plug in a fuel cell flow channel was shown to depend on wettability and geometry [48]. The motivation for the study presented herein is to assist the design of gas channels using information on static plug volumes and droplets formed under mixed wetting conditions. The minimum liquid volume required for a plug to exist is investigated. This is similar to recent studies on the stability of drops and plugs in tubes [49, 50] and the more general formulation for the existence (and nonexistence) of liquid occlusion in arbitrary tubes under transverse gravitational fields [51]. This study examines the minimum volume required for a plug to exist in channels with planar walls having different wettabilities.

For fuel cell flow fields, the wettability varies between the porous layer and the bipolar plate channel. This mixed wetting between surfaces results in a non-intuitive relationship between water drop location and flow field configuration. Similarly, the relationship between liquid plug formation and volume exhibits unusual behavior based on mixed wettability, channel geometry and channel bends.

14

(a) Initial Model　　　(b) $\theta_b = 150°$ and $\theta_w = 60°$　　(c) $\theta_b = 150°$ and $\theta_w = 110°$
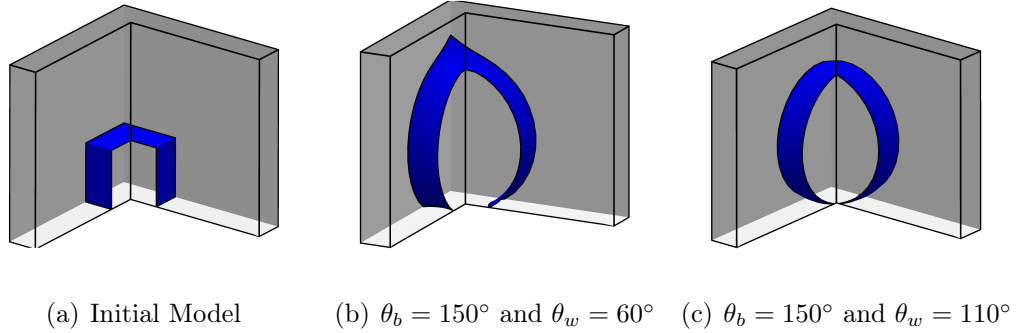
Figure 2.1. Initial and converged solutions for liquid that is in contact with the porous electrode (horizontal plane, contact angle θ_b) and two bipolar plate walls (contact angle θ_w) in a channel bend. The drops shown in 2.1(b) and 2.1(c) are the same volume.

2.2　Computational Model

Surface Evolver[21, 52] is an experimental mathematics program that can be used to study surfaces that are formed through the action of surface tension as well as other energies. It has been a valuable research tool for applications such as modeling the location of fuel in low gravity, computing capillary surfaces in exotic containers, simulating grain growth, calculating the rheology of foams, modeling the shape of molten solder on microcircuits, studying polymer chain packing, modeling cell membranes, knot energies and classifying minimal surface singularities. There have been limited studies on water morphology in fuel cells using Surface Evolver. The equilibrium morphology of isolated water drops in the porous transport layer with respect to fiber size and orientation has been studied by Roth [53]. Surface Evolver minimizes the total energy, which may have any number of components such as surface tension and gravitational potential. The minimization is performed

15

on an initially defined surface using a gradient descent method. The surface is comprised of triangular facets and the surface energy of a facet is its area multiplied by the surface tension. The contact angle may be set as a constraint after the appropriate edge integral is determined and included in the energy calculation. For a liquid drop sitting on a plane surface, the contact angle can be implemented by removing the wetted face and assigning to the drop boundary the same energy as that of the removed face. If the wetted face A has an interface energy density T, the energy of the removed plane surface can be ascribed to the contact angle through the corresponding line integral $\iint_A T\hat{k} \cdot d\mathbf{S} = \int_{\partial A} \mathbf{w} \cdot d\mathbf{l}$, where $\hat{j}$ and $\hat{k}$ are the y and z axes unit vectors. In this case, $\mathbf{w} = xT\hat{j}$ and the corresponding line integral can be included in the total energy as a constraint on the plane surface†.

To mimic an actual gas flow channel, the base corresponding to the porous transport layer (also known as the gas diffusion layer) has a contact angle θ_b different from the remaining three walls of the bipolar plate channel which have a contact angle θ_w. The effect of a change in channel wall wettability on drop morphology is shown in Figure 2.1 in which the water does not completely plug the channel. The water is in contact with both the vertical walls and the base, but not the channel wall opposite the gas diffusion layer (GDL). An initial configuration is shown in Figure 2.1(a) with the gas-liquid interface in shaded (blue) and the front walls removed for visualization. The contact angle on the horizontal plane (gas-diffusion layer) is the same for both cases with $\theta_b = 150°$. The converged solutions for channel wall contact angles of $\theta_w = 60°$ and $110°$ are shown in Figures 2.1(b) and 2.1(c), respectively. The water within a partially wetting channel bend will begin to wick up in the outer vertical corner due to a curvature gradient, while in the partially nonwetting channel bend

---

† Contact angle implementation in SE is described in more detail in Appendix A

the water tends to retract out of the corners. A growing drop of water would completely obstruct a partially wetting channel bend earlier than in a partially nonwetting channel bend.

2.3 Critical Plug Volume

The critical plug volume V_{CR} is defined as the minimum volume necessary for the water to completely obstruct a channel, that is, to form a plug. V_{CR} is a function of the contact angle, channel cross section and in-plane channel bends. The gravitational potential energy is neglected in the model and the gas-liquid interface shape is determined solely by surface forces. This assumption is justified based on the characteristic length scale of the channel and the resulting Bond number. The Bond number is a ratio of gravitational to capillary effects on the shape of a liquid surface and is defined as $Bo = \rho g L^2 / \sigma$, where ρ is the density of the liquid (neglecting the gas density), g is the gravitational acceleration, L is the characteristic length, and σ is surface tension. A water plug in a typical gas flow channel of 0.5 mm hydraulic diameter has Bo = 0.035 indicating the gravitational force has minimal effect on the liquid-gas interface shape.
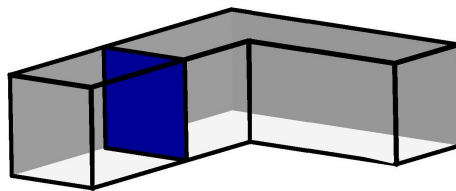
Figure 2.2. Initial model for determining the critical volume of a plug in a bend of a square channel using Surface Evolver. The left plug end consisting of a gas/water interface is shown, the right end (not visible) is symmetrically disposed.

17

Surface Evolver is only valid for static surfaces even though the surface shape changes with each computational iteration. A moving plug of water would be subject to contact angle hysteresis [54] and viscous stresses so that the interface shape becomes dependent on the flow conditions. Dissipation of energy is not captured in Surface Evolver so dynamic shape and plug volume cannot be studied is this manner. However, static plug interface shape and volume characterize intrinsic properties of mixed wettability channels and are a good indicator of the anticipated liquid water distribution in the reactant flow channels at low air/H_2 stoichiometry. In addition, the frequency of plug formation can be estimated for a given current density when the reactant flow is fully saturated.

The critical plug volume is determined by iteratively changing the volume of the initial model, shown in Figure 2.2. Each converged solution is computed by solving for a minimum energy interface with boundary conditions θ_b and θ_w in a channel with dihedral 2α, where $2\alpha = 180°$ is a straight channel. The surface defining the plug end translates during a Surface Evolver run and reaches a position according to the prescribed volume. The critical volume solution is determined when the ends of the liquid plug intersect resulting in a singularity. The critical volume calculated is the minimum volume for which a plug will exist. This volume is not the same as that determined using the stability limit of a growing drop that eventually forms a plug [49]. The critical volume is an intrinsic property of the mixed wettability channel whereas the plug volume determined by the stability of a growing drop will depend on the location of the drop; i.e. on the channel surface, on the GDL, or in a corner.

A Surface Evolver run requires modest computational time. Using an IBM T60

notebook with an Intel Centrino Duo T2500 CPU at 2 GHz and 512 MB of RAM, a minimum energy surface is obtained in 5 to 10 minutes. The geometric and surface energy constraints (facet energies) are checked for consistency by solving for a volume with 90° contact angles resulting in flat interfaces. This provides an easy visual validation of the input model as well as a check on volume calculation.

In Figure 2.2 the initial model is shown for a volume of water sufficient to plug the channel. Only half of a plug is shown, the other half being symmetric with respect to the bend dihedral bisector. The gas-liquid interface that forms the left plug side is shown shaded (blue). The value of surface tension is set to one, which is valid for a Bond number of zero. Changing the value of surface tension would subsequently change the line integral value corresponding to the contact angle. Therefore, changing the value of surface tension will have no effect on the converged interface shape nor the critical volume. Inclusion of gravitational potential would necessitate incorporation of scaled forces through the Bond number. The converged solutions for a GDL wettability of $\theta_b = 150°$ and two channel wettability conditions in a 1×1 cross section are shown in Figure 2.3. The critical plug volume for these runs are 2.16 and 3.52 for channel wall contact angles of $\theta_w = 50°$ and $\theta_w = 130°$, respectively. A plug of a lesser volume cannot exist in this configuration. The critical volume in a $d \times d$ square channel cross section can be obtained by multiplying $V_{\rm CR}$ by d^3.

The interface curvature and the critical plug volume change with surface wettability. The $\theta_w = 50°$ plug has a positive interface curvature with liquid pressure less than gas pressure, while the $\theta_w = 130°$ plug has negative curvature with liquid pressure higher than the gas. Values of θ_w below 45° cannot be simulated because a solution does not exist or is unbounded per the Concus-Finn criterion [40], which

19

(a) $\theta_w = 50°$ (b) $\theta_w = 130°$
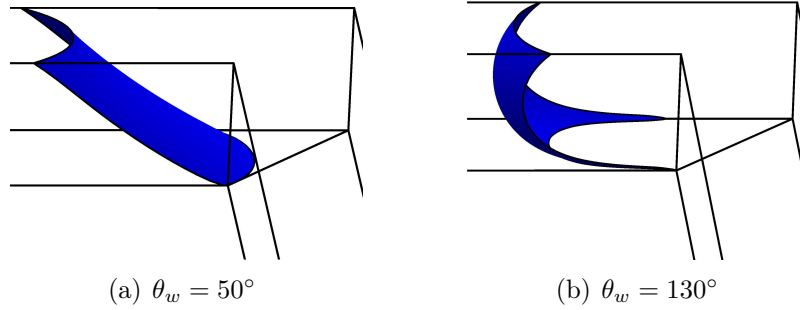
Figure 2.3. Critical volume plug in a 90° bend of a square channel for $\theta_b = 150°$ on the GDL surface(lower horizontal plane). The interface curvature is positive for $\theta_w = 50°$ on the bipolar plate (vertical planes and upper surface) and the water is in a state of under-pressure with respect to the gas. For the nonwetting cases the curvature is negative with the water in a state of over-pressure with respect to the gas.

is the criteria for capillary wicking in a corner. For $\theta_w = 50°$ the liquid plug is stretched along the upper corners as the Concus-Finn criteria of 45° is approached. If the contact angle on the channel surface is below 45°, the liquid could spread spontaneously along the corner thereby draining the plug [55, 56]. Thus, the lower limit for a converged solution is set by the Concus-Finn criterion, and the lowest wall contact angle used is 50° in order to attain convergence.

Contact angles below 45° would favor a relatively stable configuration corresponding to a liquid film attached to the more wetting surface as observed experimentally [45]. For partially nonwetting surfaces as shown in Figure 2.3(b) the liquid begins to de-wet the corners. This effect may occur when the contact angle is greater than 90° for perpendicular faces and will become more pronounced as the contact angle increases. A bounded solution does not exist for a channel with perpendicular walls when the contact angle approaches $\theta_w = 135°$. At 135°, the liquid will tend to spontaneously evacuate the corners in the absence of any other forces, but that does not preclude plug formation in fuel cell flowfields.

20

Figures 2.4 and 2.5 show the dependency of critical volume on contact angles and bend dihedrals. Critical volume solutions for a fixed GDL contact angle ($\theta_b = 110°$) and four bend dihedrals are shown for a range of bipolar plate wall contact angles (θ_w) in Figure 2.4. A similar data set for $\theta_b = 150°$ is shown in Figure 2.5. Each data point represents a fully converged solution. The critical volume solutions in a square cross section exhibit similar trends with respect to wall contact angle θ_w. The data set for each bend dihedral is offset from the straight channel by $1/\tan(\alpha)$, where α is the half-angle of the bend. Therefore, a correlation for V_{CR} as a function of θ_w can be generated for all bend dihedrals.

$$V_{CR} = a_0 + a_1 \left(\frac{\theta_w}{90}\right) + a_2 \left(\frac{\theta_w}{90}\right)^2 + a_3 \left(\frac{\theta_w}{90}\right)^3 + a_4 \left(\frac{\theta_w}{90}\right)^4 + \frac{1}{\tan(\alpha)} \tag{2.1}$$

where a_i are fitting coefficients and θ_w is in degrees. The coefficients a are given in Table 2.1 for base contact angles of $80°$, $110°$ and $150°$. The correlations are valid for wall contact angles of $50° \leq \theta_w \leq 130°$ and bend dihedrals from $90°$ to $180°$. For $2\alpha = 180°$ the channel is straight (without bend) and last term of the correlation is set to zero.

The dependence of these correlation on the GDL contact angle is not simple and a separate correlation for each θ_b appears to be necessary. Figure 2.6 shows the correlation for three different base contact angles ($80°$, $110°$, and $150°$) and a wall contact angle between $50° \leq \theta_w \leq 130°$ in a 1×1 channel. The dihedral angle factor of $1/\tan(\alpha)$ has been subtracted from each simulation so that the correlation is, in effect, for the straight channel. If the contact angle on the GDL surface decreases there is also a trend of decreased critical plug volumes, though not uniformly with channel contact angle. An example can be seen in the intersection of $80°$ and $110°$

21
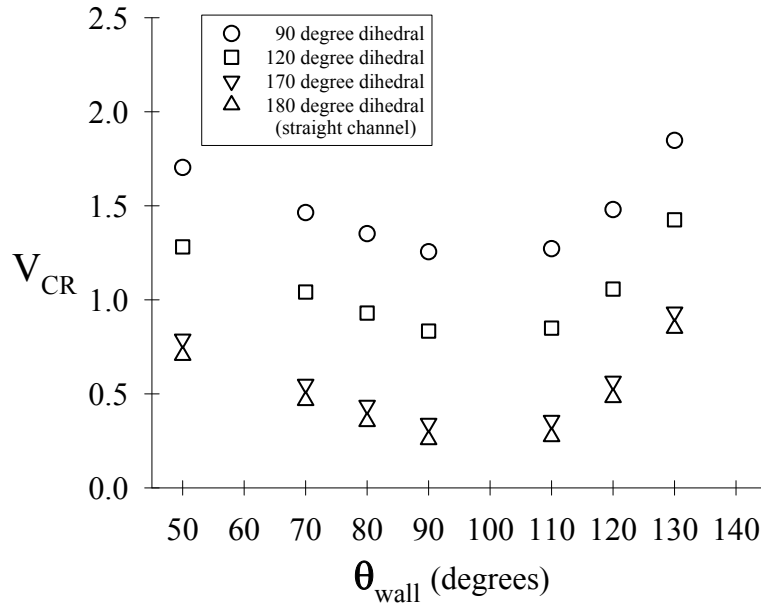
Figure 2.4. Critical plug volume in a 1×1 square channel for a range of bipolar plate contact angles θ_w for bend dihedral angles of 90°, 120°, 170°, and 180° (straight channel). The base, or GDL, contact angle is $\theta_b = 110°$.
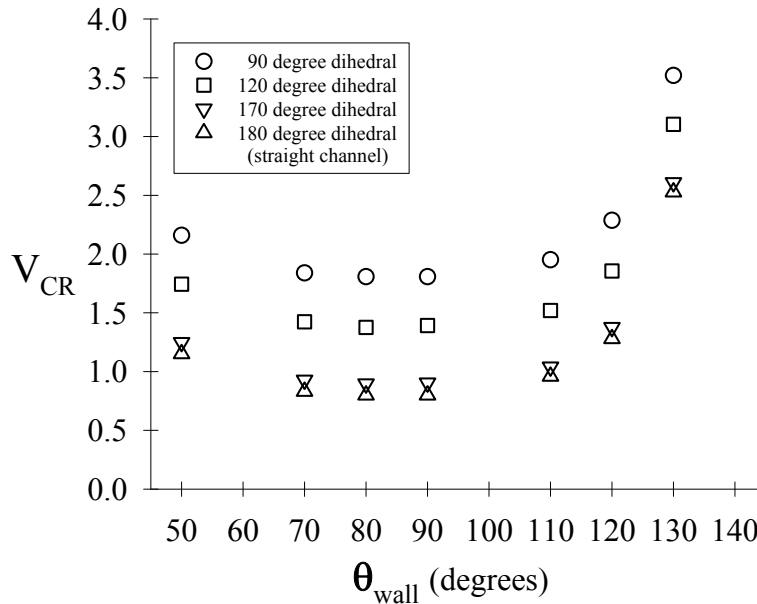
Figure 2.5. Critical plug volume in a 1×1 square channel for a range of bipolar plate contact angles θ_w for bend dihedral angles of 90°, 120°, 170°, and 180° (straight channel). The base, or GDL, contact angle is $\theta_b = 150°$.

22
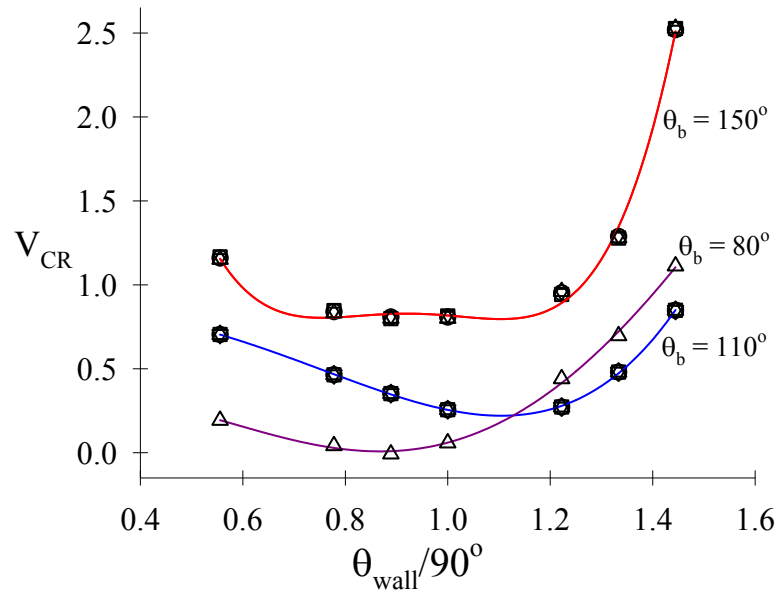
Figure 2.6. Critical plug volume in 1×1 square channels for a range of bipolar plate channel contact angles θ_w, three values of θ_b corresponding to three different GDLs. The correlations shown (solid lines) correspond to equation 2.1 and Table 2.1 for the straight $(2\alpha = 180°)$ channel. The family of curves shown in Figures 2.4 and 2.5 are obtained by adding $1/\tan(\alpha)$.

23

Table 2.1. V_{CR} correlation coefficients for a 1×1 square cross section channel with a contact angle θ_b on the GDL side. All angles are in degrees. The correlation for $\theta_b = 110°$ condenses all of the data shown in Figure 2.4 to a single curve. Similarly, the correlation for $\theta_b = 150°$ condenses all of the data shown in Figure 2.5. The correlation for the trapezoidal section is only valid for a straight channel, for which the last term of equation (2.1) is 0. The correlation coefficients are for θ_w in degrees and normalized by $90°$.

	θ_b	a_0	a_1	a_2	a_3	a_4	r^2
square	80	-0.3910	5.0443	-11.5088	8.8721	-1.9562	0.9983
square	110	0.8868	-0.0233	0.4513	-2.7382	1.6787	0.9995
square	150	21.6526	-93.2994	154.7584	-112.7123	30.4181	0.9952
trapezoidal	110	4.7701	-16.4804	28.052	-23.9858	7.9031	0.9988

correlations in Figure 2.6. The relative change in critical volume is not intuitive and indicates the need for specific simulations when wetting and nonwetting GDLs are used. For this particular case the critical volume is larger for the $80°$ GDL when the bipolar plate contact angle θ_w is greater than $102°$.

The general trend in critical volume correlations shown in Figure 2.6 can be separated into partially nonwetting ($1 < \theta_w/90° < 1.5$) and partially wetting ($0.5 < \theta_w/90° < 1$) interior corners. The critical volume increases as the wall contact angle approaches the convergence limits of $45°$ and $135°$ ($0.5 < \theta_w/90° < 1.5$), though the rate of increase in critical volume is much greater on the partially nonwetting side of the correlation. A gross estimate of plug length can be inferred from the value of the critical volume, $V_{\mathrm{CR}} \sim L/d$, where L is the plug length and d is the hydraulic diameter of the channel. The exact length will depend upon the meniscus curvature. Thus, per Figure 2.6, the plug length is approximately 2.5 times the channel dimension for $\theta_b = 150°, \theta_w/90° = 1.4$ and approximately 0.5 times the channel dimension for $\theta_b = 110°, \theta_w/90° = 1.4$. The plug length corresponding to

24

the critical volume is always less than three channel dimensions for the square cross section. Based on these correlations a channel-GDL configuration could be designed to deliver liquid plugs of a specific (critical) volume, which prompts the question of which critical volume (small or large) is most advantageous for fuel cell operation.

Experimental observations indicate that a single large plug is easier to move than multiple small plugs through a capillary-scale channel comparable to fuel cell flow fields [57]. This observation is generally true when the static contact angles range from 60° to 130° for which the energy dissipation resulting from moving contact lines is an important mechanism resisting plug motion [58]. Lee and Lee [59] note that pressure drop for plug flow in polyurethane and teflon tubes decreases with a reduction in the number of moving plugs. A follow on study concluded that the moving contact lines are a major factor in determining the pressure drop of plug flow [60]. Based on these experimental studies, for fuel cell operating conditions during which plug formation occurs, the flow field can more easily be cleared for lower frequency plug formation (longer average plug lengths). The channel-GDL surface energies that result in the longest plug length is for the partially nonwetting conditions as shown in Figures 2.4, 2.5, and 2.6.

The experimental study by Owejan et al. [20], which examined plug formation in an operating fuel cell under various channel wettabilities, would seem to contradict this conclusion. Their results show that the partially nonwetting channels ($\theta_w = 95°$) exhibited small, more uniformly distributed plugs than the wetting channels ($\theta_w = 40°$). Also, the partially nonwetting channels ($\theta_w = 95°$) demonstrated better performance in the mass transport limited region of the polarization curve as compared to the wetting channels; i.e., better performance with small plug lengths

25
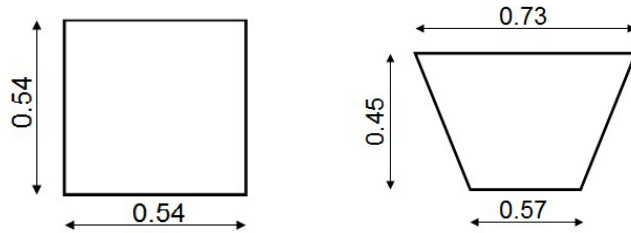
Figure 2.7. Square and trapezoidal cross sectional areas used for comparison of critical volumes. The area of the two sections are both 0.2925 mm².

rather than long plug lengths. However, a channel contact angle of 40° meets the Concus-Finn criteria in both the square and triangular cross sections tested. This results in liquid accumulation along the channel corners so that when a plug forms, the length can be on the order of a hundred hydraulic diameters as shown in neutron images. Under these conditions the inertial resistance impeding the motion of the plug becomes important in addition to the contact line energy dissipation. The wetting conditions ($\theta_w = 40°$) in the study by Owejan et al. [20] do not allow for a bounded solution using Surface Evolver because of corner wicking. For moderate length plugs that are less than three hydraulic diameters as predicted using Surface Evolver, contact line dissipation will be the dominant mechanism resisting plug motion. The fewer the contact lines, the easier the plugs can be removed from the flow field.

2.3.1   Comparison of Critical Volume for Square and Trapezoidal Cross Sections

The critical volume is compared for a square and a trapezoidal cross section with dimensions used in a typical PEM fuel cell flow field. The isosceles trapezoidal

26
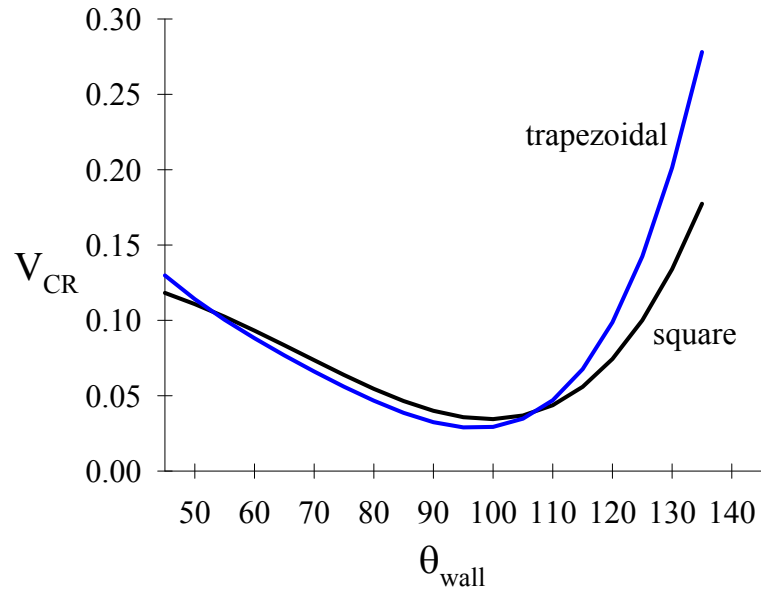
Figure 2.8. Liquid hold-up in a straight channel, square 0.54×0.54 and trapezoidal sections with parallel sides of 0.57 and 0.73 spaced by 0.45 as illustrated in Figure 2.7. The GDL contact angle is $\theta_b = 110°$ and the bipolar plate contact angle θ_w is varied. The curves shown are correlations per equation (2.1).

channel having the parallel sides of 0.57 and 0.73 distanced by 0.45 with a cross-sectional area of 0.2925 mm^2 has the same cross sectional area as a square channel of width 0.5408 mm. Figure 2.7 illustrates the respective geometries. The critical volume analysis enables a comparison between the square and trapezoidal geometries under varied wetting conditions.

Figure 2.8 is a comparison of critical volume for the square and trapezoidal cross sections for a $180°$ degree bend dihedral (straight channel) with a GDL contact angle of $\theta_b = 110°$. A simple relationship for the bend dihedral has not been found for the trapezoidal cross section. Thus, the trapezoidal correlation expressed in equation (2.1) with the coefficients listed in Table 2.1 are only for a straight channel. For a geometrically similar trapezoidal section with parallel sides spaced by a distance

27

ℓ, the critical volume can be obtained from multiplying equation (2.1) by $(\ell/0.45)^3$.

In a straight channel the critical volume V_{CR} is larger for the trapezoidal section than for the square section when $\theta_w \geq 110°$ even though the cross sectional areas are the same. At $\theta_w = 120°$, the trapezoidal critical volume is 20% greater and is 50% greater at $\theta_w = 130°$. The implication is that the larger the critical volume, the less frequently plug formation will occur under nominal fuel cell operating conditions and the less pressure drop required to keep the channels clear of water. Lu et al. [45] did not observe a significant difference in pressure drops for plug flow in square and trapezoidal cross sections with the same dimensions shown in Figure 2.7. However, the channel contact angle is reported as 85°, which per Figure 2.8 should result in nearly identical critical volumes and subsequently, similar plug lengths.

2.3.2   Plug Formation Frequency

The time required for a sufficient volume of water to accumulate for plug forma-tion can be approximated using the critical volume. The calculation assumes that water is collected over a channel length equal to three hydraulic diameters roughly approximating the Rayleigh instability wavelength, which has been shown as a valid pinch-off wavelength for capillary-scale two-phase flows [61–66]. For a liquid water flux into the cathode flow field at an equivalent current density of 0.4 cm^{-2} over an active area of 18.4 cm^2, similar to the ex-situ experiments performed by Lu et al. [34], the time necessary for critical volume accumulation may vary significantly be-tween the trapezoidal and square cross sections depending on the channel contact angle. When $\theta_b = 110°$ and $\theta_w = 130°$, the time to critical volume is 140 seconds in the square section, while in the trapezoidal section the time is 211 seconds.

28

2.4 Drop Location as a Result of Mixed Wettability

Even though water is uniformly distributed along the channels for high V_{CR} values, the cross-sectional water distribution may be predominantly towards the GDL. This implies that the gas transport across the GDL would be blocked resulting in flooding of the porous electrodes. Capillary forces naturally present in microchannels pose a challenge for water transport due to a large area-to-volume ratio. Surface Evolver simulations were performed for drops being in contact with two adjacent walls of a rectangular channel having different wettabilities simulating a water drop simultaneously contacting the bipolar plate and GDL.

The case of a drop which forms on the GDL side and makes contact with one of the bipolar plate walls is shown in Figure 2.9. The GDL has $\theta_b = 150°$ (horizontal plane) and the bipolar plate has $\theta_w = 100°$ (vertical plane). The drop shape and location is solely dictated by capillary forces that are initially unbalanced due to the difference in the surface energies of the two walls. The surface tension forces act on the drop surface as well as on the contact lines which are present at the gas/liquid/solid junction. The contact angle on the walls was prescribed and the drop evolution is shown at different iteration steps in Figure 2.9. The liquid volume migrates towards the lower contact angle surface, which is the vertical wall in order to minimize the surface area under given contact angles. This implies that water can be passively removed from the GDL surface to the bipolar plate walls by sole means of capillary forces, preventing thus the blockage of gas transport through the porous electrodes as well as flooding. Experimental observations of Bazylak et al. [41] corroborate this result.

29
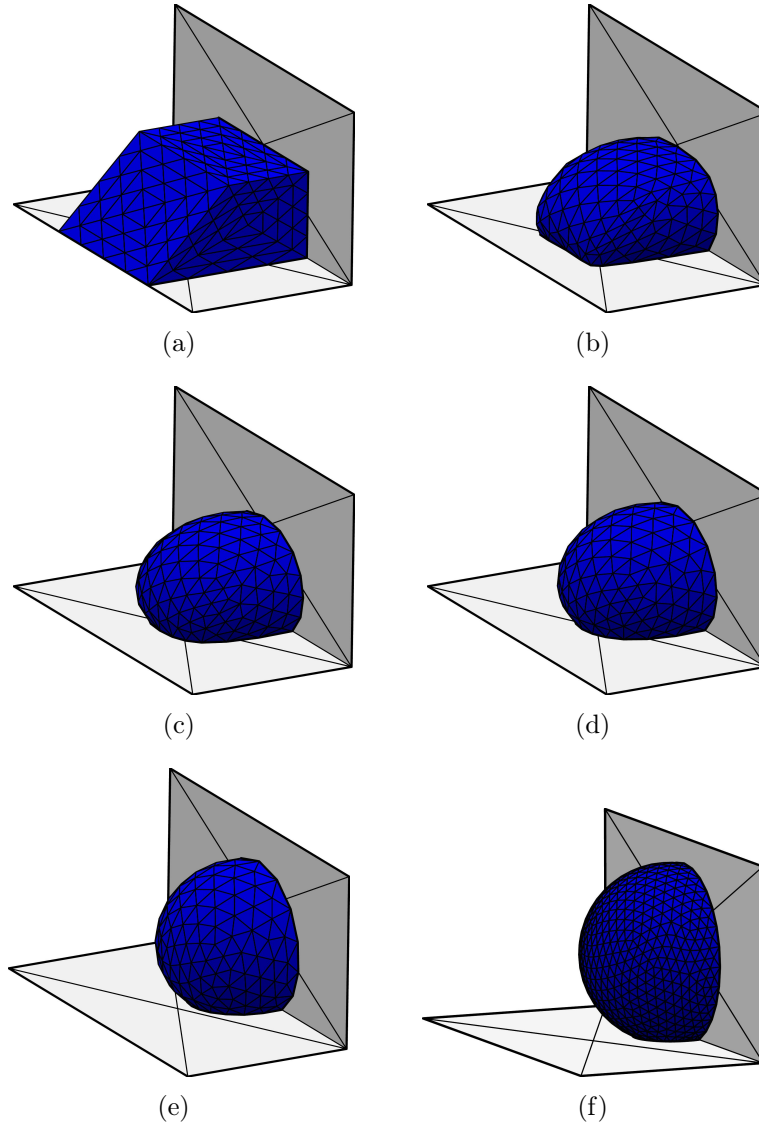
Figure 2.9. Energy minimization steps towards an equilibrium configuration (f). The base (GDL) contact angle is $\theta_b = 150°$ and the channel wall contact angle is $\theta_w = 100°$.

2.5 Wetting or Nonwetting Channels?

In order to better predict the flow morphology for preliminary design purposes, the critical volume data has to be corroborated with other information concerning either the particular geometry such as the presence of bends, the existence and stability of liquid films, and the presence of moving contact lines. For example, a GDL with $\theta_b = 150°$ can have the same critical volume with either a partially wetting channel ($\theta_w = 60°$) or a partially nonwetting wall ($\theta_w = 110°$) as shown in Figure 2.6. The choice of partially wetting or partially nonwetting channels is not immediately obvious. If other channel features such as bends are present, then additional simulations can be used to help determine the more optimal wetting condition. The channel bend simulations shown in Figure 2.1 indicate that the partially wetting channel ($\theta_w = 60°$) would tend to plug earlier than the partially nonwetting ($\theta_w = 110°$) channel for a drop growing in the bend. Therefore, the partially nonwetting channel would appear to be the more optimal configuration. Each combination of channel geometry, channel wettability, and GDL wettability presents a unique scenario.

Degradation of the GDL often results in a lower θ_b [67] and this may negatively impact fuel cell performance by decreasing V_{CR}, resulting in more numerous plugs. Using the correlations shown in equation 2.1 and Table 2.1, if a square channel with an initial GDL contact angle of 150° and channel contact angle of $\theta_w = 100°$ degrades to $\theta_b = 80°$ and $\theta_w = 80°$, then the critical plug volume will decrease by nearly a factor of ten. Ten times less water would be required to plug the degraded channel resulting in many more liquid plugs for a given current density. Consequently, there

will be many more moving contact lines within the same channel length and clearing the channel will be more difficult as compared to the initial wetting conditions.

2.6   Conclusion

The critical volume calculations via Surface Evolver enable estimation of the minimum volume of water required to plug the flow field channel of a PEM fuel cell with mixed wettability between the bipolar plate and the GDL. The correlations for critical volume are sensitive to the GDL and channel contact angles as well as channelcross-section and channel bends. For square cross section channels, the bend dihedral can be accounted for in the correlations of V_{CR} and θ_w through a single term, $1/\tan(\alpha)$. The utility of Surface Evolver has also been demonstrated with determining the equilibrium location of discrete drops within a fuel cell flow field. Notably, simulations show that water can be passively removed from the GDL surface to the bipolar plate if the latter has a lower contact angle, potentially avoiding flooding of the GDL.

The critical volume represents an intrinsic property of mixed wettability channels and V_{CR} is an implicit measure of static plug formation. As such, the magnitude of the critical volume can be used to estimate the frequency of plug formation during fuel cell operation at low reactant flow rates. Though the calculated critical volumes are for static morphologies, the effect of component degradation on water management can be inferred. The calculated critical volumes with corresponding correlations can be used to assess the effect of material degradation on water accumulation in flow field channels.

32

Partially nonwetting channels will tend to form relatively large plugs as compared to partially wetting channels, though the difference is only significant at the upper end of nonwetting. At $\theta_w > 120°$ the divergence in V_{CR} becomes apparent. This range of channel wettability would tend to produce the least number of liquid plugs, with the least number of moving contact lines. Experimental observations and energy dissipation arguments suggest that relatively large partially nonwetting plugs would be advantageous for fuel cell operation. Unfortunately, there appears to be no experimental data available for fuel cell operation with channel wettabilities greater than 120°. Contact angles on materials used for bipolar plates generally range from 80° to 120°, which exhibit small variations in critical volume as shown in Figures 2.4, 2.5, and 2.6. Fuel cell testing with $\theta_w > 120°$ would provide valuable results that could be used to assess the effectiveness of highly nonwetting GDL-channel combinations on water management in the flow field.

3. HIGH SPEED MICROSCOPY

Chapter comprising of two sections, reprinted by permission.

3.1 Periodic Interface Destabilization in High-Speed Gas-Liquid Flows at the Capillary Scale

[*] Recent research efforts have illustrated the importance of capillarity on the behavior of two-phase flow (gas-liquid) in low Bond number systems; that is, systems where capillary forces are important relative to gravitational forces. Such systems include capillary tubes and microchannels as well as the gas flow channels of a PEM fuel cell. High speed microscopy experiments visualizing air-water flow through a 500 micrometer square glass capillary, 10 cm long were conducted. The flow rates are significant with velocities of 6.2 m/s for the air and 0.2 m/s for the water. A unique annular flow with periodic destabilization of the gas-liquid interface has been observed. Standing waves develop on the liquid film and grow into annular lobes typical of that observed in low speed two-phase flow in capillary tubes. Atypical is

---

[*] Section reprinted by permission from ASME. The copyright agreement is attached in Appendix B. Herescu A, Allen JS (2006) Periodic interface destabilization in high-speed gas-liquid flows at the capillary scale. vol. 2006 B, pp 1157-1164 Limerick, Ireland: American Society of Mechanical Engineers.

the interface destabilization phenomena. The leading face of the lobe will decelerate and suddenly become normal to the wall of the square capillary while the trailing face of the lobe will remain gently sloped back into the annular liquid film. The transition between the leading and trailing faces acquires a sharp edge having a exceptionally large curvature. The entire structure then rapidly collapses and produces travelling waves which propagate upstream and downstream along the annular liquid film. The entire sequence of events takes approximately a half millisecond. This destabilization phenomenon is regular and periodic. Visualization of the destabilization from the high speed microscopy setup and preliminary analysis are presented.

3.1.1 Introduction

Two-phase flow plays a major role in a number of technologies critical to manned and unmanned space missions; including fuel cells, phase and particle separators, thermal management systems, and bioreactors. Many of these technologies exhibit a common morphology of complex flow paths, multiple channels, and manifolds. Terrestrial applications such as MEMS scale and lab-on-chip technologies also incorporate similar complex flow paths. Of particular interest in this study is the flow of gas and water vapor through microchannel gas flow passages of proton exchange membrane (PEM) fuel cells. [68]

A description of two-phase flow regimes in capillary tubes can be found in Barajas and Panton [3]. The effect of contact angle in delimitation and existence of different flow regimes was found to be important for tube diameters of 1.6 mm. For smaller diameters, as in the case presented herein (0.5 mm), capillarity becomes an even more important factor and some flow regimes (such as 'wavy', with gas flowing

36

above the liquid) no longer exist.

A discussion on the effect of a steady pressure disturbance moving at constant velocity along the interface of a thin viscous film was done in Kriegsmann, Miksis, and Vanden-Broeck [69]. However, the model employed neglects shear stress on the gas-liquid interface, which we believe should be included for proper description of interface destabilization studied herein. In Pols, Hibberd, and Azzopardi [70] there is a description of waves that occur in the case of simultaneous flow of a gas stream and a liquid film, denoted as 'roll waves' or 'disturbance waves'. It was observed that for smaller diameter tubes (<58 mm) the waves that appear in vertical annular flow are symmetrical around the circumference (ring shaped). The major differences from the present case is in that a turbulent velocity profile was considered while the flow in present system is most likely laminar, and also the gravity effect was included while we can confidently neglect it.

A PEM fuel cell relies on its flow field to transport water, hydrogen and air needed to sustain the chemical reactions that produce electricity. The flow field consists of a number of channels which are denoted as gas flow channels. Typically, the cross section of the gas flow channel is rectangular with a characteristic dimension on the order of one millimeter. As such, the gas and liquid flow in the gas flow channel is subject to capillary forces since the characteristic channel dimension is less than the Laplace constant, $L_c = \sqrt{\sigma/\rho g}$, where σ is surface tension, ρ is the liquid density, and g is gravitational acceleration. For water at 80 °C the capillary length is approximately 2.6 mm. Another means of assessing the importance of capillary forces on a two-phase system is with the Bond number. The Bond number is a ratio of gravitational effects to surface tension effects on a liquid surface and is defined

37

Figure 3.1. Schematic of high speed microscopy setup.

as Bo $= \rho g L^2/\sigma$, where L is the characteristic length scale. An alternative form of the Bond number is Bo $= (L/L_c)^2$. When the Bond number is small, surface tension effects dominate. A small Bo may be achieved by reducing the gravitational acceleration or by reducing the characteristic length scale as is found in capillary tubes. We define a microchannel as having a characteristic length scale such that the Bo < 1 in normal gravity.

The problem of liquid holdup is particularly acute in a low-Bond number environment where capillary effects can destabilize a liquid film which then may "pinch off" the flow passage with a liquid bolus.

3.1.2 Experiment Setup

The microchannel experiments investigate low-Bo number two-phase flow in a single microchannel. The system, illustrated in Fig. 3.1, consists of the visualization setup, and the water and air supplying lines. The two-phase flow test section consists of a 100 mm long, 500 μm wide square glass capillary tube. The two phases (water

38

and air) meet at the entrance region and naturally generate converging-nozzle-type entrance flow. The details of the capillary controlled mixing region can be found in [38, 68, 71, 72]. The uniquely designed and controlled entrance flow gives the several advantages in two-phase microchannel flow study. The two phase flow regimes including slug, slug-to-annular (transient), and annular flow can be synthetically generated by manipulating the single-phase supply pressure. Also, the naturally generated converging-nozzle-type flow also minimizes the entrance effect on the flow in the downstream of the microchannel. Water and air are supplied into the system from a 10 cc gas-tight syringe (water) and a 50 cc gas-tight syringe (air) both connected to the input tubes and controlled by two syringe-pumps with variable flow rate capability.

The visualization data was obtained via a high speed CMOS camera (Photron FASTCAM Ultima APX-RS) coupled to an inverted compound microscope (Nikon Eclipse TE-2000U) using a 4X objective and a 100 Watt halogen light source. The exposure time for all of the images presented herein is 9.8 μsec and the images were acquired at 10,000 frames per second.

3.1.3 Experimental Observations

Initially, the water flows in the corners of the capillary tube and also on the walls in the form of a thin film ($\sim 10\ \mu$m), while the air flows in the remaining volume (in the "center"). In the series of images presented, the region adjacent to the corners will appear as dark bands since the corner menisci reflect away the light, while the liquid lobes will appear bright as the light is transmitted directly into the microscope's objective lens. The "dark" or "bright" regions shouldn't be interpreted as "gas" or

39
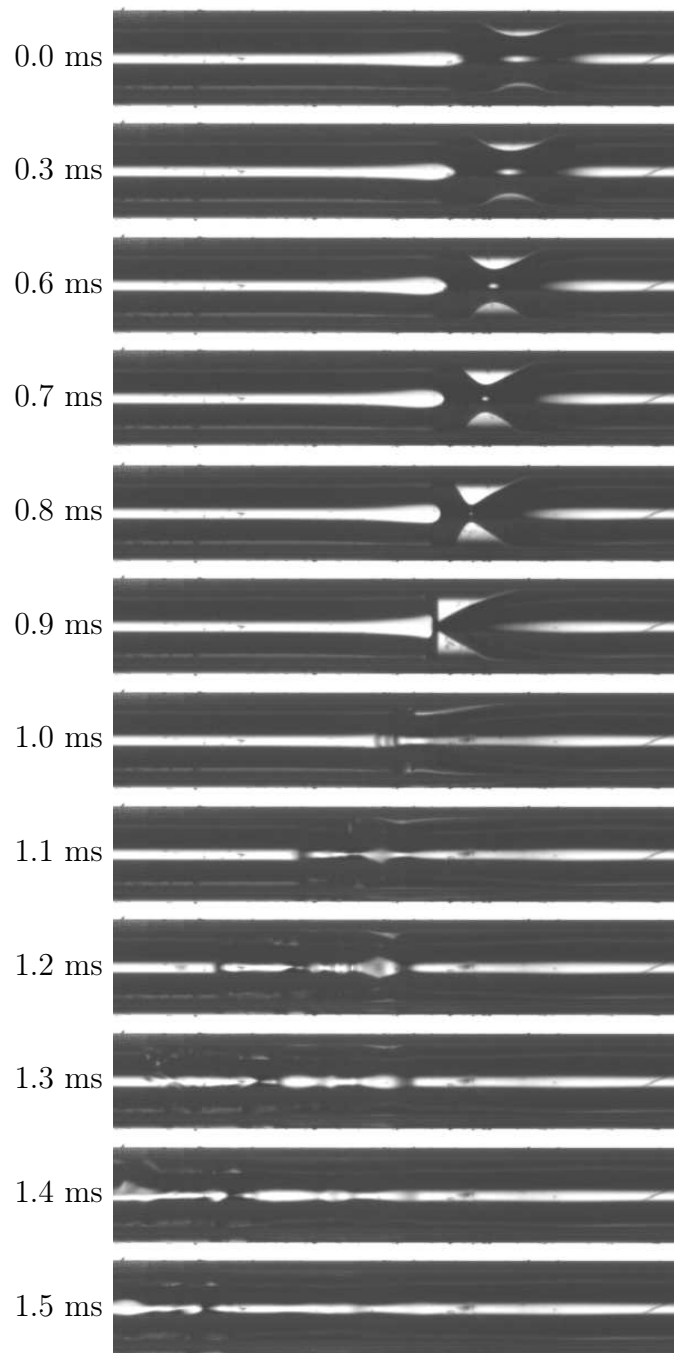
Figure 3.2. Sequence of lobe formation and collapse. The flow is from right-to-left and the width of the images is 3.931 mm.

40
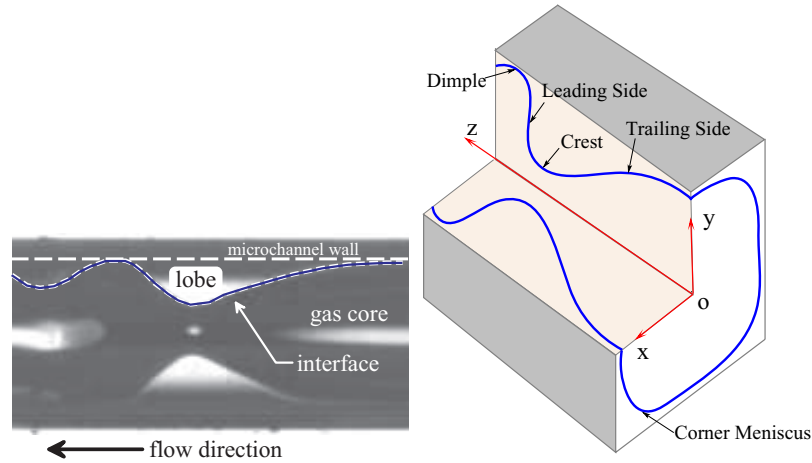
(a) Image of lobe formation detail- (b) Schematic of lobe formation in
ing the leading and trailing sides of the microchannel
the interface.

Figure 3.3. Lobe formation.The flow is from right-to-left with a high speed gas core.
The bright areas of the image result from the unimpeded path of the
backlight through the test section. The interface defines a gas core sur-
rounded by liquid adjacent to the microchannel walls.

"liquid", rather the liquid encompasses the gas phase and curved interfaces deflect the
transmitted light away from the objective lens. Bright areas represent the absence
of a curved gas-liquid interface in the ray path.

For flow rates of 10.07×10^{-6} kg/s (water) and 1.22×10^{-6} kg/s (air) an unsteady
annular flow regime is observed. The Bond number is Bo = 0.035 and $\text{Re}_l = 20$ for
water and $\text{Re}_g = 137$ for air based on the capillary width of 500 μm. The average gas
velocity is 6.2 m/s and average water velocity is 0.2 m/s. The superficial velocities
are 0.04 m/s for water and 4.1 m/s for air.

The gas-liquid interface that delimits the thin water film deposited on the in-
ner walls presents periodic capillary shear-driven instabilities as seen in the image
sequence shown in Fig. 3.2. These instabilities grow into liquid lobes that travel
in the direction of the flow (from right to left) at about 0.3 m/s which is close to

41

the estimated water velocity. Figure 3.3(a) is a magnified view of the liquid film instability highlighting the lobe formation. As the liquid lobes grow, they tend to coalesce at a critical volume forming a liquid plug characteristic for the plug flow regime. However, if the gas shear is high enough the coalescence of the liquid lobes may be prevented and the lobes will abruptly collapse back to the liquid film via capillary forces. This sudden collapse generates waves on the surface of the liquid film which propagate upstream and downstream.

A schematic of a lobe (unduloid) is shown in Figure 3.3(b). The flow is in the positive 'Z' direction (0-Z is the longitudinal axis) and the capillary tube is sectioned with three orthogonal planes (X-0-Y), (X-0-Z) and (Y-0-Z). In the (X-0-Y) plane, which is a cross-section upstream of the lobe, the geometry of the gas-liquid interface (the heavy line) consists of circular arcs (menisci) in the corners connected by thin layers (liquid films) along the walls. If we sliced the tube with a family of parallel planes perpendicular to the 0-Z axis the contour of the interface would evolve from that in the (X-0-Y) plane to quasi-circular and circular curves as we approach the crest (peak) of the lobe. The minimum diameter of the gas core corresponding to the lobe crest is estimated to be smaller than 50 μm in diameter for many of the non-coalescence lobe growth-collapse events. The (X-0-Z) and (Y-0-Z) are planes of symmetry for the lobes. The interface contour (heavy line) in the (X-0-Z) or (Y-0-Z) planes represents half of the lobe contour as seen in the images captured with the high speed camera and is characterized by the following elements: a 'dimple' preceding the leading side, a peak and a trailing side less steep than the leading one. The crest starts as a smooth, gently-sloped surface and gets narrow with a sharp peak as the wave approaches the collapse.

42
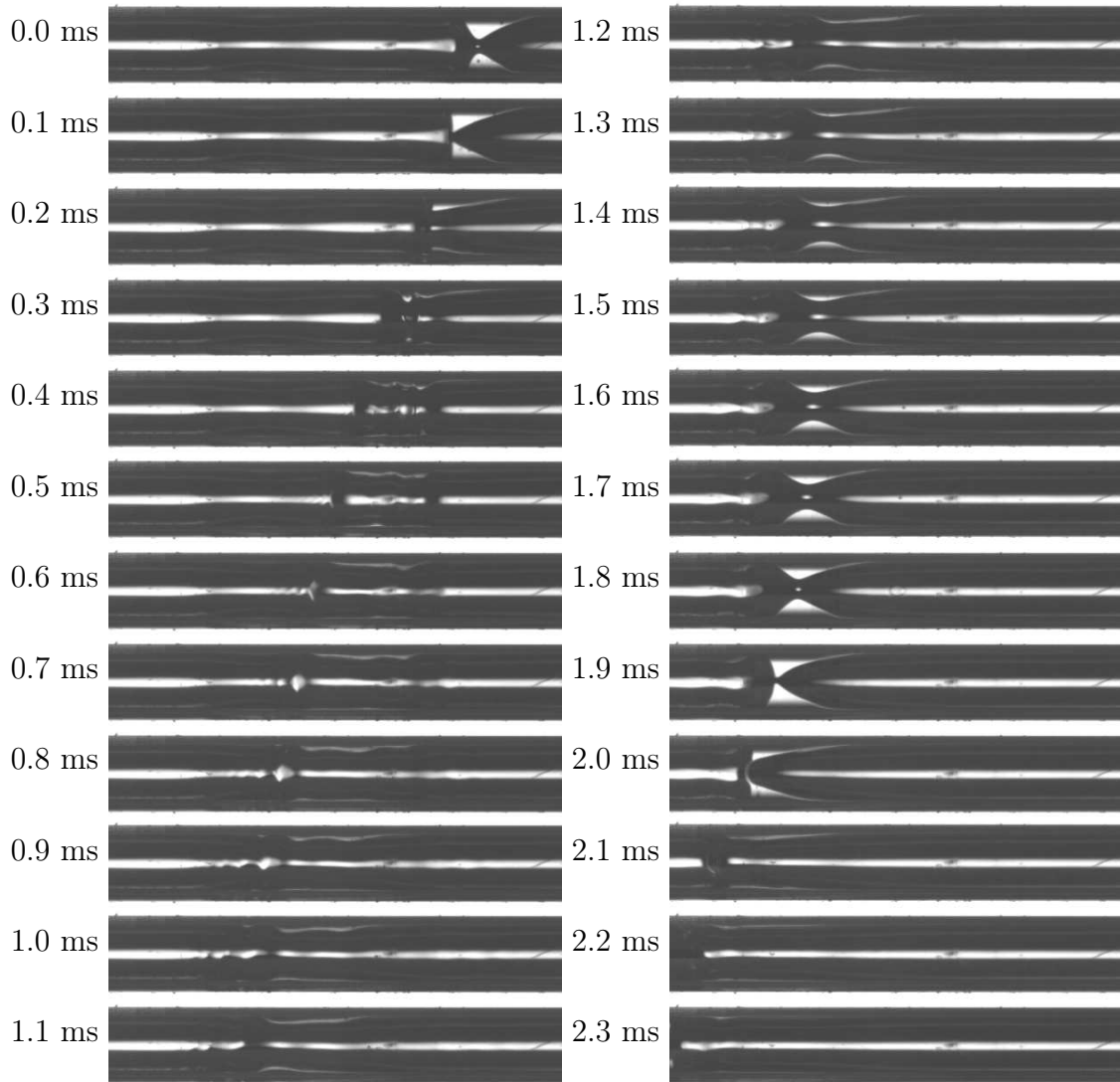
Figure 3.4. Sequence showing the repetitive liquid lobe formation and collapse. The formation and collapse occurs twice in a 2 ms period. The flow is from right-to-left and the width of the images is 3.931 mm.

43

The periodicity of lobe formation is shown in the sequence of images presented in Fig. 3.4, where we can see that the lobe formation and collapse occurs twice in a 2 millisecond time interval. The sudden collapse of the lobes may result from the capillary pressure imbalance caused by the sharp wave peak which occurs when the lobes are near coalescence.

An ejected droplet is captured in the image sequence shown in Fig. 3.7 traveling at about 6 m/s which is the same as the average gas flow rate. The series of images in Fig. 3.5 show the ejection of a droplet. After the coalescence of the lobes, the newly-formed liquid slug (0.1 ms) is accelerated from the liquid to near the gas velocity. When the accelerating liquid lobe reaches the downstream lobe traveling at a lower velocity coalescence and ejection of a liquid jet occurs (0.8 ms) which subsequently breaks into droplets due to a capillary instability. A magnified view of the droplet ejection is shown in Figure 3.6.

3.1.4   Discussion

The important physical mechanisms in the lobe formation, growth and destruction act upon the surface of the flowing liquid. These mechanisms include wall shear and shear on the gas-liquid interface, and surface tension. The velocity at which the lobes travel is about 50% higher than the estimated velocity of water (0.3 m/s vs 0.2 m/s), suggesting that shear on the gas-liquid interface might play a role in the wave dynamics (shear driven instability). In a capillary system (low Bo), body forces such as gravity may be neglected. Other forces that might be involved are caused by the distribution of pressure on the surface of the lobe due to the gas flow.

A perturbation deforms the gas-liquid interface causing the effective area through

44
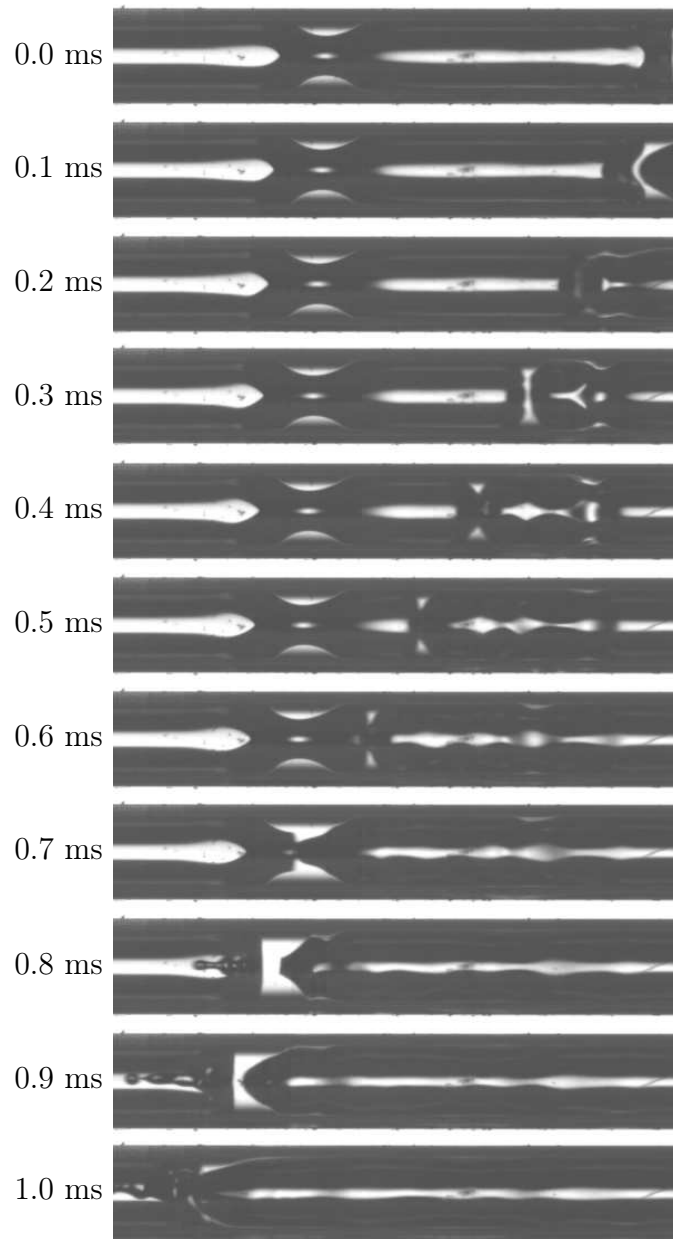
Figure 3.5. A 1-ms sequence of images showing lobe-lobe coalescence and subsequent droplet ejection. The faster liquid lobe (sometimes plug) on the right side of the image is moving approximately an order of magnitude faster than the slower moving lobe on the left. The coalescence of the two liquid masses results in an inertial ejection of a liquid jet shown at time 0.8 ms. The width of the images is 3.931 mm.

45
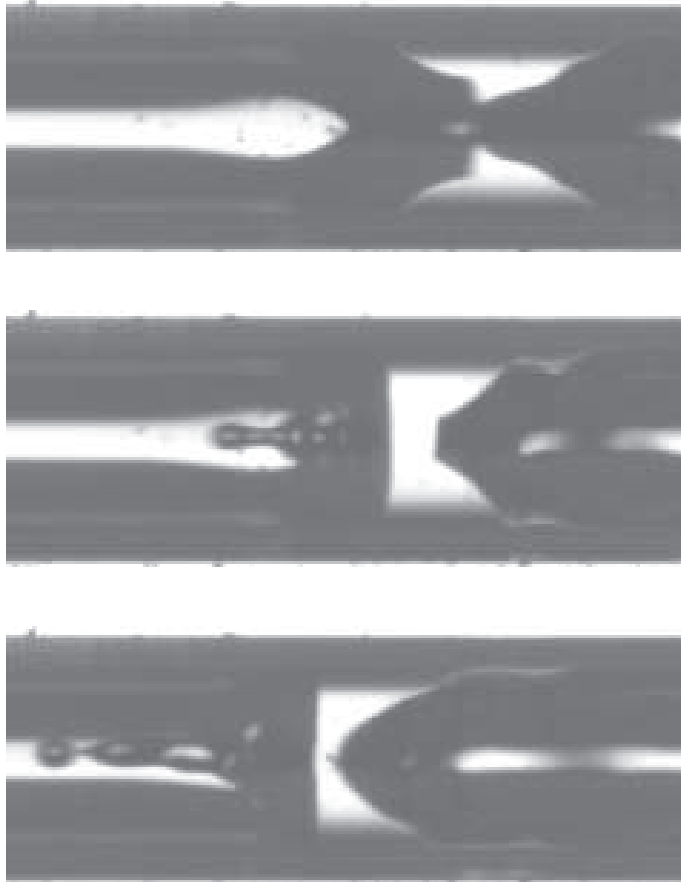
Figure 3.6. Magnified view of 2 ms droplet ejection sequence from Figure 3.5. In the top image (0.7 ms) coalescence is imminent. In the middle image (0.8 ms) coalescence has occurred and a liquid column is being ejected from the liquid plug. In the bottom image (0.9 ms) the liquid column is breaking up into drops which travel at very high velocities with the gas phase.

46
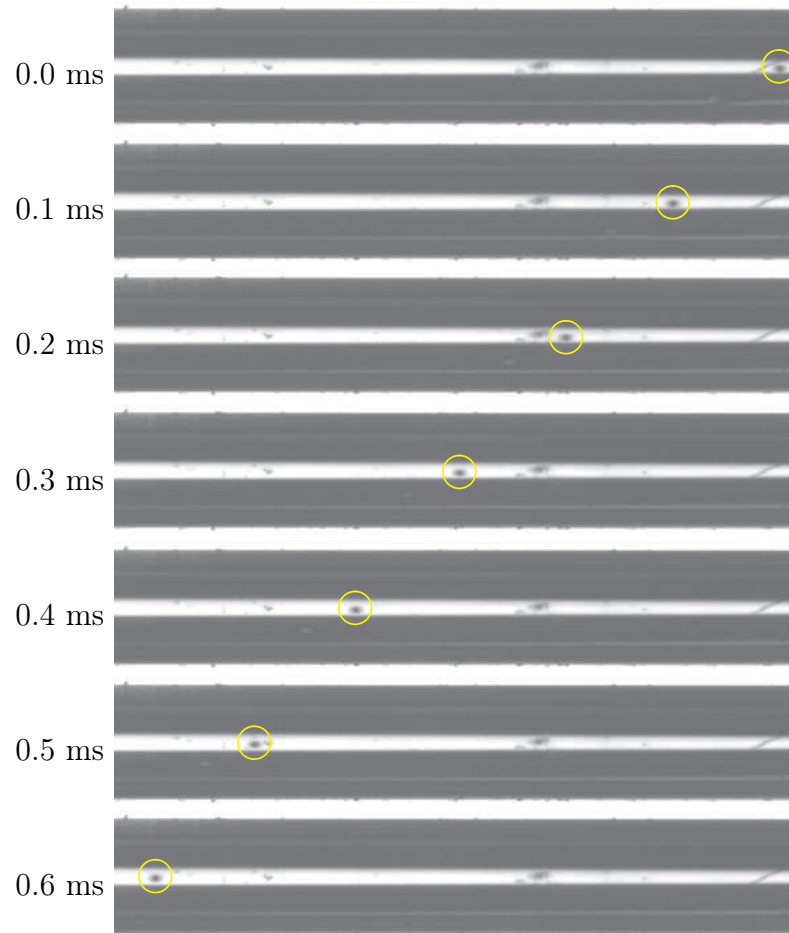
Figure 3.7. Sequence the motion of a liquid drop in the gas phase. The liquid drop is marked with a circle. The velocity of the drop is 6 m/s. The width of the images is 3.931 mm.

47

which water flows to shrink, the blockage thus formed forces the liquid to accumulate in lobes (capillary instability). It has been observed that, at the downstream edge of the moving lobe, the liquid film gets thinner which might lead to rupture. In the eventuality of film rupture we would have moving contact lines in the system that would dramatically increase the flow resistance and the pressure drop along the capillary tube.

When the lobes coalesce, the unduloid evolves into a liquid plug which is accelerated due to pressure build-up in the gas phase upstream of its location (inertial phenomenon). When the lobes don't coalesce, it was observed that the gas flow area is greatly reduced which might choke the air flow and cause a pressure build-up as in the previously mentioned case (the acceleration of the lobes is also apparent).

The rapid collapse of the lobes might be caused by an important pressure gradient due to surface tension forces at the 'peak' of the lobes which is visible at the time immediately preceding this event.

There were also observed waves that travel upstream and bounce against an existing liquid slug. An explanation of this phenomenon is that downstream of the observed location another lobe coalescence occurred and generated a pressure wave as the gas is compressed against the newly formed liquid plug. Depending on the magnitude of pressure build-up on the upstream side of a coalesced (or 'almost' coalesced) liquid plug and given the fact that this slug rapidly collapses, normal shock waves in the gas phase might exist.

The air velocity was estimated under the assumption of incompressible gas, which is reasonable considering that the Mach number is M=0.018. This hypothesis is also confirmed by the measured velocity of the water droplets traveling in the air stream,

48

which is 6 m/s and compares well with the estimated average air velocity of 6.2 m/s. However, if we look at the mass continuity (for air) between a section where the unduloids are not present and another section bounded by the wave peak observed at the time immediately preceding the lobe collapse, we obtain a velocity of 397 m/s which would exceed the speed of sound of 340 m/s for air as an ideal gas at the given temperature (15 °C). Even though for a global evaluation the gas could be taken as incompressible, locally it has to be considered compressible to account for phenomena such as pressure waves traveling at a finite velocity.

3.1.5   Conclusion

Periodic gas-liquid interface destabilization in a square 500 μm capillary tube was studied via high speed imaging technology. Wave formations that evolve from inception to collapse in less than one millisecond were identified on the interface. Possible physical mechanisms involved in the lobe formation and evolution were enumerated and discussed. It was stressed out that compressibility of the gas phase cannot be neglected since interaction between lobes and pressure waves (in gas) was noticed.

We believe this is the first presentation of this wave behavior in a capillary system. Further investigation and analysis is required in order to reveal the physics of interface destabilization and to delimit the corresponding transitional flow regime.

49

3.2 Compressibility Effects In The Gas Phase For Unsteady Annular Two-Phase Flow In A Microchannel

[†] High speed microscopy experiments investigating two-phase (gas-liquid) flow behavior in capillary-scale systems, that is, systems where capillary forces are important relative to gravitational forces, have revealed a unique unsteady annular flow with periodic destabilization of the gas-liquid interface. Standing waves develop on the liquid film and grow into annular lobes similar with those observed in low-speed two-phase flow. The leading face of the lobe will decelerate and suddenly become normal to the wall of the capillary, suggesting the possibility of a shock wave in the gas phase at a downstream location from the minimum gas flow section. Visualization of the naturally occurring convergent-divergent nozzle-like structures as well as a discussion on the possibility of shock wave formation are presented.

3.2.1 Introduction

Two-phase flow is important to a number of technologies at both the macro- and micro-scales. Many of these technologies, including fuel cells, heat exchangers, phase separators, and bioreators, exhibit a common morphology of complex flow paths, multiple channels, and manifolds. Microscale applications such as MEMS and lab-on-chip technologies incorporate similar flow complexity [73–77]. PEM fuel cells, while not microscale, are dependent upon microscale two-phase flow for effective

---

[†] Section reprinted by permission from ASME. The copyright agreement is attached in Appendix B. Herescu A, Allen JS (2006) Compressibility effects in the gas phase for unsteady annular two-phase flow in a microchannel. Chicago, IL, United states: American Society of Mechanical Engineers.

50

management of the product water [78].

A Polymer Electrolyte Membrane (PEM) fuel cell operates by catalytically stripping a hydrogen atom of its electrons and then passing the protons across a acid-based polymeric membrane. In order for the proton transport to occur, the membrane must be hydrated. The production of water at the cathode must be balanced by removal of water from the cell. As the oxygen gas stream becomes saturated, the removal of water from the gas diffusion layer via evaporation diminishes and water may accumulate. If the water accumulation becomes too great, then the gas flow channel may become completely blocked by water; a condition known as "liquid holdup". The problem of liquid holdup is particularly acute in a microchannel where capillary effects can destabilize a liquid film which then may "pinch off" the flow passage with a liquid bolus.

Reliable Polymer Electrolyte Membrane (PEM) fuel cell operation requires that the reactant flow be as uniform as possible over the entire MEA (membrane electrode assembly) surface. Uniform distribution can be difficult to achieve due to the number of parallel flow paths connected to the same inlet and exit. Liquid holdup in one or more locations along a channel or channels does not significantly affect the pressure drop and there is little driving force to move the liquid plug. This results in a mal-distribution of reactants which is detrimental to fuel cell operation and stability [6, 78].

Typically, the cross section of the gas flow channel is rectangular with a characteristic dimension on the order of one millimeter. As such, the gas and liquid flow in the gas flow channel is subject to capillary forces since the characteristic channel dimension is less than the Laplace constant, $L_c = \sqrt{\sigma/\rho g}$, where σ is surface tension,

51

ρ is the liquid density, and g is gravitational acceleration. At 80 °C, the operating temperature of a PEM fuel cell, the capillary length of water is approximately 2.6 mm which is greater than the characteristic length of the gas flow channels of a PEM fuel cell. Thus, the fuel cell flow field constitutes an array of microchannels.

Generally, microchannel two-phase flow has been investigated in much the same manner as macroscale two-phase flow. Flow regime maps are generated in order to predict flow regime transitions. [1, 6, 9, 13, 78–85]. Suo and Griffith [79],Biswas and Geenfield [80],Garimella and Coleman [81],Hassan et al. [9], Mishima and Hibiki [82],Tabatabai and Faghri [13],Triplett et al. [1],Wölk and Hans [83], Xu et al. [84],Zhao Zhao and Bi [85],Trabold [78],Owejan et al. [6] However, unlike macroscale two-phase flow, microscale two-phase flow can be significantly affected by local phenomena such as contact angle and cross-sectional geometry [3, 68, 86]. Contact angle and cross-sectional geometry define the curvature of a static liquid surface in a microchannel. The research results presented herein illustrate that local curvature is also extremely important to the behavior of a dynamic liquid surface in a microchannel.

3.2.2 Experiment Setup

The high speed microscopy setup, illustrated in Fig. 3.8, consists of a high speed camera coupled to an inverted microscope with controlled water and air feeds. The two-phase flow test section was a 100 mm long, 500 μm square glass capillary tube. The two phases (water and air) meet at the entrance region and naturally generate converging-nozzle-type entrance flow. The uniquely designed and controlled entrance flow gives the several advantages in two-phase microchannel flow study. The two
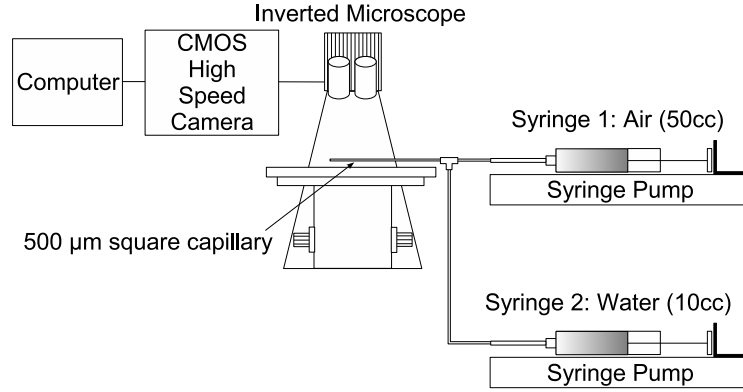
Figure 3.8. Schematic of high speed microscopy setup.

phase flow regimes including slug, slug-to-annular (transient), and annular flow can be synthetically generated by manipulating the single-phase supply pressure. Also, the naturally generated converging-nozzle-type flow also minimizes the entrance effect on the flow in the downstream of the microchannel. The details of the capillary controlled mixing region can be found in Allen et al. [68] and Son and Allen [38]. Water and air are supplied into the system from a 10 cc gas-tight syringe (water) and a 50 cc gas-tight syringe (air) both connected to the input tubes and controlled by two syringe-pumps with variable flow rate capability.

The visualization data was obtained via a high speed CMOS camera (Photron FASTCAM Ultima APX-RS) coupled to an inverted compound microscope (Nikon Eclipse TE-2000U) using a 4X objective. The exposure time for all of the images presented herein is 9.8 μsec and the images were acquired at 10,000 frames per second.
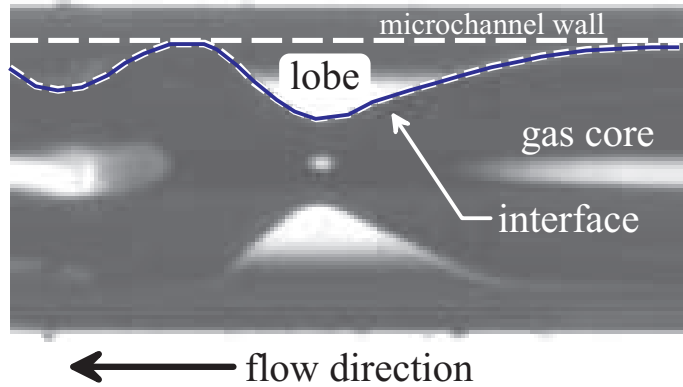
Figure 3.9. Image of lobe formation detailing the nozzle like liquid structure. The flow is from right-to-left with a high speed gas core. The bright areas of the image result from the unimpeded path of the backlight through the test section.

3.2.3 Experimental Observations

Within the 500 μm square microchannel, water wicks into the corners of the microchannel as well as spreads on the interior walls to form a thin liquid film (~ 10 μm), while the air flows in the core ("center"). The gas-liquid interface that delimits the thin water film deposited on the inner walls exhibits a periodic shear-driven instabilities. Figure 3.9 is a magnified view of the liquid film instability highlighting the lobe formation;the convergent-divergent nozzle is apparent. If Fig. 3.9, the regions adjacent to the corners appear as dark bands since the corner menisci reflect away the light, while the liquid lobe appears bright as the light is transmitted directly into the microscope objective. The "dark" or "bright" regions shouldn't be interpreted as "gas" or "liquid", rather the liquid encapsulates the gas phase and any curved interfaces deflect the transmitted light away from the objective lens. Bright areas represent the absence of a curved gas-liquid interface in the ray path. As the liquid lobes grow, they tend to coalesce at a critical volume forming a liquid plug.

54

However, at sufficiently high gas flows, coalescence of the liquid lobes is suppressed and the curvature of the liquid surface creates a converging-diverging nozzle. The physical mechanisms responsible for the growth and sudden collapse of this nozzle-like structure on the liquid surface are as yet unknown.

The minimum diameter of the gas core corresponding to the lobe crest (the nozzle throat) is estimated in the range of 50 μm in diameter for many of the non-coalescence lobe growth-collapse events. The interface contour is characterized by the following elements: a 'dimple' preceding the leading side, a peak and a trailing side less steep than the leading one. The crest starts as a smooth, gently-sloped surface and gets narrow with a sharp peak as the wave approaches the collapse.

The image sequence shown in Fig. 3.10 illustrates the growth and abrupt collapse of a liquid lobe. Instabilities on the liquid surface grow into lobes which travel in the direction of the flow (from right to left). For this sequence of images, the flow rates are 10.07×10^{-6} kg/s for the water and 1.22×10^{-6} kg/s for the air. The Bond number is Bo = 0.035 and $\text{Re}_l = 20$ for water and $\text{Re}_g = 137$ for air based on the capillary width of 500 μm. The average gas velocity is 6.2 m/s and average water velocity is 0.2 m/s while the superficial velocities (flow rate divided by channel cross sectional area) are 0.04 m/s for water and 4.1 m/s for air. The liquid lobes move at approximately 0.3 m/s.

The lobe formation and growth occurred in approximately 1 ms at which point the leading edge of the lobe becomes perpendicular to the channel wall with extremely large curvature at the core. Then, in less than 1/10 ms, the lobe collapses and generates surface waves which travel downstream (and possibly upstream) on the annular liquid film (1.1 to 1.6 ms images). It is hypothesized that the leading

55

0.0 ms

0.3 ms

0.6 ms

0.7 ms

0.8 ms

0.9 ms

1.0 ms

1.1 ms

1.2 ms

1.3 ms
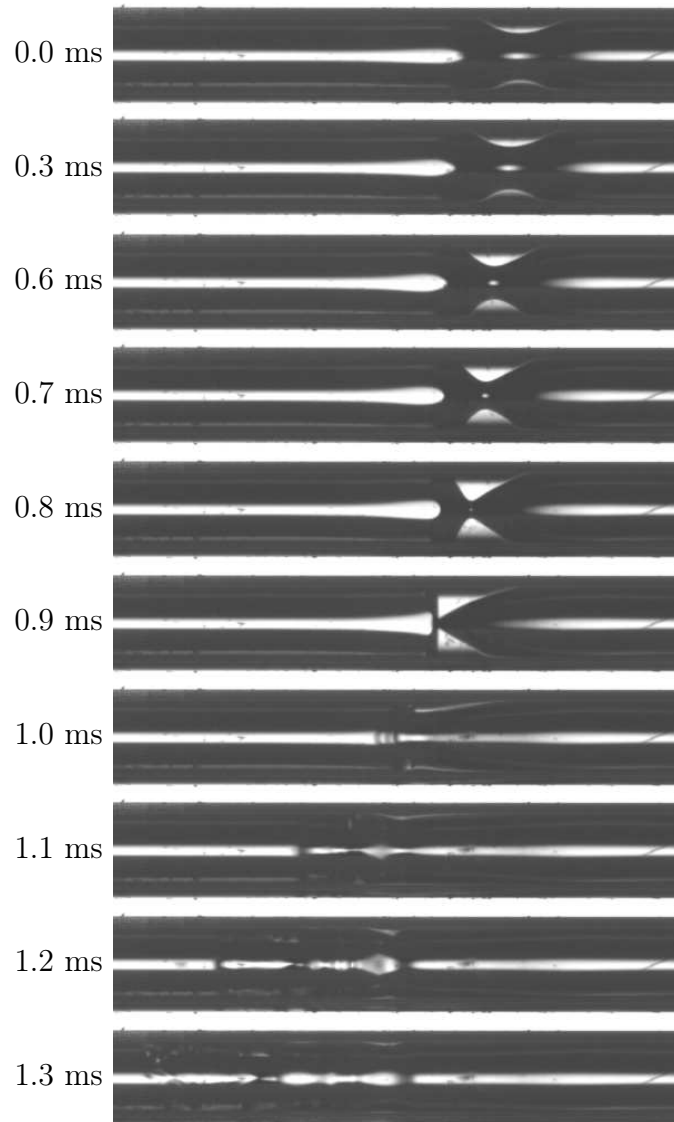
Figure 3.10. Sequence of lobe formation and collapse. The flow is from right-to-left and the width of the images is 3.931 mm.

56

edge of the lobe flattens as a result of a density wave in the gas reflecting off of the lobe. The density wave reflection results in a curvature with an estimated pressure difference of 12,800 Pa over 225 μm between the lobe apex and the channel wall. The large pressure drop drives the liquid lobe back towards channel wall. The periodicity of lobe formation is shown in the sequence of images presented in Fig. 3.4, where the lobe formation and collapse occurs twice during a 2 ms time interval.

3.2.4 Discussion

The physical mechanisms associated with the lobe formation, growth and collapse include wall shear, shear on the gas-liquid interface, and surface tension. The velocity at which the lobes travel is about 50% higher than the estimated velocity of water (0.3 m/s vs 0.2 m/s), suggesting that shear on the gas-liquid interface is driving the lobe motion and growth. Recent numerical results of Zhang and Bankoff [87] suggest that interfacial shear may also contribute to the flattening of the lobe's leading edge. The local pressure in the lobe and the rapid collapse also suggest that another mechanism is at work.

When the lobes coalesce, the unduloid evolves into a liquid plug which is accelerated due to pressure build-up in the gas phase upstream of its location (inertial phenomenon). When the lobes don't coalesce, it was observed that the gas flow area is greatly reduced which may choke the air flow and cause normal shock waves downstream of the nozzle throat. Rapid acceleration of the lobes is also apparent. The air velocity is estimated assuming incompressible gas, which is reasonable (globally) considering that the Mach number is M = 0.018. The gas velocity is also confirmed by the measured velocity of the small water droplets traveling in the air stream.

57

Even though for a global evaluation the gas could be taken as incompressible, locally it has to be considered compressible to account for phenomena such as pressure waves traveling at a finite velocity.

Assuming stagnation conditions for the gas flow upstream of the throat of a nozzle-like structure of $T_0 = 298$ K and $P_0 = 1$ atm, the critical mass flow rate necessary to attain Mach number of one at the minimum section (taken 54 μm in diameter) results as 5.4×10^{-7} m^3/s while the estimated air mass flow rate was 1.2156×10^{-6} m^3/s which is comparable to the gas flow rate for these experiments. This suggests a strong possibility for the occurrence of normal shock waves provided that the back pressure in a section downstream of the throat drops below a critical value. The pressure gradient in the flow direction is negative, therefore the back pressure can attain values between those at the entrance and at the exit of the microchannel. A shock wave would then form downstream of the minimum gas flow section (nozzle throat). Upstream of the shock there is an expansion of the gas, which may cause the flattening of the downstream lobe surface just prior to lobe collapse. The normal shock wave travels towards the throat (upstream) while the lobes move downstream such that some interaction between the wave and the lobes is expected.

3.2.5   Conclusion

An unsteady annular two-phase flow regime in a square 500 μm capillary tube was studied via high speed imaging technology. Wave formations that evolve from inception to collapse in less than one millisecond were identified on the interface. Compressibility effects in the gas phase, and potentially shock waves, are thought to be

the mechanism for generation of the extremely large capillary pressures which drive the liquid back into the thin film region of the microchannel. Further investigation is required and new visualization techniques need to be developed in order to confirm this hypothesis. The existence of shock waves would have serious implications for the operation of a PEM fuel cell, since the occurrence of this phenomenon could increase the pressure drop across the system and, more significantly, the localized pressure could result in premature degradation of structural elements within the gas flow channels.

4. Two-Phase Flow in Microchannels

4.1 Foreword

Two-phase morphology is described in a variety of terminologies, which could be summarized as intermittent (plug/slug) flow, annular, bubbly, churn/dispersed rivulet/wavy and separated/stratified [3]. The existence of different morphologies is typically presented as two-phase flow maps having the gas and liquid superficial velocities ($U_{G,S}$, $U_{L,S}$) as abscissa and ordinate, respectively. The superficial velocity is defined as the volumetric flow rate divided by the cross-sectional area. There are numerous microchannel flow regime maps (Hassan, Damianides, Triplett, Coleman, Kawaji, Kawahara [1, 2, 9–12], etc.) which attempt to give universal transition criteria using the classical macroscale parameters, the superficial velocities. These studies were not successful due to the fundamental differences between macroscale and interface dominated microscale flows. Other authors took a different approach using dimensional analysis to devise transition criteria (Waelchli, Tabatabai, Akbar [7, 13, 14]). Although these studies bring us closer to a physical understanding of capillary scale two-phase flow they cannot be extended to other cases. There is a need of fundamental knowledge of the interface behavior.

Barajas and Panton[3]were the first to note a shift in the flow regime transition

61
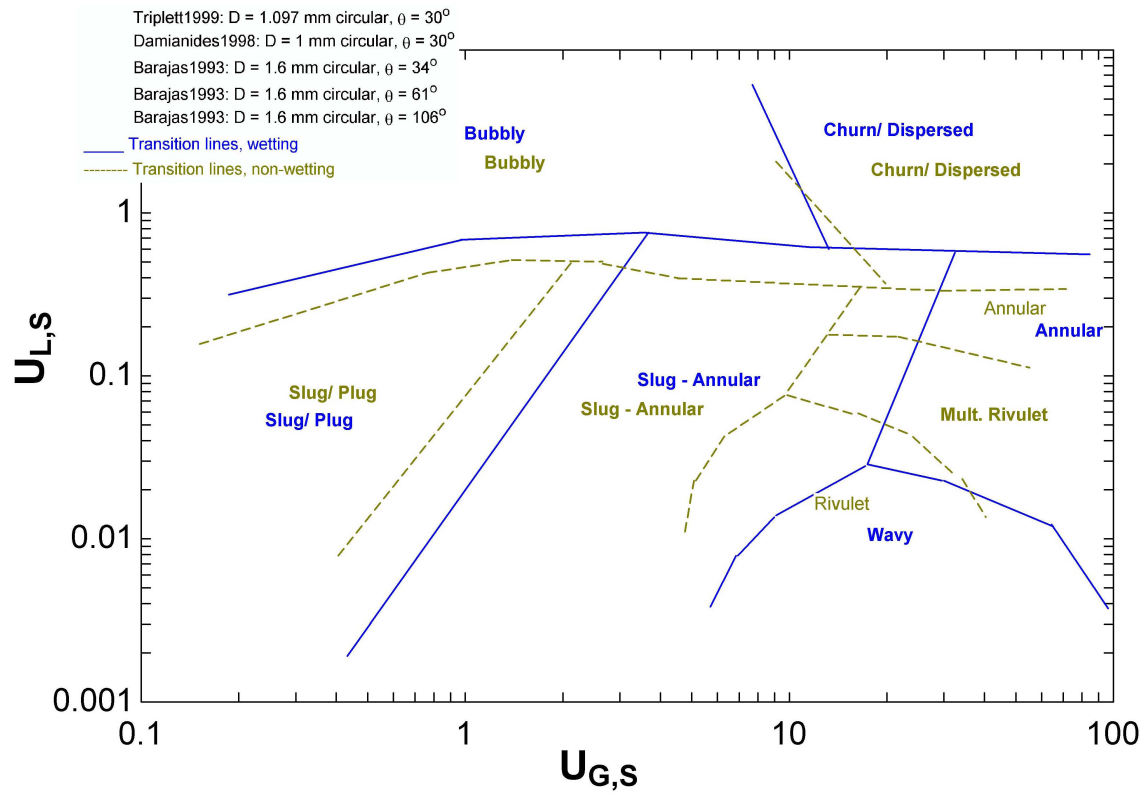
Figure 4.1. Two-Phase Transitions in Round Microchannels [1–3]
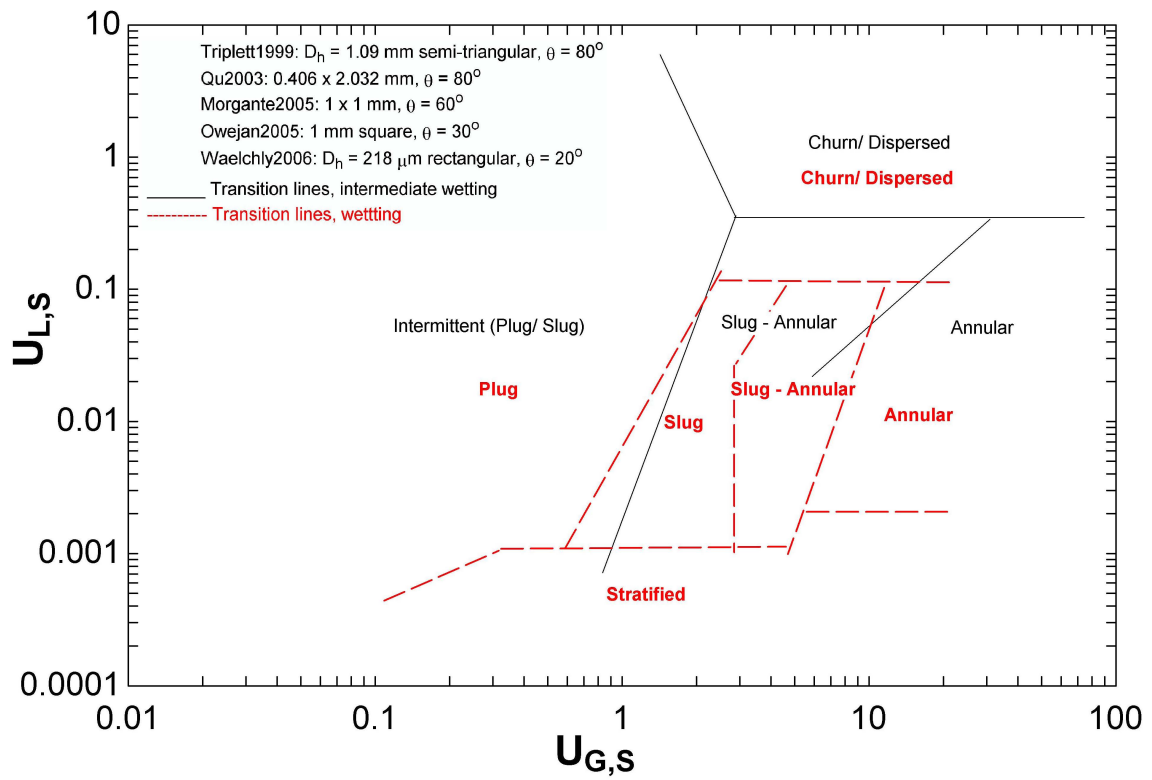
Figure 4.2. Two-Phase Transitions in Square Microchannels [1, 4–7]

lines of round 1.6 mm diameter tubes as the contact angle is changed. Herescu and Allen[15] showed that the flow regime in square and round 0.5 mm tubes changes with the contact angle (θ), four morphologies were observed for θ=20°, 60° and 105° at the same flow rates. These findings suggest that both cross-sectional geometry and contact angle change the flow morphology. To better show this, experimental results from literature were grouped by geometry (round and square) and the transition lines were shown for different wettabilities (wetting $\theta < 45°$, intermediate wetting $45° < \theta < 90°$ and nonwetting $\theta > 90°$) in Figures 4.1 and 4.2.

*The following section is reprinted by permission.**

4.2   Wetting Effects on Two-Phase Flow In A Microchannel

In the recent years there has been an increasing interest in the study of two-phase flows in low Bond number systems (where capillary forces are important relative to gravitational forces). Such systems include capillary tubes and microchannels as well as the gas flow channels of a PEM fuel cell. At the capillary scale, surface tension forces play an important role in two-phase flow regime transitions, pointing out the need to take into account the geometry of the cross section and the surface properties (wettability). Surface tension is generally considered in flow transitions, but the wetting properties of the fluid-surface material pairs (contact angle) are rarely given any importance. The researchers investigating two-phase flows should take extreme care when choosing the material of the test sections, as the flow morphology and the the pressure drop accordingly can vary widely with contact angle. In order to show these morphological changes high speed visualization experiments of air-water flow through 500 μm square and round microchannels were conducted. For the round channels, contact angles of less than 20° (wetting) and 105° (non-wetting) were investigated. For the square section, things are complicated by the presence of the corners. According to the Concus-Finn criterion, the liquid will wick into (wet) the corner if the contact angle is less then 45°, or will de-wet the corner if the contact angle is above 45°. A new case not previously mentioned in the literature

---

arises for a contact angle of $45° \leq \theta \leq 90°$, for which the liquid is wetting the walls but de-wetting the corners. Three contact angles of less than $20°$, $80°$ and $105°$ are considered to investigate the possible morphologies in the square geometry. Images aquired with a high speed camera depicting the different flow morphologies that exist at the same air-water flow rates for each of the considered contact angle and geometry are presented.

4.2.1 Introduction

Two-phase flow plays a major role in a number of technologies critical to manned and unmanned space missions; including fuel cells, phase and particle separators, thermal management systems, and bioreactors. Many of these technologies exhibit a common morphology of complex flow paths, multiple channels, and manifolds. Terrestrial applications such as MEMS scale and lab-on-chip technologies also incorporate similar complex flow paths. Of particular interest in this study is the flow of gas and water vapor through microchannel gas flow passages of proton exchange membrane (PEM) fuel cells. [68]

A description of two-phase flow regimes in capillary tubes can be found in Barajas and Panton [3]. The effect of contact angle in delimitation and existence of different flow regimes was found to be important for tube diameters of 1.6 mm. For smaller diameters, as in the case presented herein (0.5 mm), capillarity becomes an even more important factor and some flow regimes (such as 'wavy', with gas flowing above the liquid) no longer exist.

PEMfuel cells incorporate gas flow channels used for the gas and water transport necessary to sustain the electrochemical reactions. Typically, the cross section of the

66

gas flow channel is rectangular with a characteristic dimension on the order of one millimeter. The gas and liquid flow in the gas flow channel is subject to capillary forces since the characteristic channel dimension is less than the Laplace constant, $L_c = \sqrt{\sigma/\rho g}$, where σ is surface tension, ρ is the liquid density, and g is gravitational acceleration. For water at 80 °C the capillary length is approximately 2.6 mm. Another means of assessing the importance of capillary forces on a two-phase system is with the Bond number. The Bond number is a ratio of gravitational effects to surface tension effects on a liquid surface and is defined as Bo $= \rho g L^2 / \sigma$, where L is the characteristic length scale. An alternative form of the Bond number is Bo $= (L/L_c)^2$. When the Bond number is small, surface tension effects dominate. A small Bo may be achieved by reducing the gravitational acceleration or by reducing the characteristic length scale as is found in capillary tubes. We define a microchannel as having a characteristic length scale such that the Bo < 1 in normal gravity.

The problem of liquid holdup is particularly acute in a low-Bond number environment where capillary effects can destabilize a liquid film which then may "pinch off" the flow passage with a liquid plug.

4.2.2   Experiment Setup

Present experiments investigate low-Bo number two-phase flow in a single microchannel. The system, illustrated in Figure 4.3, consists of the visualization setup, and the water and air supplying lines. The two-phase flow test sections consist of a 100 mm long 500 μm wide square glass capillary tube, a 120 mm long 500 μm diameter round glass tube and a 500 μm wide 100 mm long acrylic coated square channel.For the uncoated square and round channels the contact angle is less than 20°. To obtain

67
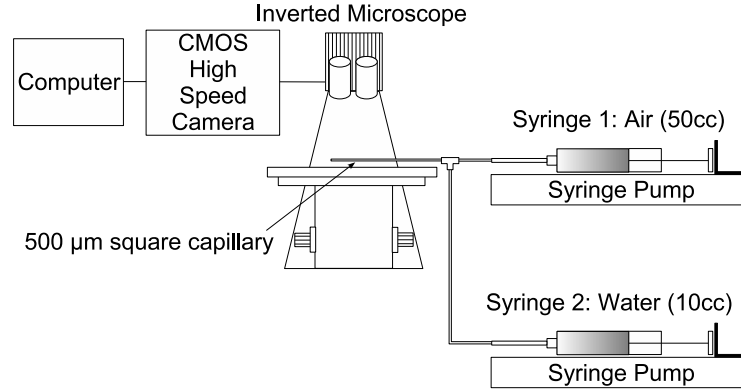
Figure 4.3. Schematic of high speed microscopy setup.

a contact angle of 105° the glass channels are coated with a comercially available glass treatment. The two phases (water and air) meet at the entrance region and naturally generate converging-nozzle-type entrance flow. The details of the capillary controlled mixing region can be found in [38, 68, 71, 72]. The uniquely designed and controlled entrance flow gives the several advantages in two-phase microchannel flow study. The two phase flow regimes including slug, slug-to-annular (transient), and annular flow can be synthetically generated by manipulating the single-phase supply pressure. Also, the naturally generated converging-nozzle-type flow also minimizes the entrance effect on the flow in the downstream of the microchannel. Water and air are supplied into the system from a 10 cc gas-tight syringe (water) and a 50 cc gas-tight syringe (air) both connected to the input tubes and controlled by two syringe-pumps with variable flow rate capability.

The visualization data was obtained via a high speed CMOS camera (Photron FASTCAM Ultima APX-RS) coupled to an inverted compound microscope (Nikon Eclipse TE-2000U) using a 4X objective and a 100 Watt halogen light source. The images were acquired at 10,000 and 15,000 frames per second.

The flow rates (resulting from the volumetric flow rates as the fluids are considered incompressible) are of 10.07×10^{-6} kg/s (water) and 1.22×10^{-6} kg/s (air).

4.2.3   Experimental Observations

All the experiments were performed at a single fixed flow rate for air and a single fixed flow rate for water. Contact angles of $20°$ and $105°$ were tested for both square and round sections and the case of $80°$ was tested in the square acrylic coated channel, totaling five cases with the corresponding morphologies. For the wetting case ($20°$ contact angle) in the square channel the water flows in the corners of the channel and also on the walls in the form of a thin film (~ 10 μm), while the air flows in the core. In the series of images presented, the region adjacent to the corners will appear as dark bands since the corner menisci reflect away the light, while the liquid lobes will appear bright as the light is transmitted directly into the microscope's objective lens. The "dark" or "bright" regions shouldn't be interpreted as "gas" or "liquid", rather the liquid encompasses the gas phase and curved interfaces deflect the transmitted light away from the objective lens. Bright areas indicate the absence of a curved gas-liquid interface in the ray path.

The gas-liquid interface that delimits the thin water film deposited on the inner walls presents periodic capillary shear-driven instabilities as seen in the image sequence shown in Figure 4.4. These instabilities grow into liquid lobes that travel in the direction of the flow (from right to left) at about 0.3 m/s which is close to the estimated water velocity.

As the liquid lobes grow, they tend to coalesce at a critical volume forming a liquid plug characteristic for the plug flow regime; the critical volume can be defined

69

www.manaraa.com
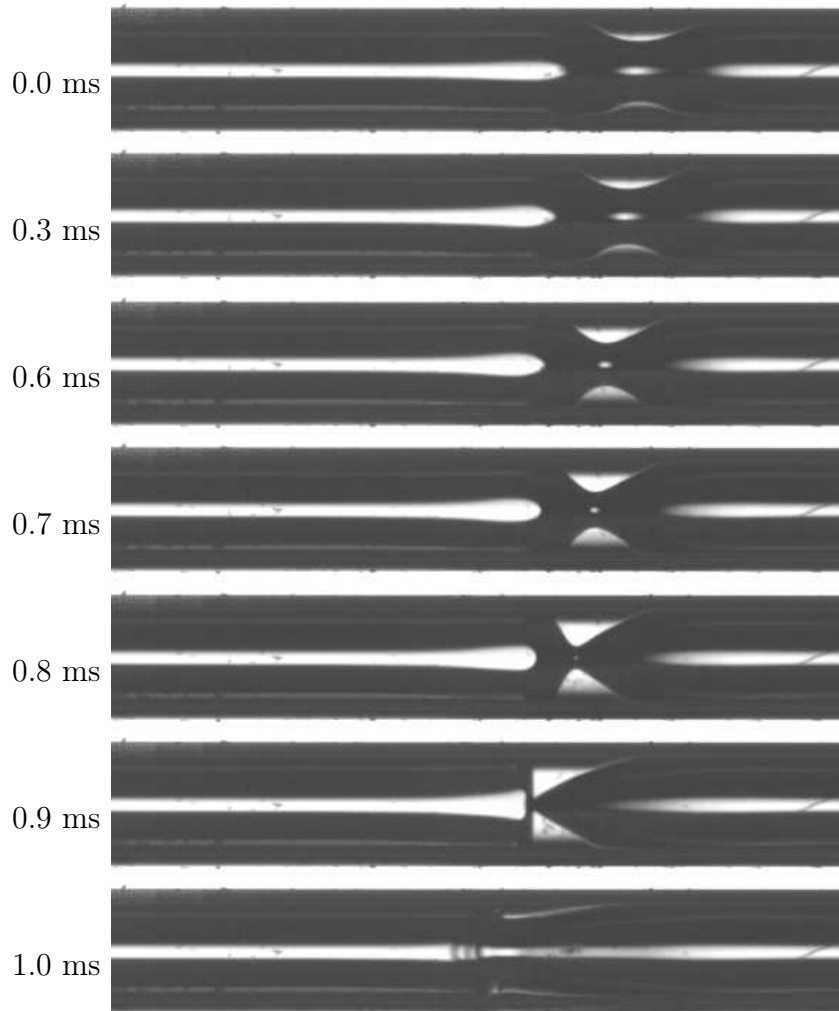
Figure 4.4. Lobe formation and collapse in a square channel, $\theta \leq 20°$. The flow is from right-to-left and the width of the images is 3.931 mm.
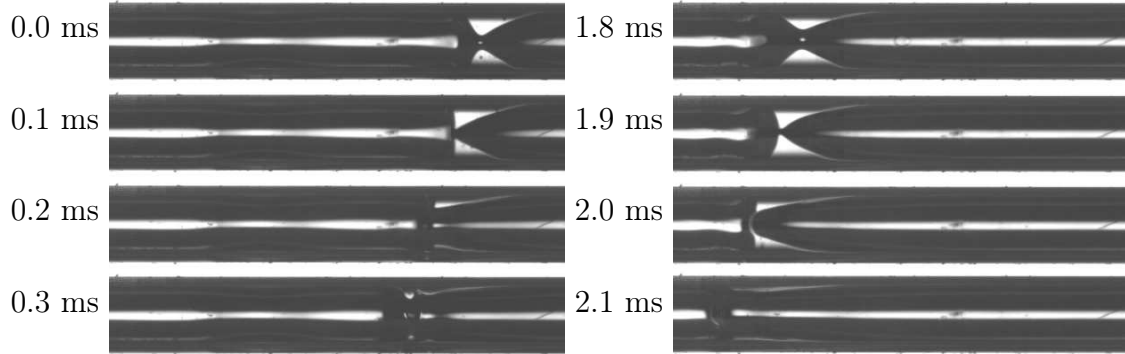
Figure 4.5. Repetitive liquid lobe formation and collapse in a square channel, $\theta \leq 20°$. The lobe collapse (left) and coalescence (right) are visible . The flow is from right-to-left and the width of the images is 3.931 mm.

as the maximum volume of liquid that can be accumulated in a lobe before turning into a plug. However, under some circumstances, coalescence of the liquid lobes may be prevented and the lobes will abruptly collapse back to the liquid film via capillary forces. This flow behavior is referred to as unsteady annular flow.

The periodicity of lobe formation is shown in the sequence of images presented in Figure 4.5, where we can see that the lobe formation and collapse occurs twice in a 2 ms time interval. The sudden collapse (left column) of the lobes may result from the capillary pressure imbalance caused by the sharp wave peak. The lobes may coalesce to form liquid plugs (right column) which are accelerated and destroyed by the gas flow. For the wetting case ($\theta \leq 20°$) in the round channel an unsteady annular flow regime was also observed. Even though the morphology is quite similar with that of the square channel flow, there are three noticeable differences we will discuss. First, the lobe collapse behavior tends to be less abrupt in the round channel and the leading edge of the lobe doesn't become perpendicular to the walls as it usually happens in the square channel. Second, the water film deposited on the walls appears to be thicker in the round channel suggesting higher average film velocity compared

71
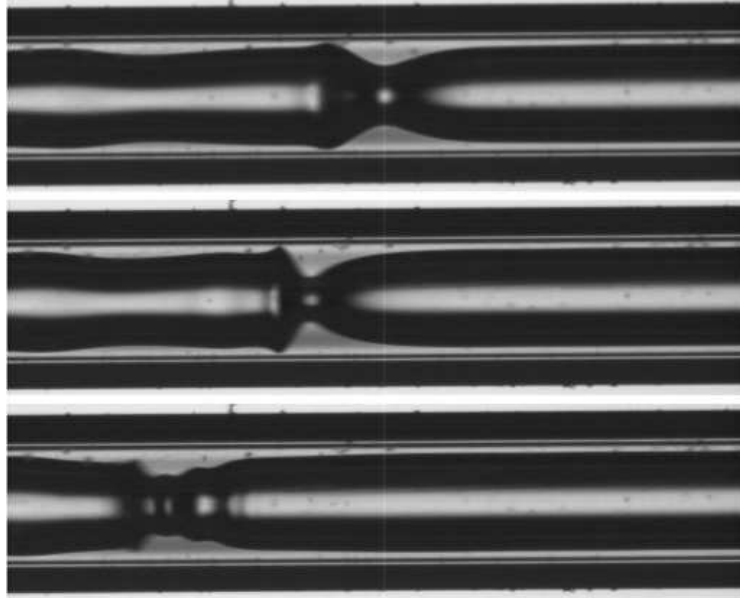
Figure 4.6. Lobe formation and collapse in a round channel,$\theta \leq 20°$. Consecutive frames 0.067 ms appart. The flow is from right-to-left and the width of the images is 3.438 mm.

to the square channel. And third, the liquid plugs that form as a result of lobe coalescence are more stable in the round channel and tend to accumulate larger volumes of water, indicating a propensity for plug flow at the same flow rates as compared to the square channel.

Lobe collapse in the round channel is shown in Figure 4.6. Notice how the leading side of the lobe remains sloped back before collapse, a behavior different from the square case where it becomes perpendicular to the walls (see Figure 4.4). The case when the lobe coalesces and forms a liquid plug is shown in Figure 4.7. The plug was stable over the 1.742 ms interval when in view, a long time considering that a lobe's collapse takes place in less than 0.1 ms.

The non-wetting case ($\theta = 105°$) of the circular channel presents a flow morphology different than in the wetting case, somewhat simmilar to the square wetting

72
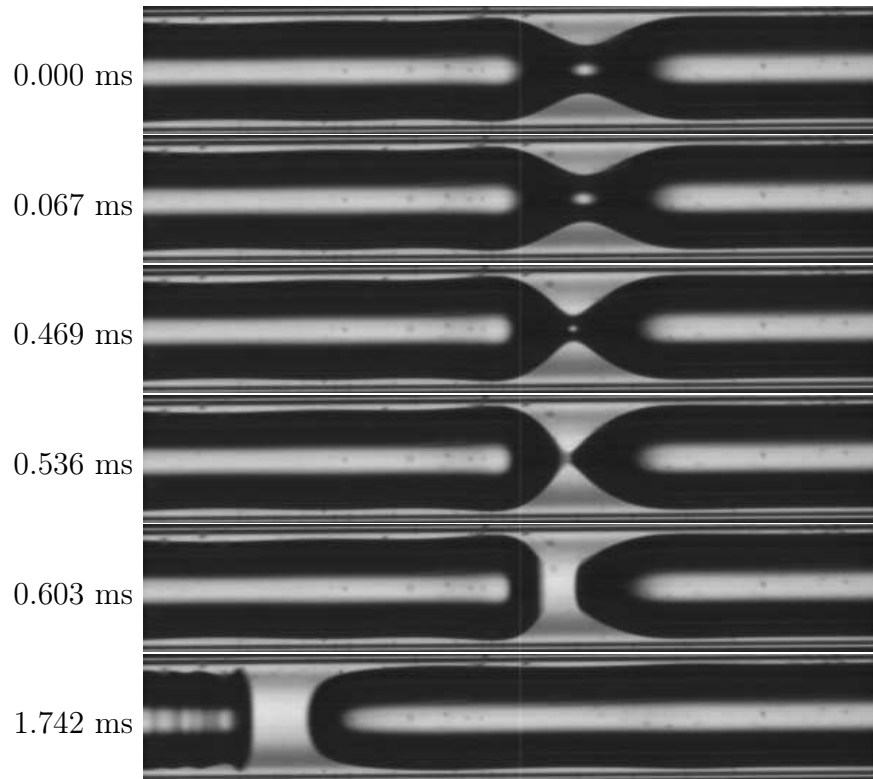
Figure 4.7. Lobe evolution and coalescence in a round channel, $\theta \leq 20°$. The flow is from right-to-left and the width of the images is 3.455 mm.
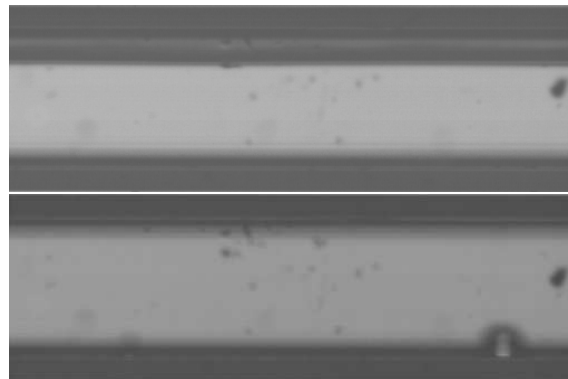
Figure 4.8. Top, separated flow in a square channel, $\theta = 105°$. The bottom picture shows the channel with no flow. The flow is from right-to-left and the width of the images is 4.198 mm.

73

case. There is little occurence of plug flow and a tendency for serpentine type of flow which normally occurs at smaller diameters in the round wetting channels. Specific for this case is the repetitive formation of liquid lenses which are pushed through the system until collapse, as shown in Figure 4.9.

The square non-wetting case ($\theta = 105°$) presents a flow morphology strikingly different from its wetting counterpart. The liquid flows on one of the walls and its adjacent corners or in the corners alone while the gas occupies the remaining volume of the channel such that the flow is completely separated. The flow is extremely stable, and the liquid may flow on any of the walls or corners respectively. In Figure 4.8 the liquid flows quiescently on a lateral wall and corners, or in the corners bounding the wall (top of image). A similar separated flow regime was previously noted by Barajas and Panton [3], and Biswas and Geenfield [80] for the case of non-wetting round and square sections, respectively.

The flow in the mixed-wetting square case ($\theta = 80°$) was extremely unstable, a mixture of plug and slug flows. Moving contact lines and film rupture with correspondingly high energy dissipation and pressure drop are characteristic to this flow regime. A liquid plug moving through the channel is shown in Figure 4.10. There is no liquid film connecting the plugs and moving contact lines are present at the leading side. Long liquid slugs with a liquid film deposited on any of the walls and a dry oposite wall are exemplified in Figure 4.11. Film rupture on one of the walls is captured in Figure 4.12.

4.2.4 Conclusion

The effects of surface wettability (contact angle) on two phase flow morphology was investigated by the means of high speed visualization, in square and round channels.

74
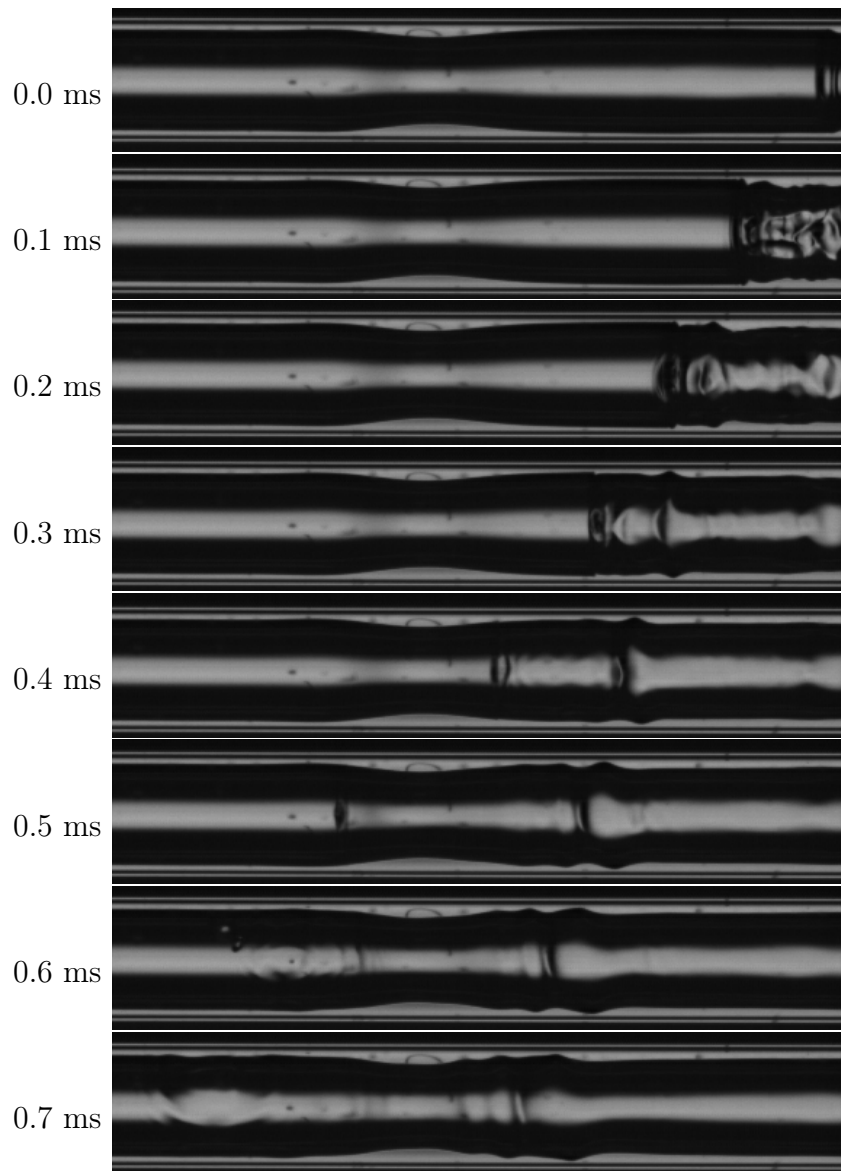
Figure 4.9. Lens formation and collapse in a round channel, $\theta = 105°$. The flow is from right-to-left and the width of the images is 6.513 mm.

75

0.0 ms

17. ms
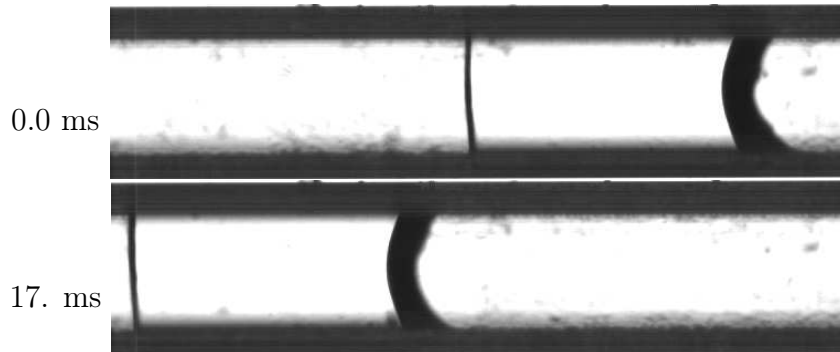
Figure 4.10. Plug flow in a square channel, $\theta = 80°$. The flow is from right-to-left and the width of the images is 2.866 mm.

0.000 s

0.498 s
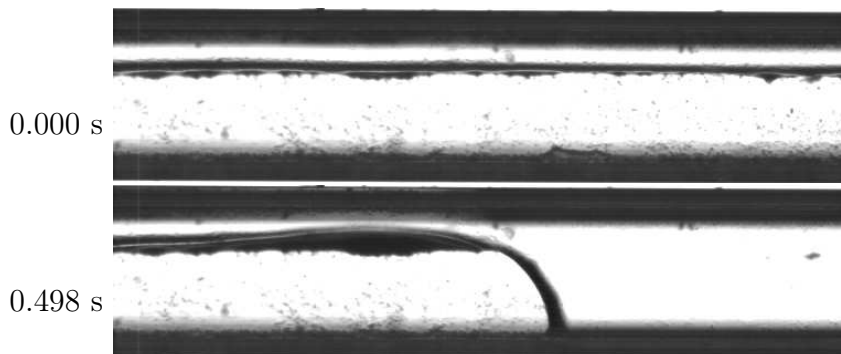
Figure 4.11. Slug flow in a square channel, $\theta = 80°$. The flow is from right-to-left and the width of the images is 2.866 mm.

76
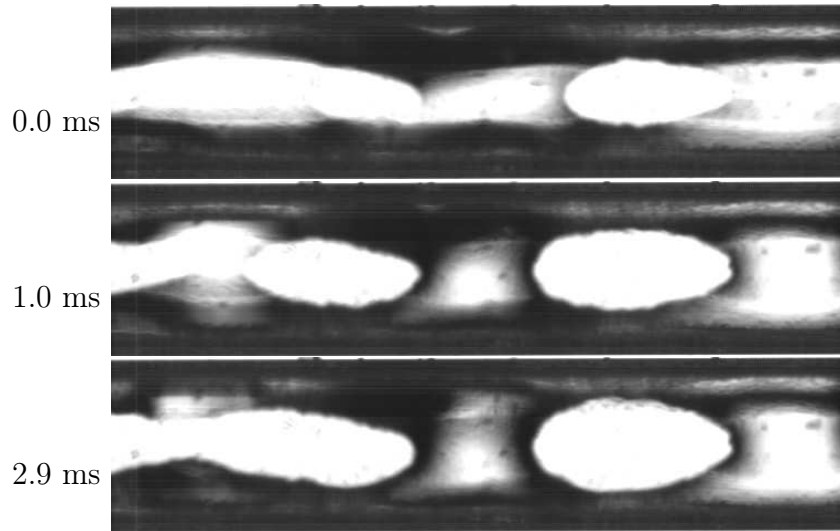
Figure 4.12. Film rupture in a square channel, $\theta = 80°$. The flow is from right-to-left and the width of the images is 2.866 mm.

For the static case it is well known that the contact angle θ is the boundary condition that sets the shape of the gas/liquid interface. It is then expected that the wetting properties play an important role in setting the two-phase low Bond number flow regimes by its influence on the gas/liquid interface shape. This fact is experimentally confirmed in the five studied cases, round and square both wetting ($\theta \leq 20°$) and non-wetting(($\theta = 105°$), and a mixed-wetting case in a square channel ($\theta = 80°$). The mixed-wetting case is a wetting case for the walls ($\theta = 80°$), but for the corners according to the Concus-Finn criterion it is also de-wetting. This behavior needs to be taken into account when studying two-phase flow in polygonal geometries.

For a fixed air-water flow rate pair four unique flow regimes are observed proving that changes in contact angle and geometry result in distinct flow behavior. Both contact angle and geometry of the cross section need to be included in a succesful model of capillary scale two-phase flow systems.

77

5. THE EFFECT OF SURFACE WETTABILITY ON VISCOUS FILM DEPOSITION

5.1 Preamble
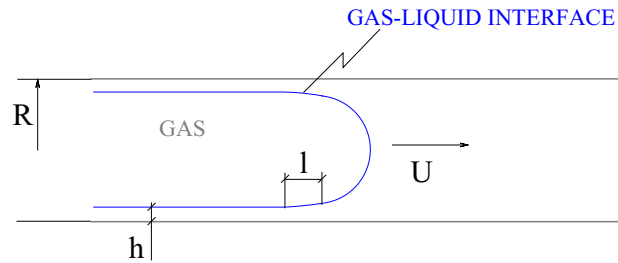
Figure 5.1. Film Deposition Schematic.

The film deposition process in a tube of radius R, described in the following paper[*], presents three fundamentally different zones as shown in Figure 5.1:

1. The quasi-spherical static meniscus translating with velocity U, where capillary forces are dominant.

2. Transition meniscus of length l, where both capillary and viscous forces are important. This zone connects the static meniscus and the film.

---

3. The deposited film of thickness h, laid on the wall at the transition meniscus.

The following chapter is republished by permission.

The viscous deposition of a liquid film on the inside of a capillary has been experimentally investigated with a focus on the relationship between the film thickness and surface wettability. With distilled water as a working fluid tests were run in a 622 microns diameter glass tube with contact angles of 30° and 105°, respectively. In the first set of experiments the tube was uncoated while in the second set a fluoropolymer coating was applied to increase the contact angle. A film thickness dependence with the contact angle θ (surface wettability) as well as the Capillary number in the form $h_R \approx Ca^{2/3}/cos\theta$ is inferred from scaling arguments. For partial wetting it may explain the existence of a thicker film for non-zero contact angle. It was further found that the non-wetting case of 105° contact angle deviates significantly from the existing theories, the film thickness presenting a weak dependence on the Capillary number. This deviation as well as the apparent non-uniqueness of the solution is thought to be caused by the film instability (rupture) observed during the tests.

The thickness of the deposited film as a function of the Capillary number was estimated from the liquid mass exiting the capillary and the gas-liquid interface (meniscus) velocity, and compared to Bretherton's data and a correlation proposed by Quere. The film thickness measurements as well as the meniscus velocity were determined with the aid of a Photron high speed camera with 10000 frames per second sampling capability coupled with a Nikon TE-2000 inverted microscope and a Precisa electronic balance.

5.2   Introduction

The age of miniaturization has brought with it an array of technical challenges pertaining to two-phase flow in microchannels, heat exchangers, lab-on-chip devices to mention a few. One of the barriers in the way of PEM fuel cell development is the flooding that occurs in the bipolar plate channels. Coating industrial processes require precise knowledge of the parameters controlling the *film thickness*, also important in oil recovery.

Fairbrother and Stubbs[22] first noted that a bubble passing through a liquid-filled tube would move at a velocity higher than the average liquid velocity. In 1942 Landau, Levich[23] and Derjaguin[24] proposed a model for evaluating the thickness of a viscously deposited film as a function of Capillary number ($Ca = \mu U/\sigma$). Later on Bretherton[25] proposed a similar law for a film deposited inside a capillary, valid for thin films and Ca smaller than 0.005. He also found experimentally that aniline ($\theta_{\text{aniline}} = 36°$) does not follow the predicted behavior and the deviation becomes increasingly important as the Capillary number decreases. Teletzke[26] proposed a theory which accounts for the conjoining/disjoining pressure potential to explain the behavior of films thinner than one micron, which cannot alone explain the deviation in Bretherton's data.

Scaling arguments which could explain this discrepancy are given in the "Results and Discussion" section. The vast majority of the viscous deposition studies had assumed perfect wetting (zero contact angle) between the liquid and the solid. What happens if the wetting is partial (non-zero contact angle)? In the following we will present experimental data collected in a range of low Reynolds and Bond numbers,

for Capillary numbers up to 0.008. The gravity and inertia are of negligible importance, the film is being deposited as a result of the competition between capillarity and viscosity.

5.3 The Experiment

(a) Schematic   (b) Actual Setup
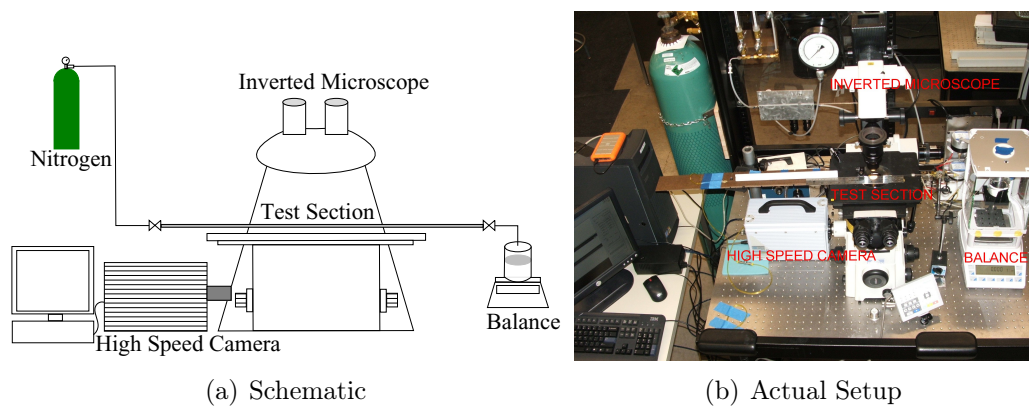
Figure 5.2. Film Measurements Setup

The experimental setup consisted of a glass capillary tube 60 centimeters long having an internal diameter of 622 microns, a Nikon TE-2000 inverted microscope, a Photron high-speed camera and a Precisa electronic balance (Figure 5.2). The capillary exit is connected through a valve with rigid tubing which is immersed in the distilled water-filled glass vessel used to weigh the expelled liquid. The nonwetting fluoropolymer coating was obtained by passing a FC-721 (3M Corporation) liquid slug through the capillary at constant velocity, with the aid of a syringe pump. For deposition velocities of 1 to 55 m/s a uniform coating of 0.05 to 0.075 μm is expected [88].

The experiment begins with the glass tube being filled with distilled water. When a valve at the test section outlet is opened the filtered compressed nitrogen pushes the liquid out of the capillary while a thin film is left on the wall. The experiments are run on 40-50 centimeter lengths by opening and closing the exit valve. The meniscus velocity is measured using the recording from the high-speed camera coupled to the microscope. The length of the run is recorded and the expelled liquid mass is measured immediately after the exit valve is closed. The mass reading is obtained from the electronic balance to within 0.5 mg. Evaporation precautions are taken and it is not expected to contribute to the mass measurement error. The entire setup is placed on a vibration isolation table and the glass vessel where the water exiting the capillary is collected sits under a shield which encloses the testing space of the balance. All tests were run at a temperature of 20°C.

The film thickness is then calculated with the formula:

$$h_R = 1 - \frac{1}{R}\sqrt{\frac{m}{\rho\pi L}} \qquad (5.1)$$

where h_R is the non-dimensional film thickness, R is the capillary radius, m is the expelled liquid mass, ρ is the mass density and L is the length of the run.

In the first set of experiments the capillary was uncoated while in the second set there was a FC-721 coating applied. The contact angle for bare glass-water is 30° and for the fluoropolymer coating-water the contact angle is 105° (given by the manufacturer and also measured in the lab).

83

5.4   Results and Discussion

For all tests only one capillary was used, which was coated for the second round to investigate the nonwettting film deposition. The Bond number based on the tube radius was 0.013 and the gravity effect can be safely neglected. The Weber number ranged from 4e-4 to 1.45 and the Reynolds number varied from 3 to 180, indicating that the inertia of the liquid column needs to be carefully considered for the role it might play in the physics of viscous deposition. Evidently, although water has a low viscosity there would be no deposition in the absence of viscosity and the term *viscous deposition* legitimately describes the physics of the phenomenon. Ca is the parameter traditionally used to describe the film thickness variation with velocity and ranges from 1.4e-4 to 0.008 in present experiments.

All tests were performed at 20°C and the properties of water at this temperature are $\sigma = 72.73 mN/m$, $\mu = 0.001 Pa - s$ and $\rho = 998.2 kg/m^3$.

The experimental results for water on bare glass compared with data of Bretherton [25] are presented in Figure 5.3. We mention herein that Bretherton's theory assumes a 0° contact angle (perfect wetting) while his data is obtained using fluids which do not perfectly wet the wall of the tube. For thicker films Quere proposed a correlation [8] which is shown as a broken line and follows closely Bretherton's law for the considered Ca range. For water with 30° contact angle (circles) the data fits Bretherton's law (solid line) to within 10% for Ca exceeding 0.001 and it appears to confirm the deviation observed for aniline when the Capillary number is below 0.001. Bretherton's data for aniline (squares) and benzene (down triangles) illustrate the discrepancies which occur for different surface wettabilities (contact angles of 36°

84
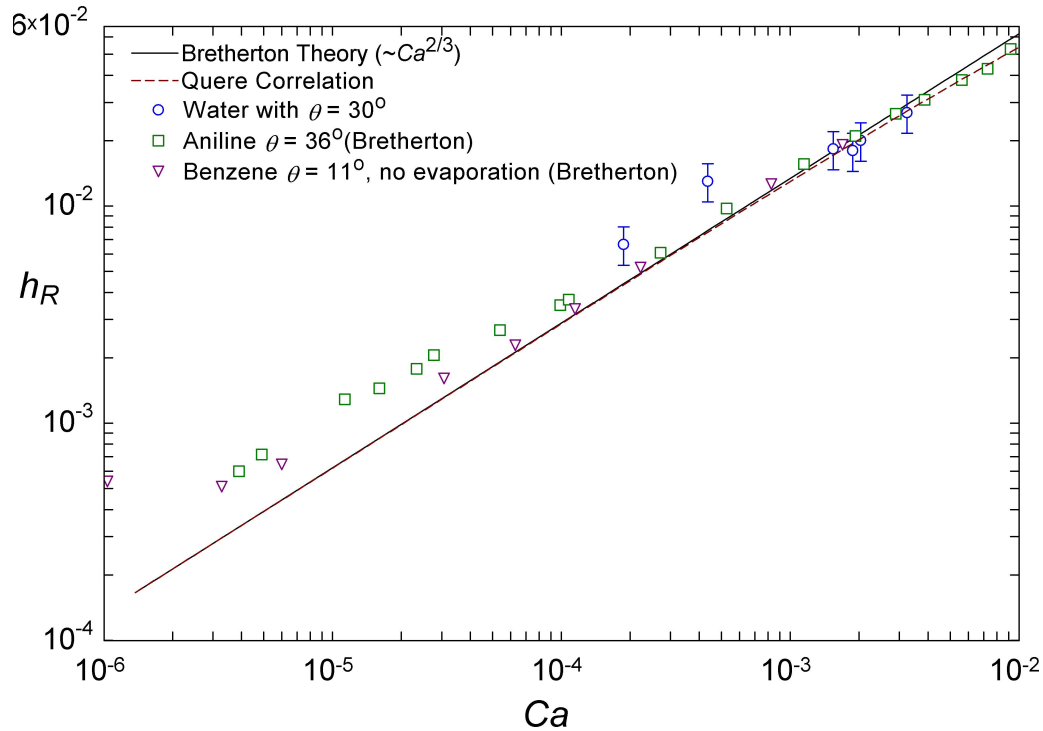
Figure 5.3. Non-dimensional film thickness vs. Ca, the wetting case.

and 11°). A quantification to account for partial wetting cannot be made at this time due to insufficient accuracy of the present method, instead scaling arguments are proposed to support the film thickening experimental observations.

For low Ca and negligible inertia the gas-liquid interface in a low Bo system is expected to keep a spherical shape up to the wall where it merges through a transition region of length l with the deposited film. In the transition region the viscous contribution has to be balanced by the pressure gradient due to varying curvature (surface tension component) $\mu U/h^2 \approx \sigma k/l$, where h is the film thickness and k is the meniscus curvature. The meniscus curvature matches the curvature of the transition zone where the two merge, $h/l^2 \approx k$ and the meniscus curvature is

85
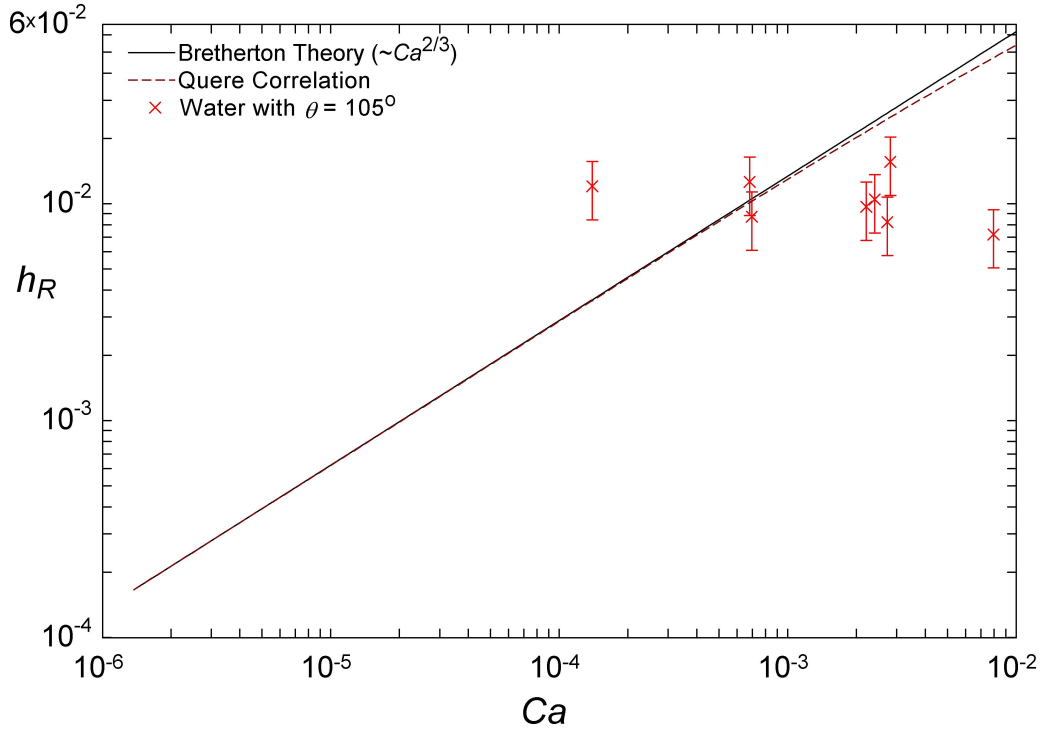
Figure 5.4. Non-dimensional film thickness vs. Ca, the nonwetting case.

$k = cos\theta/R$ as long as the apparent contact angle retains a value θ. From these arguments it can be inferred a non-dimensional film thickness of the form:

$$h_R \approx \frac{Ca^{2/3}}{1 - \theta^2/2} \tag{5.2}$$

which would account for wetting film deposition such in the case of aniline. The arguments seem to hold for a moderate contact angle ($< 36°$) and while the film thickness is greater than one micron (while the disjoining/conjoining pressure terms are negligible).

Film thickening for low viscosity fluids due to inertia has been investigated by

86

Aussillous and Quere [8] who proposed a critical Capillary number Ca^* above which inertial effects become noticeable. In present experiments the maximum Ca is 0.008 while $Ca^* > 0.01$ therefore inertial effects are not expected to increase the film thickness. It is even less expected they would become important with decreasing Ca (velocity).

The non-wetting film deposition data is shown in Figure 5.4. Water on FC-721 coated glass presents a 105° contact angle and the deposited film has a non-dimensional thickness of approximately 0.008 which appears to not vary considerably with Ca within the range investigated. This behavior deviates significantly from the predictions of the existing theories and signal that entirely different physics is involved when deposition takes place on a non-wetting surface. The film is generally much thinner than predicted for Ca exceeding 0.001 and appears to increase slightly at lower Ca. The scatter in the data might suggest a non-unique solution for this deposition problem, although the error associated with the experimental method needs to be excluded to validate this hypothesis. Experimental observations regarding the film stability suggest that a non-unique solution for the nonwetting film thickness is possible. In Fig. 5.5 it is shown a typical nonwetting film behavior while it is deposited by a liquid column flowing from left to right. In the first three images from the top the meniscus travels with velocity $U = 0.2246\ m/s\ (Ca = 3.09e - 3)$ and a film is deposited on the wall. In the fourth image the film begins to rupture and the newly formed contact line which delimits the trailing film translates with $0.0229\ m/s$. The film rupture is complete in $36.1\ ms$ and it takes place several times during the experiment run.

If we compare the wetting and the non-wetting deposition the film stability rep-
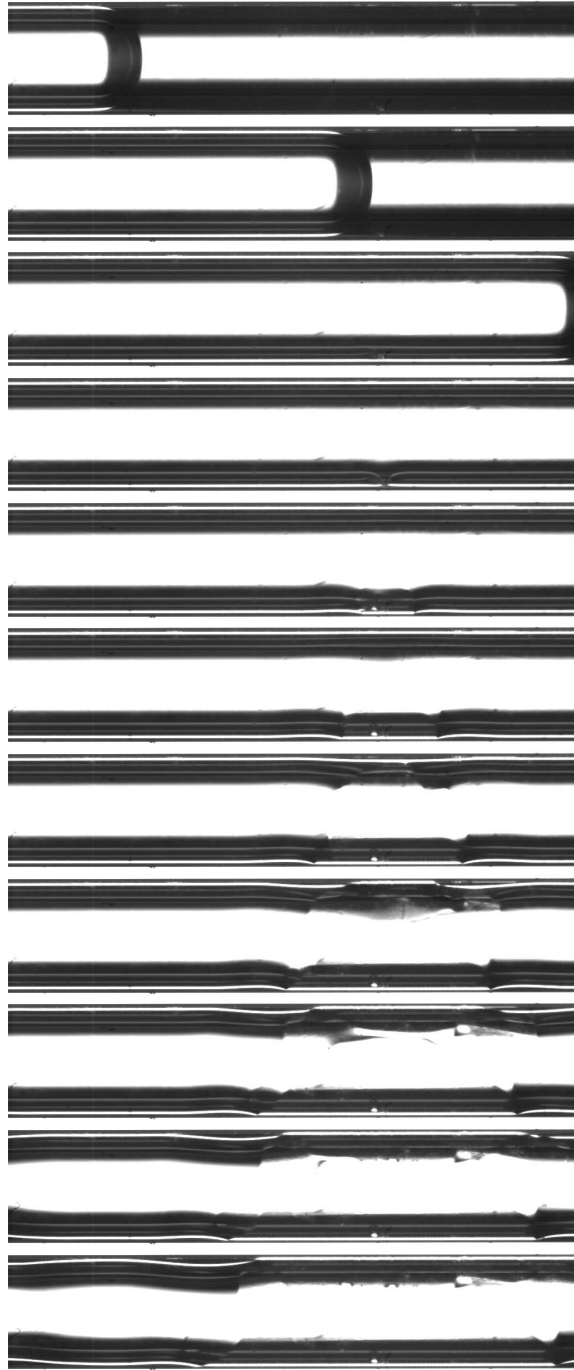
Figure 5.5. Viscous film deposition in a nonwetting capillary, $\theta = 105°$. Image width of 4.427 mm. Consecutive images 8.032 ms appart.

88

resents a noticeable difference which is likely to change the physics involved in the process. Indeed, a Plateau-Rayleigh instability time scale [58] for our wetting test section-working fluid is on the order of 58 s which is much longer then the time of a test run and it is unlikely to play a role in the deposition. In the non-wetting case however, the film rupture occurs in a much shorter time and it was observed to occur repeatedly during a test run, possibly interfering with the mechanisms at play in the wetting deposition.

5.5 Conclusion

The film deposition behavior observed by Bretherton departs from his theory in an unexpected way, behavior experimentally confirmed in present investigation for the case of water in a glass capillary ($\theta = 30°$). Scaling arguments derived herein suggest a non-dimensional film thickness dependence with the contact angle θ (surface wettability) as well as the Capillary number in the form $h_R \approx Ca^{2/3}/(1 - \theta^2/2)$. Based on the work of Aussillous and Quere[8] the liquid column inertia was neglected for the Ca range investigated.

The effect of wettability was further investigated for a high contact angle ($\theta = 105°$) which yielded a non-wetting film deposition behavior that departed significantly from the existing theories, developed under the perfect wetting $\theta = 0°$ assumption. It was found that the non-dimensional film thickness presents a weak dependence on the Capillary number and has an average value of $h_R = 0.008$. Experimental observations suggest that the film stability could cause the reported behavior since film rupture occurred repeatedly in any given test run. On the other hand,

film rupture or even destabilization was not observed during the wetting deposition experiments: the time scale of a Plateau-Rayleigh instability is much longer than the time required for any of the performed tests.

Further experiments with improved accuracy need to be perfected in order to quantify the non-dimensional film thickness dependency on surface wettability. Improved accuracy is also desirable to distinguish between error-caused versus non-unique film thickness solution suggested by the scatter in the nonwetting data.

6. Non-wetting Annular Films. Flow Morphology and The Shock Condition

The nature of film deposition in circular glass capillaries of 500 μm diameter is investigated experimentally by considering two surface wettabilities: wetting with static contact angle of 30° (water on glass) and non-wetting with static contact angle of 105°. A liquid film is deposited behind a moving meniscus, the finite length film ends in a ridge that also moves in the direction of the flow. The ridge is bounded by a moving contact line and it translates over the deposited film. There are notable dissimilarities in the film deposition behavior when the surface wetting is changed, the non-wetting film is significantly thicker than the wetting film. Taylor bubbles, also differentiated by wettability, form due to the growth of the ridge. At a given Capillary number, the contact line velocity is as much as twice as large for the non-wetting case. The dynamics of the deposition process is studied experimentally and a criterion is proposed to explain the occurrence of a shock (hydraulic jump) in the non-wetting film connecting the ridge to the meniscus. A hydraulic jump forms in the film when critical conditions are attained, as defined by a non-dimensional

91

parameter similar to the Froude number. The film thickness is then calculated directly from the experimental data and a correlation is obtained by matching the measured and the theoretical shock velocities.

6.1   Introduction

Film deposition processes captured the interest of researchers due to both their fundamental aspects, as well as for their numerous applications ranging from oil extraction to microfluidic devices. The study of film deposition (the infinite bubble case) is also a necessary step in understanding the interface behavior associated with the Taylor bubble flow regime. Taylor bubble flow is defined as finite length gas bubbles longer than the tube diameter alternating with liquid plugs.

Fairbrother and Stubbs[22] first noted that a bubble passing through a liquid-filled tube would move at a velocity higher than the average liquid velocity. In 1942 Landau, Levich[23] and Deryagin[24] proposed a model for evaluating the thickness of a viscously deposited film as a function of Capillary number ($Ca = \mu U / \sigma$). Later, Bretherton[25] proposed a similar law for a film deposited inside a capillary, valid for thin films and Ca smaller than 0.005. He also found experimentally that aniline ($\theta_{\text{aniline}} = 36°$) does not follow the predicted behavior and the deviation becomes increasingly important as the Capillary number decreases. Teletzke [26] proposed a theory which accounts for the conjoining/disjoining pressure potential to explain the behavior of films thinner than one micron. Aussillous and Quere [8] examined the role of inertia and extended Bretherton's law for higher Ca, matching Taylor's experimental data.

92

Snoeijer et al. [27] showed that the thickness of a film coating a plate withdrawn from a liquid reservoir depends on surface wettability. They proved that the film thickness can have two solutions for the partial wetting case. Most notably Snoeijer et al. [89] found that a ridge ending with a hydraulic jump occurs at the end of a plate deposited film (under partial wetting, $\theta \approx 50°$), which is to some extent similar to the experimental findings presented herein. In present experiments a hydraulic jump was observed in the film during the inside-of-tube deposition under non-wetting conditions ($\theta = 105°$).

Schwartz Schwartz et al. [28] examined the infinite and finite bubbles in low Ca flow and found that the short bubble film obeys Bretherton's law while the long bubble film is almost twice as thick; for intermediate bubble length the film thickness presented multiple solutions possibly due to instabilities. Herescu and Allen[29] observed that the film thickness increases with a contact angle having low wetting values($\theta = 30°$), while for a non-wetting contact angle of $105°$ the film thickness departed markedly from Bretherton's law. Changes in film thickness can be brought about by Marangoni stresses which occur at the gas-liquid interface due to the presence of contaminants. There is no general agreement as to what are the conditions when the film thickness increases or decreases, it is certain though that surface tension gradients can cause changes in the film thickness. Marangoni effects on film deposition were studied by Ratulowski[30], Ramdane and Quere [31] as well as Krechetnikov and Homsy [32]. In present experiments the film thickness increased significantly for the non-wetting case ($105°$ contact angle) which is believed to be caused by the dynamics of the moving contact line rather than Marangoni stresses.

93
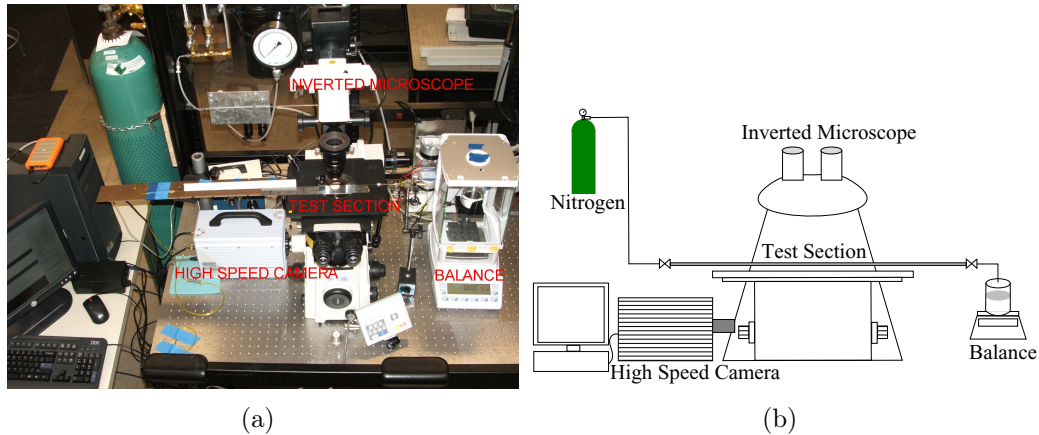
Figure 6.1. Experiment Setup

6.2   Description of the Experiment

The experimental setup consisted of a glass capillary tube 12 centimeters long having an internal diameter of 500 microns, a Nikon TE-2000 inverted microscope, a Photron high-speed camera and a Precisa electronic balance (Figure 6.1). The capillary exit is connected through a valve with rigid tubing which is immersed in the distilled water-filled glass vessel used to contain the expelled liquid. The nonwetting fluoropolymer coating was obtained by passing a Rain-X$^{\text{TM}}$(3M Corporation) liquid slug through the capillary at constant velocity, with the aid of a syringe pump. The coating obtained yields a static contact angle of 105° for water. The experiment begins with the glass tube being filled with distilled water, after which the desired gas pressure is set while keeping the outlet valve closed. When the valve at the test section outlet is opened the filtered compressed nitrogen pushes the liquid out of the capillary while a thin film is left on the wall. The gas-liquid interface dynamics is recorded through the 2X microscope objective at a location 7-8 centimeters down-

94

stream of the initial meniscus position, with the aid of the high speed camera. The experimental error for velocity and length measurements is within 5% for all data.

6.3   Experimental Observations

Figure 6.2. Hydraulic Jump in a Non-Wetting Film

Film deposition experiments were performed with distilled water in a 500 μm glass round capillary, with and without a Rain-X coating. A water droplet sitting on the Rain-X coated glass makes a static contact angle of 105° (*non-wetting*) and a static contact angle of 30° on a glass surface (*wetting*, commonly denoted as *partial wetting*, *perfect wetting* being the 0° contact angle) . During the wetting experiments a Bretherton film of uniform thickness is deposited in the glass tube, with the non-dimensional thickness given by Bretherton's [25] law $h/R \equiv h_R = 1.34$ $\text{Ca}^{2/3}$ which is valid for $\text{Ca} \leq 0.005$.* A contrasting behavior has been observed for the film deposited in the non-wetting capillary. The film is thicker than in the uncoated glass capillary case (implicitly thicker than the Bretherton film if we assume the law is valid in a wetting tube) and ends with a ridge, which subsequently grows to form a plug and give rise to Taylor bubbles. If a certain velocity is attained, the film

---

* A similar correlation valid up to Ca = 0.01 is proposed by Aussillous and Quere [8] in the form $h_R = 1.34$ $Ca^{2/3}/(1 + 1.34 \ 2.5Ca^{2/3})$.

95
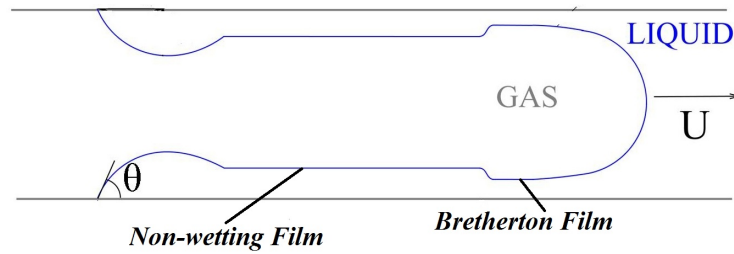
Figure 6.3. Hydraulic Jump Schematic. The thicker non-wetting film is separated by the Bretherton film through a hydraulic jump.

thickness presents an abrupt jump through which the Bretherton film deposited at the meniscus connects with the thicker film merging into the ridge (Figures 6.2, 6.3). The gas bubble appears dark with a bright band along the centerline. The liquid plug, the thin film surrounding the bubble as well as the ridge appear bright with the gas-liquid interface delimiting the dark bubble region.

A hydraulic jump (shock) is observed in the film for a number of tests performed in the non-wetting test section, while in the bare glass tube no hydraulic jump was present in the tested Ca range [†] ($0.00196 \leq$ Ca ≤ 0.0098 for bare glass and $0.0026 \leq$ Ca ≤ 0.0075 for the non-wetting section, where Ca is based on the meniscus velocity). For both surfaces (wetting and non-wetting) the ridge grows to eventually form a plug and Taylor bubbles. In the bare glass tube the bubbles are much longer than in the non-wetting tube, approaching the infinite bubble case. There are also noticeable differences in the morphology of the deposited film. The non-wetting case presents a hydraulic jump if a critical velocity is exceeded. Below this velocity the hydraulic jump does not occur and the deposited non-wetting film is thicker than the wetting Bretherton film. Also the bubbles are much shorter in the non-wetting

---

[†] The Ca range is limited in the lower limit by the minimum deposition velocity, below which a film cannot be deposited. The highest Ca tested is within the validity range of Bretherton's law, beyond this limit inertial effects would become noticeable.

96
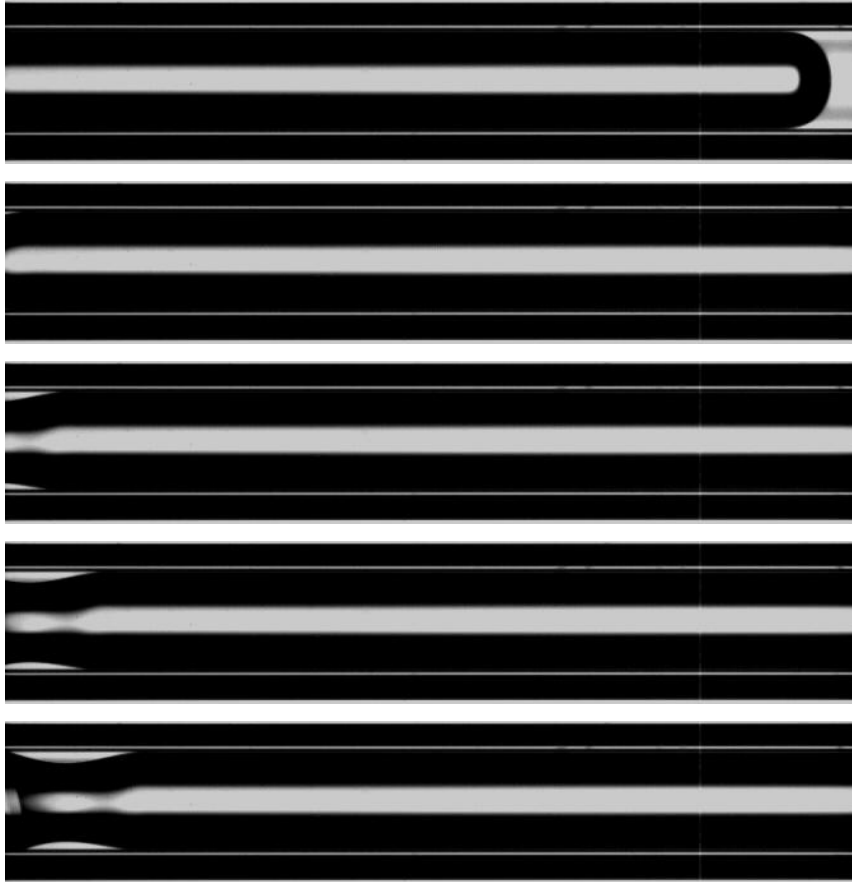
Figure 6.4. Wetting Taylor bubble , Ca = 0.0034. Images 4 ms apart. The width of the images is 5.74 mm.
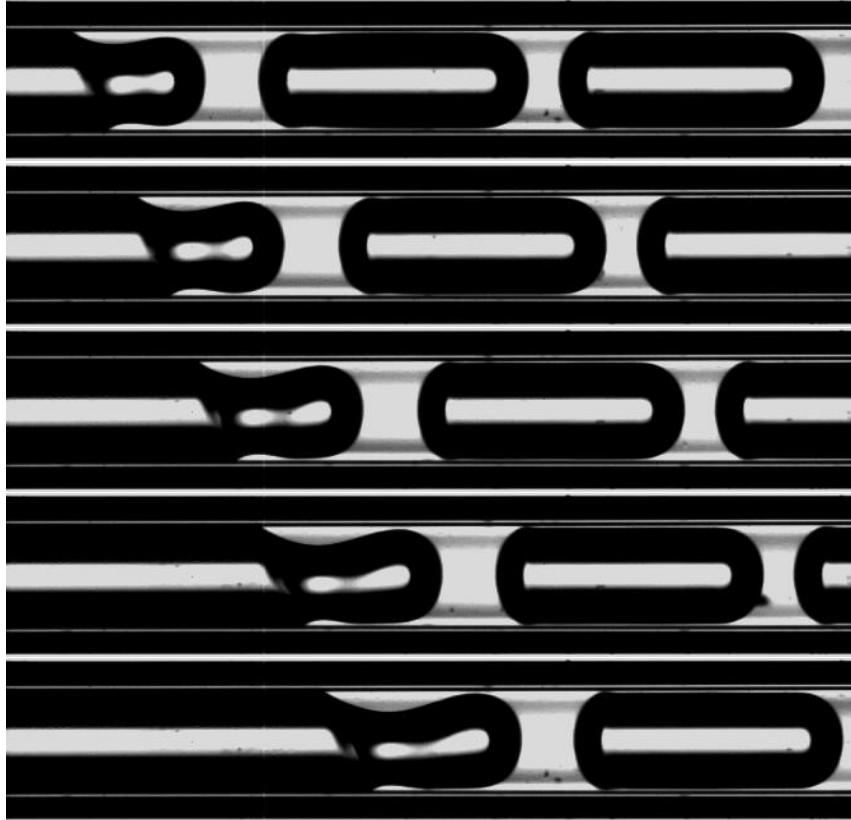
Figure 6.5. Non-wetting Taylor bubble , Ca = 0.0037. The images are captured every
2 ms. The width of the images is 5.74 mm.
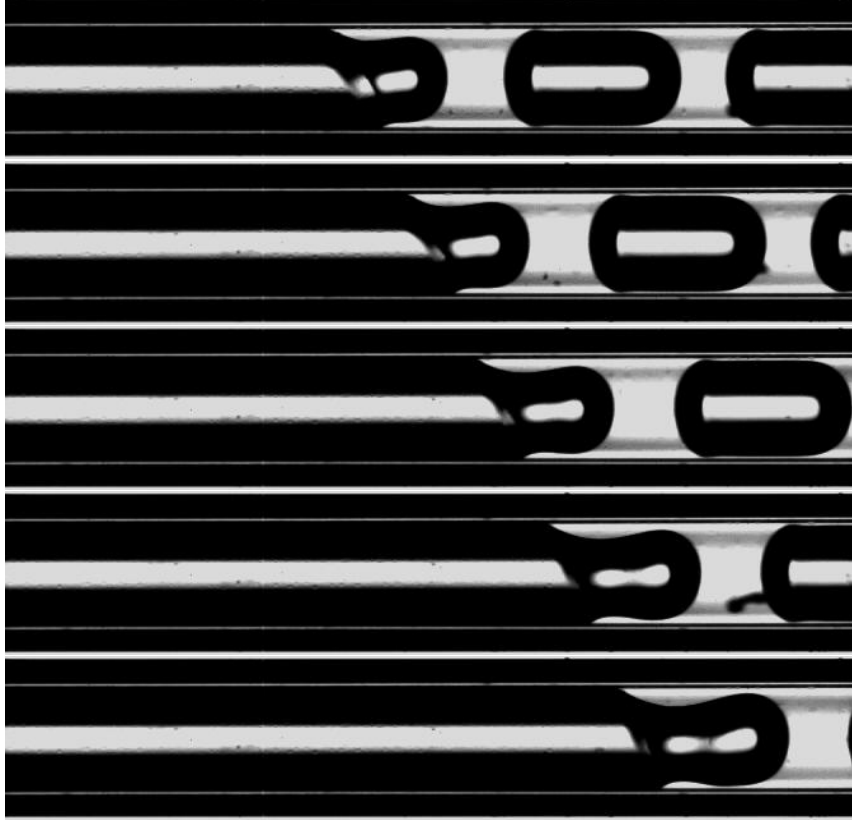
Figure 6.6. Non-wetting Subcritical Taylor bubble (no hydraulic jump), Ca = 0.004. $(U - U_{CL})/c^*$=0.417. Images 2 ms apart. The width of the images is 5.74 mm.

tube. The sequence of images in Figure 6.4 shows the film deposition in the bare glass tube, a very long bubble (approximating the infinite bubble) will eventually form when the ridge grows into a plug. Note the uniform thin film that is laid by the translating meniscus at a Capillary number of Ca = 0.0034. On the other hand, if we examine the Taylor bubbles in the non-wetting tube at a similar Ca we observe they are considerably shorter than the wetting counterparts (Figure 6.5). Also, the non-wetting film appears to be thicker than the wetting film.

The shock theory proposed herein states that the critical shock velocity of a

99
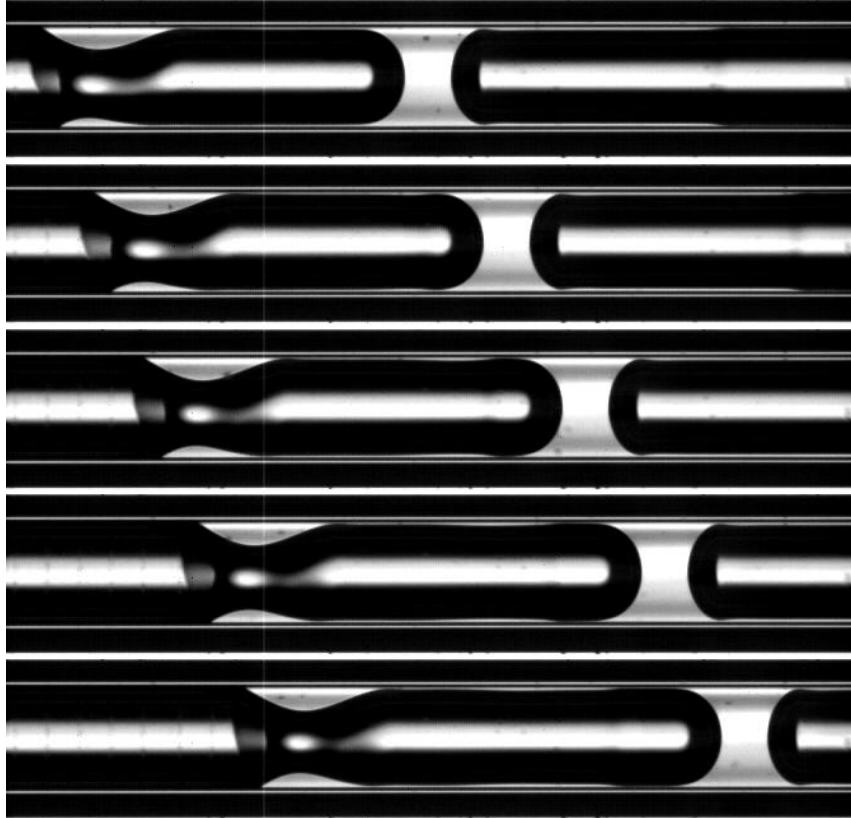
Figure 6.7. Non-wetting Supercritical Taylor bubble (with hydraulic jump), Ca = 0.00357. $(U - U_{CL})/c^*$=0.95. Images 2 ms apart. The width of the images is 5.74 mm.

hydraulic jump in a cylindrical film is a function of the deposited film thickness. It follows that with increasing Ca the hydraulic jump cannot form unless a critical velocity c^* is reached. This appears to be supported by the experiments. In Figures 6.6 and 6.7 the hydraulic jump does not occur unless the critical velocity is reached, despite the fact that Ca has a larger value in Figure 6.6. In the non-wetting case, the bubble length as well as the film morphology change when a critical velocity is exceeded. To exemplify this behavior, we show in Figure 6.6 a sequence of images taken at Ca = 0.004 with no hydraulic jump present. In the same experimental run a hydraulic jump occurs at Ca = 0.00357 as seen in Figure 6.7, visible in the formed bubble. Note the shorter bubble length as well as the thicker film for the sub-critical case (no hydraulic jump). The film thickness presents a jump when critical conditions are reached (hydraulic jump). An *ad-hoc* shock criterion requires that $(U - U_{CL})/c^* \gtrapprox 1$, where c^* will be derived in the following. We can readily see that at a larger Ca=0.004 the hydraulic jump does not occur since $(U - U_{CL})/c^*$=0.417 while at a smaller Ca = 0.00357 the hydraulic jump is present when $(U - U_{CL})/c^*$=0.95. The non-dimensional parameter $(U - U_{CL})/c^*$ is similar to the Froude number for characterizing the hydraulic jump, which in this flow is a capillary pressure gradient.

6.4   Critical Speed Scaling

It is interesting to revisit the classical shallow water wave theory to possibly gain some insight into the hydraulic jump under investigation. Froude predicted that a hydraulic jump will be present whenever the velocity exceeds a critical value

101

$c_{Fr} = \sqrt{gh}$ (critical wave speed), the Froude number being defined as the ratio $V/\sqrt{gh}$. The physics of shocks in planar films on the order of 1 mm is governed by the Froude velocity and at the same time the characteristic scale is the capillary length $\sqrt{\sigma/\rho g}$. For a capillary tube the characteristic scale for the process is the tube radius instead. We can then make an analogy with the Froude wave speed if we replace the capillary length with the tube radius. The result is a critical wave speed in the form $(1/R)\sqrt{\sigma/\rho}\sqrt{h}$ which scales as $\sqrt{h}$ and is similar to the expression derived by a shock analysis in the next section (Eqn. 6.4). From a physical stand point this implies that the shock mechanism for an annular micron-thick film is capillary drainage, as opposed to gravity drainage for mm-thick planar films. It is also important to note that this type of hydraulic jump is specific to the annular geometry since the capillary drainage is performed through the azimuthal curvature gradient in the film.

6.5   Hydraulic Jump Equations

The film presents an annular ridge at the trailing end, bound by a moving contact line which initially defines the edge of the gas-liquid interface (meniscus). The film presents an abrupt change in thickness once a critical state is attained as illustrated in Figure 6.8(a). The transition in film thickness has the appearance of a hydraulic jump which can be physically described by writing the conservation of mass and momentum across the shock. The liquid film from the ridge side has a velocity V_2 and flows over a stagnant film (Figure 6.8(b)), while the wave front travels at a velocity c. In a reference frame translating with c, the film deposited by the meniscus (having

102

thickness e) enters the shock with a velocity c which changes to $c-V_2$ after the jump.

(a) Hydraulic Jump High-Speed Image   (b) Hydraulic Jump Schematic
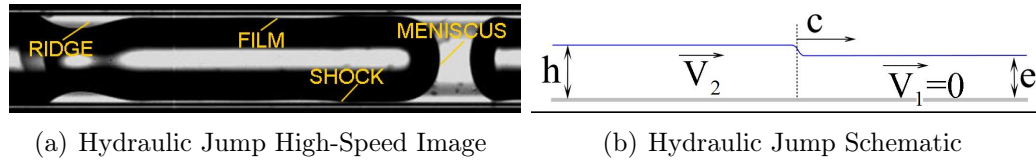
Figure 6.8. Hydraulic Jump in a Non-Wetting Film

The classical treatment of a hydraulic jump is to write the conservation laws across it. The following hypotheses are made when the conservation of mass and momentum are written across the shock:

1. Wall shear and shear at the gas-liquid interface are neglected.

2. The azimuthal curvature gradient is driving the shock.

We can now write the conservation of mass:

$$2\pi Rec = 2\pi Rh\left(c - V_2\right) \tag{6.1}$$

And the conservation of momentum:

$$\rho 2\pi R\left[-c^2 e + \left(c - V_2\right)^2 h\right] = 2\pi Rh\sigma\left[\frac{1}{R-h} - \frac{1}{R-e}\right] \tag{6.2}$$

103

From the above Eqn. 6.1 and 6.2 it follows that the wave front velocity varies as:

$$c^2 = \frac{\sigma}{\rho} \frac{h^2}{e(R-h)(R-e)} \tag{6.3}$$

The critical wave front velocity is obtained when $e = h$:

$$c^* = \frac{1}{R-h} \sqrt{\frac{\sigma}{\rho}} \sqrt{h} \tag{6.4}$$

When the ridge film velocity $V_2 > c^*$ the thin annular film deposited by the meniscus will connect to the ridge through a hydraulic jump. Note that the critical wave front velocity predicted by Eqn. 6.4 varies as $\sqrt{h}$ confirming the Froude analogy made in the previous section.

Note the difference between the shock velocity and critical shock velocity: the former is the velocity at which the wave front translates, while the latter is the minimum attainable wave front velocity, the existence limit of a hydraulic jump. The wave front velocity U_S (the shock velocity), is plotted in Figure 6.9 as a function of the deposited film thickness h_R (Bretherton film thickness non-dimensionalized by the tube radius) for the non-wetting test section. The Froude critical velocity [58] as well as the shock prediction proposed for an interface curvature gradient driven hydraulic jump are shown as a dotted line and as dash-dot line, respectively. The measured shock velocity U_S data points are located above the critical shock velocity line as expected. Another validation comes from the calculated shock velocity performed using the shock Equation 6.4 and the measured film thickness. It also

104
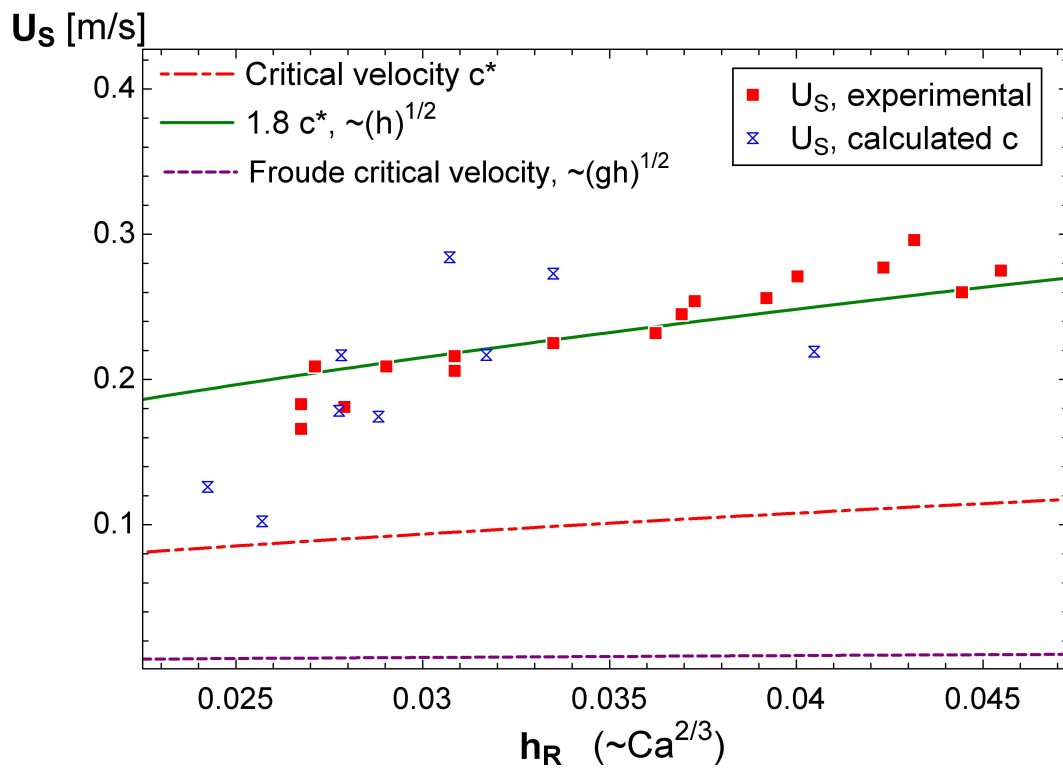
Figure 6.9. Shock Velocity vs. Nondimensional Film Thickness. $U_S, experimental$ is the shock velocity measured in a number of separate runs in the non-wetting test section. $U_S, calculated$ is the shock velocity computed with the shock theory relation Eqn. 6.3 using the measured film thickness. All data points lie above the critical shock velocity c^* which is computed using Eqn. 6.4 . Bretherton's film thickness h_R dependency on Ca is given as a correlation by Aussillous and Quere [8].

serves as a validation for the film thickness measurement method. All calculated shock velocity data follow the same trend as the measured U_S with the exception of the two leftmost points which were computed with inputs from transitional tests in which a hydraulic jump was not observed. Although these two points are still above the critical shock velocity line a transition region should exist, with this instance being representative. At the same time the error associated with the film thickness measurements is within 20% and may cause some shift in the data. The critical velocity data was taken in a number of tests spanning a month to check for repeatability and possible coating degradation. A hydraulic jump (shock) in the film was observed for a number of tests performed in the non-wetting test section, while in the bare glass tube no hydraulic jump was present in the tested Ca range. For the uncoated section 0.0018≤ Ca ≤0.009 and for the non-wetting the tests were in the interval 0.0026≤ Ca ≤0.0075. The experimental U_S can be correlated with a $\sqrt{h}$ law although the 1.8 c^* line appears to deviate to some extent from the data trend. This would imply per the shock Equation 6.4, that the actual to Bretherton film thickness ratio should be a function of Ca, which we will check *a posteriori*.

6.6   Shock Velocity and Film Thickness Correlations

The shock velocity is better described by a correlation in the form:

$$U_S = 3.8 \ h_R^{0.833} \tag{6.5}$$

which is shown in Figure 6.10 as a solid line. Note that the multiplier "3.8" in the above correlation has dimensions of velocity. $h_R = h/R$ is the non-dimensional
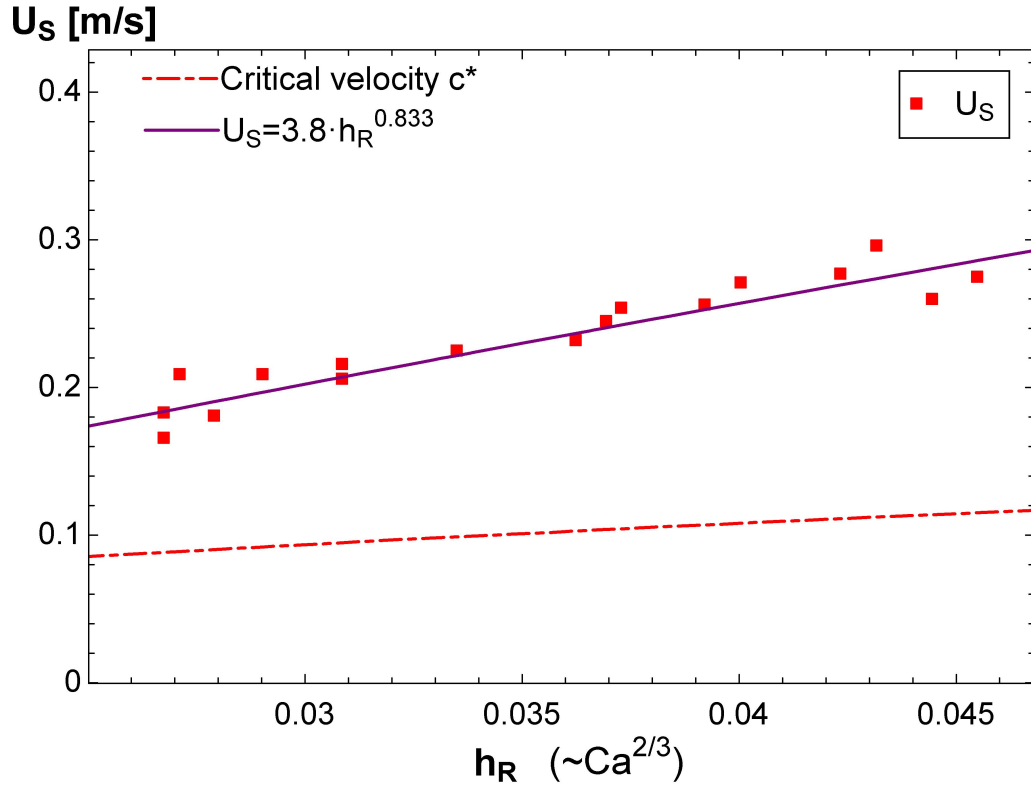
Figure 6.10. Shock Velocity vs. Non-dimensional Bretherton Film Thickness

wetting Bretherton film thickness, which is given in the literature as a function of Ca [8]. Expression 6.5 accounts for the actual to Bretherton film thickness ratio dependence on Ca, and it can be obtained in a non-dimensional form if the shock velocity U_S is scaled by the critical shock velocity c^*(Eqn.6.4). The correlation is shown in Figure 6.11:

$$\frac{U_S}{c^*} = 7 \ h_R^{1/3} \tag{6.6}$$

Experimental observations indicate that the non-wetting film is much thicker than the Bretherton film and the measurements confirm this. The question arising

107

U$_S$ / c*
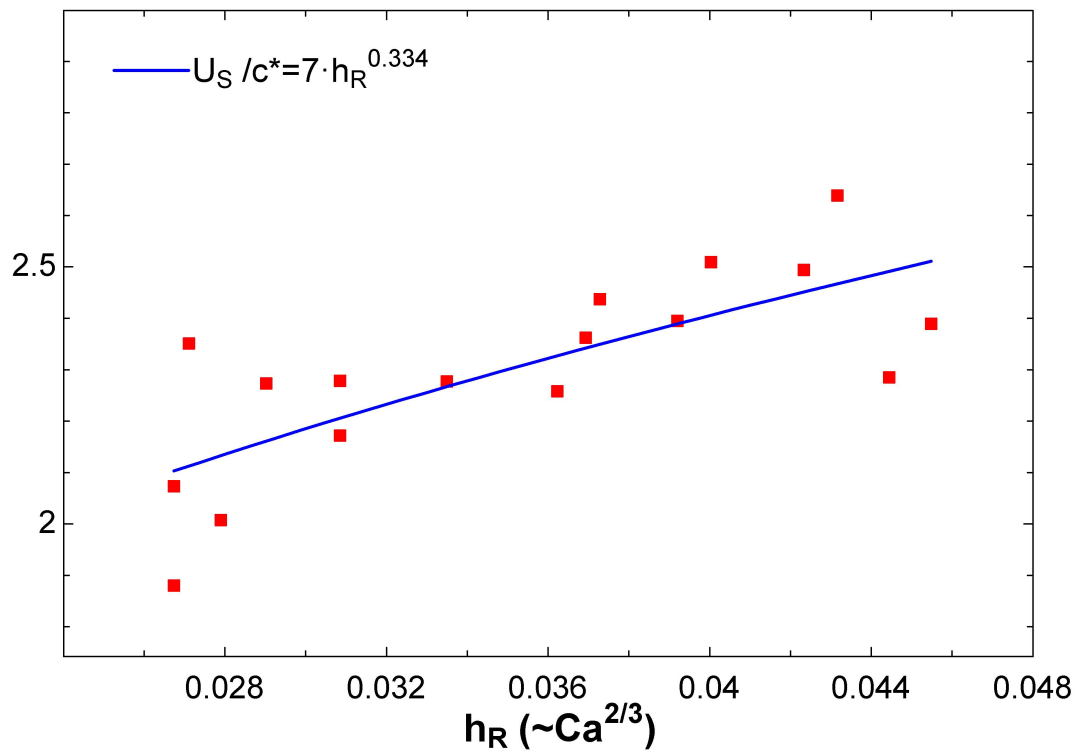
Figure 6.11. Non-dimensional Shock Velocity Correlation

now is if we can find a meaningful law to describe the film thickness variation. Eqn. 6.6 can be corroborated with the shock relations Eqns. 6.3 and 6.4 to find a relationship for the non-dimensional non-wetting film thickness, $h_{R,nonwet}$, as given in Eqn.6.7. The non-wetting film is the thicker film observed during experiments, the thin film is the wetting Bretherton film. Recall that in the hydraulic jump images 6.2 two types of films are present, a thick film towards the ridge and a thin film towards the meniscus.

$$h_{R,nonwet} \; = \; 7 \, h_R{}^{4/3} \tag{6.7}$$

This correlation as well as the measured film thickness data are plotted in Figure 6.12. The errors in the film thickness measurements are within 20% and the corresponding error bars are shown. The two leftmost data points are cases in which no hydraulic jump was observed and they fall below the shock theory film thickness law. It is apparent that the measured non-wetting film is thicker than the wetting since the data points lie above the Bretherton film thickness line. A matching curve that connects the proposed correlation with Bretherton's law may be appropriate for the sub-critical region since present correlation was derived for the super-critical region only, in which the shock velocity was measured.
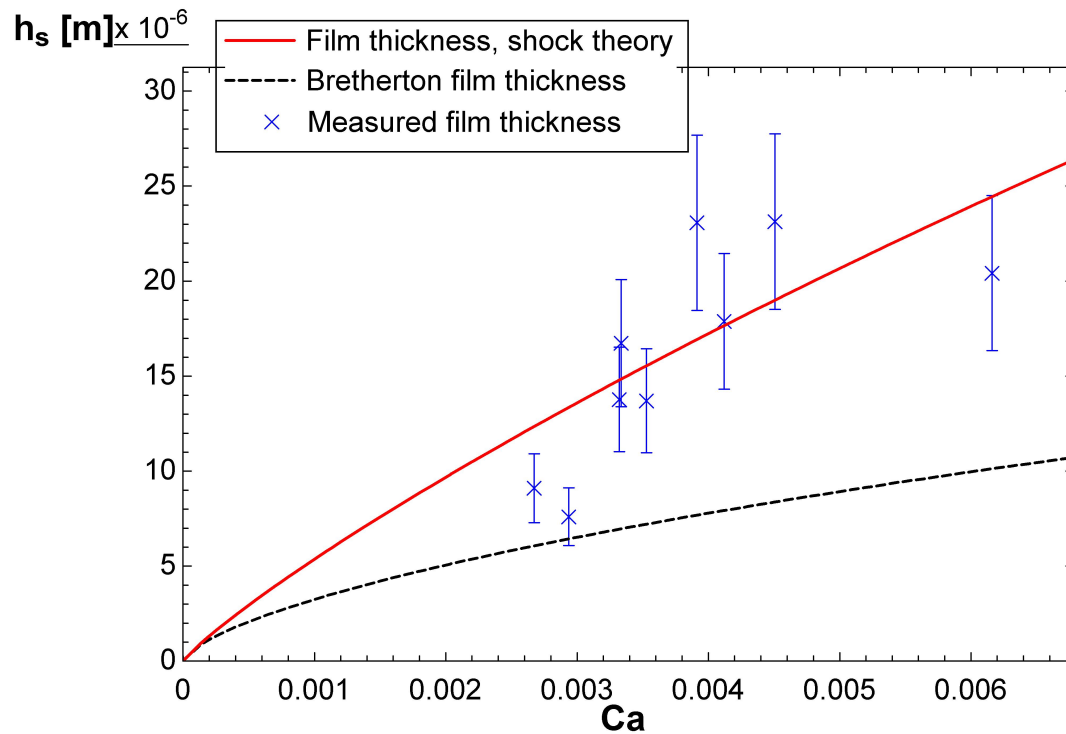
Figure 6.12. Non-wetting Film Thickness. The measured thickness follows the law obtained from the shock theory, except for the two leftmost data points which did not present a hydraulic jump. The wetting Bretherton film is shown for reference.

110

6.7　A Criterion for Shock Existence

The proposed shock theory defines a critical velocity c^* that has to be exceeded in order for the jump to occur. More specifically, the ridge *film velocity* V_2 has to be greater than the critical velocity. Let us examine the variation of the film velocity V_2 in comparison to c^*, as a function of Capillary number. V_2 can be calculated using Eqns 6.1 and 6.3, together with the film thickness correlation Eqn 6.6. As apparent in Figure 6.13 the two velocity lines V_2 and c^* intersect at Ca = 0.0025. It is important to note that although this is a critical Capillary number it will still differ depending on the system, owing to the fact that the film velocity is related to the contact line velocity. There are many factors that can change the contact line velocity and subsequently the film velocity, i.e. the contact angle or the contact line stability. Nevertheless, it happens that the film velocity is greater than the critical velocity for Ca $\geq$ 0.0025 in present experiments. However the smallest Ca at which a hydraulic jump is observed is 0.0031.

The contact line velocity relative to the meniscus, $U - U_{CL}$, is also plotted in Figure 6.13. Interestingly all the sub-critical data points lie below the c^* line. So, an *ad hoc* shock criterion could be devised as $U - U_{CL} \geq c^*$. According to the test results a hydraulic jump is always present when this criterion is satisfied. On the other hand this criterion does not state that for $U - U_{CL} < c^*$ a hydraulic jump is not possible, a few data points in this region do present a hydraulic jump. These points are relatively close to c^* and most likely belong to a transition band. More importantly, the observed behavior indicates the connection between the film and contact line velocities.
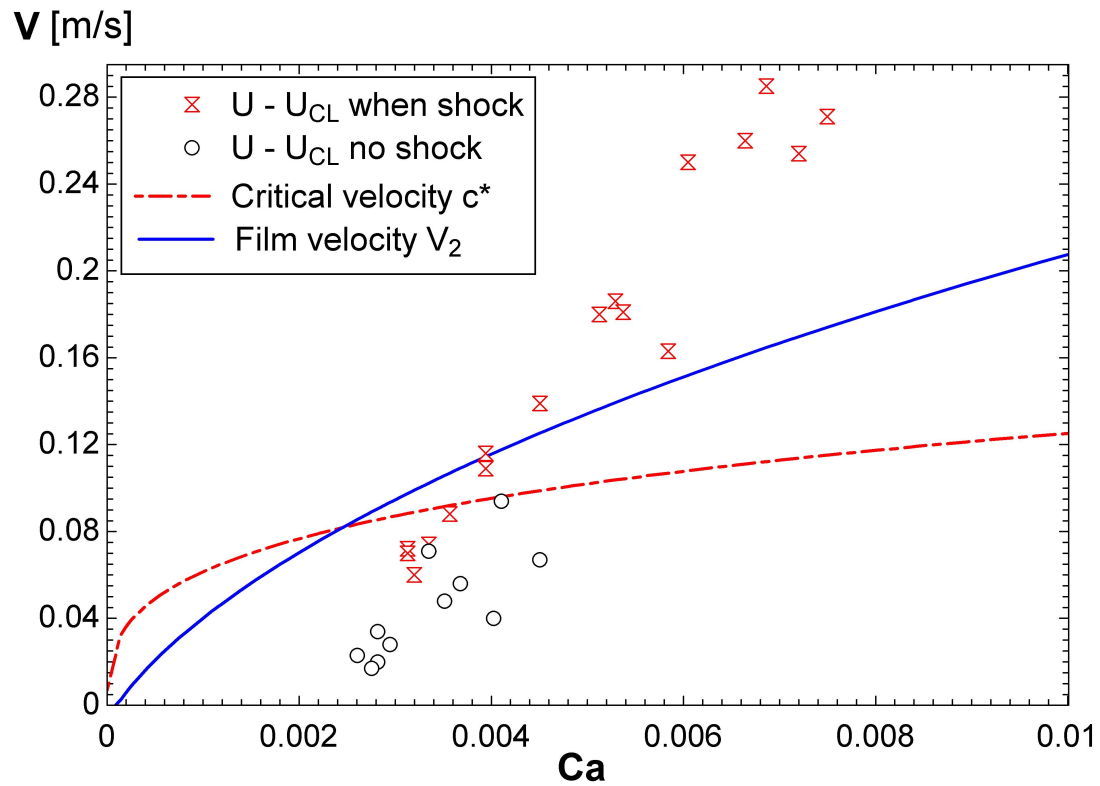
Figure 6.13. Film Velocity vs Ca. If $V_2 \geq c^*$ a hydraulic jump will occur. The relative contact line velocity data shows that a hydraulic jump always exists if $U - U_{CL} > c^*$.
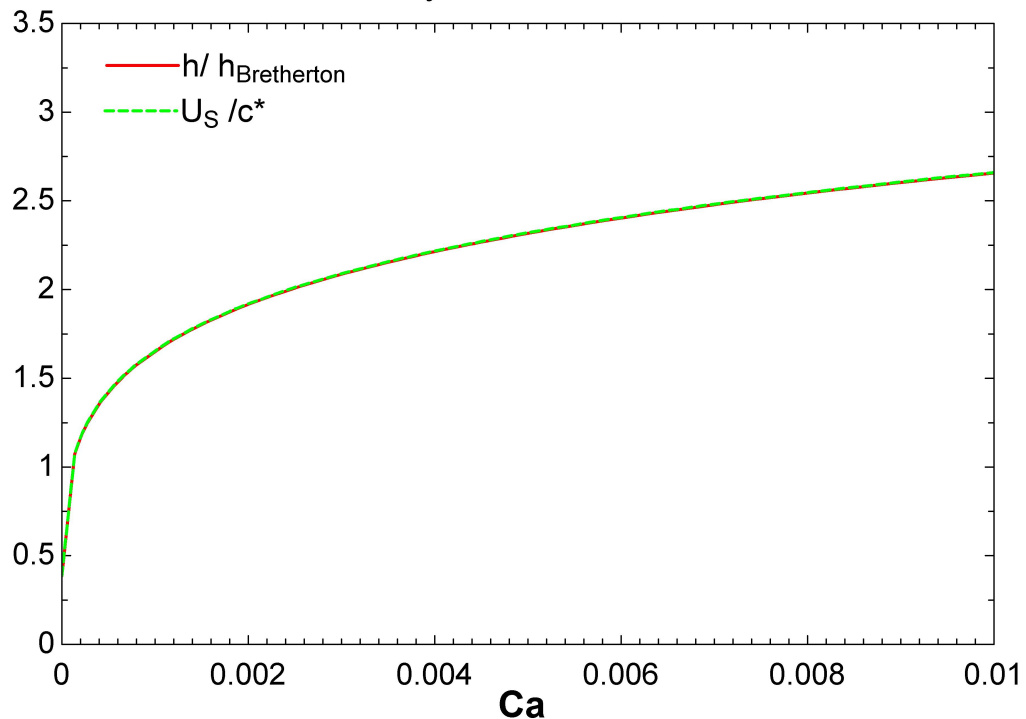
Figure 6.14. The Actual to Bretherton Film Thickness Ratio, and the Shock to Critical Velocity Ratio as a Function of Capillary Number. Note that the two lines coincide.

The influence of the contact line dynamics can be accounted for if we consider the contact line velocity relative to the meniscus rather than the film velocity in the shock criterion. We can then define a non-dimensional parameter similar to the Froude number, the non-dimensional velocity $(U - U_{\mathrm{CL}})/c^*$, which defines the border between the subcritical and supercritical regimes at a value of one. When $(U - U_{\mathrm{CL}})/c^* \geq 1$ a supercritical flow regime sets in and hydraulic jumps can be seen in the deposited film, as apparent from data plotted in Fig. 6.13. We mentioned previously at the end of Section *Hydraulic Jump Equations*, that the actual to Bretherton film thickness, $h/h_{\mathrm{Bretherton}}$, is expected to be a function of Ca. This dependence is shown

113

in Figure 6.14, notably the ratio of shock and critical velocities U_S/c^* follows the same law according to the shock relations 6.3,6.4[‡].

6.8 Critical Ca, Hydraulic Jump Formation and Taylor Bubbles

A transition Ca is now in question, if it exists it should have values between 0.00335 and 0.0045 for present non-wetting test section. However, within this range a hydraulic jump does or does not exist depending on the magnitude of the contact line velocity as can be seen in Figure 6.15. This fact suggests that even though a critical Ca may exist, the occurrence of the critical regime (hydraulic jump formation) is intimately connected to the contact line behavior. The bifurcation is clearly seen in the plot of Fig.6.15, two solutions for the contact line velocity are possible in the aforementioned Ca range: one yielding a hydraulic jump and the other not.

The bubble length as well as the film thickness present a behavior which is closely related to the existence of the hydraulic jump. Short Taylor bubbles with a thicker film are formed as long as there is no hydraulic jump, on the other hand if a hydraulic jump occurs the bubbles are longer with a thin film at the meniscus and a thicker film towards the ridge. The distance L between the contact line and the location where the hydraulic jump is first observed, as shown in Figure 6.16 does not appear to be dependent on the Capillary number and it might be regarded as a cutoff bubble length above which a hydraulic jump is observed. L varies randomly between 2.0

[‡] It can be checked independently that $h/h_{\text{Bretherton}}$ varies as U_S/c^*, if we consider the measured film thickness as h in the first ratio. The second ratio should be computed using the measured shock velocity U_S and the critical velocity c^* proposed in the shock theory.
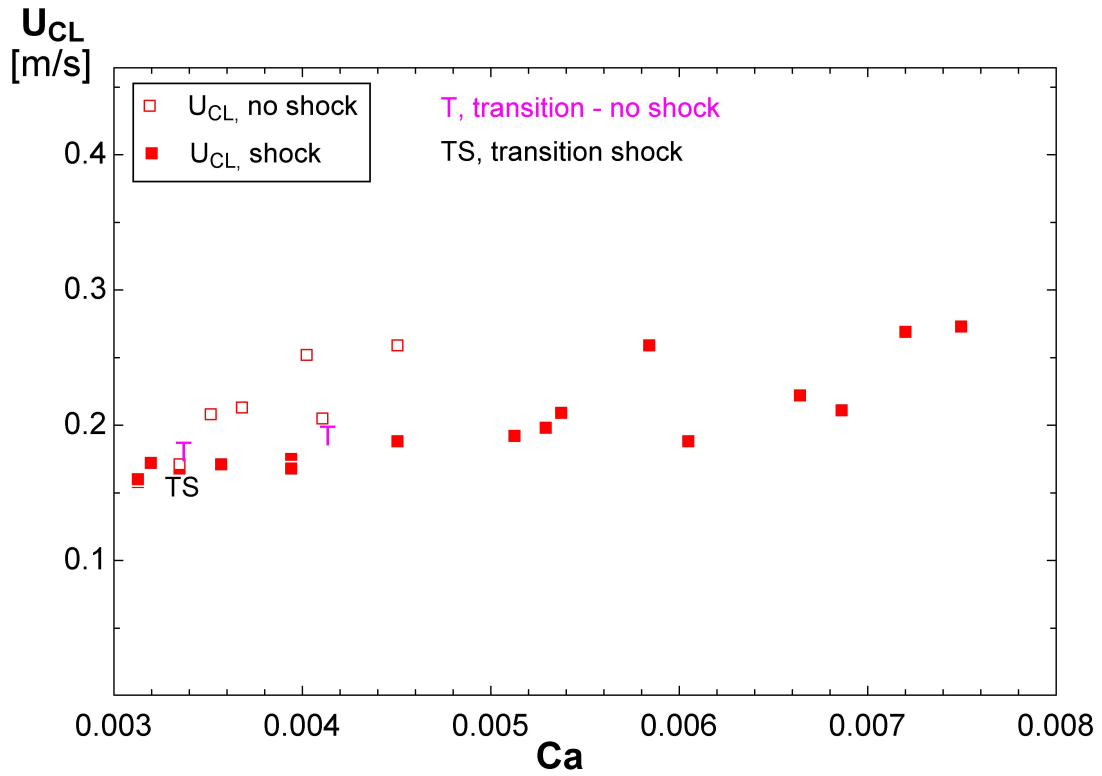
Figure 6.15. Contact Line Velocity vs. Ca. Note that for an entire Ca range the hydraulic jump may or may not exist depending on the contact line velocity.
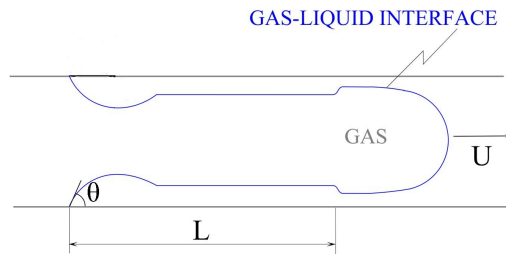
Figure 6.16. Non-Wetting Film Deposition with Hydraulic Jump

and 2.4 mm for a Capillary range between 0.0026 and 0.0075.

A discussion about two possible mechanisms which may influence the film deposition behavior feels necessary at this point. Perhaps the most notable mechanism which could cause an increased film thickness apart from the assumed contact line dynamics mechanism is contamination. Marangoni stresses can in principle cause a film thickening but it is less clear why the hydraulic jump occurs as the velocity increases, when surface tension gradients are expected to lessen in importance. The Capillary number of 0.0031 at which a hydraulic jump is first observed is rather high, the contamination effects are usually visible at much lower values. To clarify the possible contamination issue, experiments were performed in Teflon tubing (no coating applied this time) and the same behavior was observed with a hydraulic jump occurring at critical conditions. At the same time there was no hydraulic jump or film thickening in the glass tube even though the same "possibly contaminated" water was used (the water is drawn into the test section from a beaker, where it is also collected test after test) .

Another film thickening mechanism for low viscosity fluids due to inertia has been investigated by Aussillous and Quere[8] who proposed a critical Capillary number Ca* above which inertial effects become noticeable. In present non-wetting exper-

116

iments the maximum Ca is 0.0075 while Ca* $\approx$ 0.01 therefore inertial effects are not expected to significantly increase the film thickness or play a part in the shock formation.

6.9 Conclusion

Film deposition experiments performed in wetting and non-wetting tubes demonstrated that a thicker than Bretherton film is present in the latter case. A ridge bound by a moving contact line is visible at the downstream end of the deposited film. The non-wetting contact line velocity is much larger than the wetting counterpart. It is believed that the differing contact line dynamics for the two surfaces, wetting and non-wetting, cause a series of morphological changes in both the deposited film and the Taylor bubbles forming during the flow. The wetting bubbles are much longer than the non-wetting ones, the latter presenting a thicker film. Moreover, during the deposition of the non-wetting film a hydraulic jump is observed when a critical velocity is attained. If a hydraulic jump is present shorter bubbles are formed, the super-critical bubbles being longer. An analogy with the Froude shallow water wave theory suggested that the critical velocity should vary as $\sqrt{h}$ if the characteristic length is the tube radius rather than the capillary length. From a physical stand point this fact would imply that the shock mechanism for an annular non-wetting micron-thick film is capillary drainage, as opposed to gravity drainage for mm-thick planar films.

A shock theory was developed assuming that the azimuthal curvature gradient is driving the hydraulic jump. The derived critical speed follows a $\sqrt{h}$ law as pre-

117

dicted by the analogy to Froude's shock relation, while the shock velocity depends on the actual to Bretherton film thickness ratio. The non-dimensional shock velocity and the non-wetting film thickness are found to vary as $h_R^{1/3}$ and $h_R^{4/3}$, respectively (h_R being the non-dimensional Bretherton film thickness). Experimental evidence shows that the film velocity depends on the contact line velocity, and a hydraulic jump will always occur if the contact line velocity relative to the meniscus exceeds the proposed critical speed.

7. Conclusions

The critical volume of a liquid plug is computed using Surface Evolver. The minimum water volume necessary to form a plug is calculated for a range of GDL and channel wettabilities. The critical volume represents an intrinsic property of mixed wetting channels such as the gas flow channels of PEMFC and an implicit measure of the plug formation. A small critical volume plug is more likely to form under similar flow conditions, when compared to a large volume. Critical volume data can be used together with experimental data for PEMFC optimization. We also show that water can be passively removed from the GDL surface by sole means of capillary action, if the bipolar plate has a lower contact angle. This type of flow control can be used to avoid the blockage of gas reactant flow through the porous electrodes. We have to note that the existence limit was deliberately chosen over the stability limit, since the latter would require a number of different initial scenarios for water distribution making a comparison more difficult. It would be beneficial to analyze this limit as well for specific water configurations observed experimentally, this procedure would make possible further prototype-based optimization. Liquid stability and existence in various morphology can be analyzed in a similar manner, considering for example plugs spanning multiple channels or geometrically complex manifolds.

High speed microscopy was employed to study two-phase flow in micro-channels.

119

It also proved a useful tool for the study of film deposition and shock phenomena occurring in non-wetting films. An unsteady annular flow regime was observed in square microchannels and the possible existence of shock waves in the gas phase was brought into discussion. Interactions between liquid lobes and compression waves were observed using high-speed short exposure time imaging. This technique could be used with matched refraction index test sections to obtain direct film thickness measurements with improved accuracy. Other phenomena such as film rupture and dewetting, of interest for the operation of some micro-scale heat transfer devices, can also be quantified in this manner.

The effect of wettability on establishing two-phase flow morphology was also investigated by means of high speed microscopy. It is found that wetting properties play a crucial role in setting the flow regime at capillary scale, in microchannels. This fact is confirmed experimentally in the five studied cases, round and square sections with wetting ($\theta \leq 20°$) and non-wetting ($\theta = 105°$) surfaces, and a intermediate wetting case ($\theta = 80°$) in a square channel. The mixed-wetting case is a wetting case for the walls ($\theta = 80°$), but for the corners it may be de-wetting according to Concus-Finn criterion. This behavior needs to be taken into account when studying two-phase flow in polygonal geometries. For a fixed flow rate four unique flow regimes are observed proving that changes in contact angle and geometry result in distinct flow behavior. Both contact angle and geometry of the cross section need to be included in a realistic model of capillary scale two-phase flow. Future research may explore the interplay between film stability and corner flow in microchannels of varied wettabilities, and establish appropriate scaling relevant to two-phase flow regimes and transitions.

Film deposition experiments indicate that a thicker film is deposited on a surface that is not perfectly wetting. Scaling arguments suggest a non-dimensional film thickness dependence with the contact angle θ (surface wettability) as well as the Capillary number in the form $h_R \approx Ca^{2/3}/(1 - \theta^2/2)$, for relatively small contact angles up to $36°$. The effect of wettability was also investigated for a high contact angle ($\theta = 105°$) yielding a non-wetting film deposition behavior that departed significantly from the existing theories, developed under the perfect wetting assumption, $\theta = 0°$. It was found that the non-dimensional film thickness presents a weak dependence on the Capillary number having an average value of $h_R = 0.008$. Experimental observations suggest that the film stability could cause the reported behavior since film rupture occurred repeatedly in any given test run. On the other hand, film rupture or even destabilization are not observed during the wetting deposition experiments: the time scale of a Plateau-Rayleigh instability is much longer than the time required for any of the performed tests. A closer look at the film deposition process in non-wetting capillary tubes and better accuracy for film thickness measurements are desirable.

Subsequently, non-wetting experiments are carried out in order to quantify the non-dimensional film thickness dependence on surface wettability. A ridge bound by a moving contact line is observed at the downstream end of the deposited film. The non-wetting contact line velocity is much larger than the wetting counterpart. It is believed that the differing contact line dynamics for the two surfaces, wetting and non-wetting, cause a series of morphological changes in both the deposited film and the forming Taylor bubbles. The wetting bubbles are much longer than the non-wetting ones, the latter presenting a thicker film. Moreover, during the deposition of

121

the non-wetting film a shock (hydraulic jump) is observed when a critical velocity is attained. If a shock is present shorter bubbles are formed, the super-critical bubbles being longer. An analogy with the Froude shallow water wave theory suggested that the critical velocity should vary as $\sqrt{h}$ if the characteristic length is the tube radius rather than the capillary length. From a physical stand point this fact would imply that the shock mechanism for an annular non-wetting micron-thick film is capillary drainage, as opposed to gravity drainage for mm-thick planar films. A shock theory was developed assuming that the azimuthal curvature gradient is driving the shock. The derived critical speed follows a $\sqrt{h}$ law as predicted by the Froude analogy, while the shock velocity depends on the actual to Bretherton film thickness ratio. The non-dimensional shock velocity and the non-wetting film thickness are found to vary as $h_R^{1/3}$ and $h_R^{4/3}$, respectively (h_R being the non-dimensional Bretherton film thickness). Experimental evidence shows that the film velocity depends on the contact line velocity, and a shock will always occur if the contact line velocity relative to the meniscus exceeds the proposed critical speed. Improved accuracy for film thickness measurements is desirable to better establish the derived correlations. Future research is necessary to explore the contact line dynamics and its influence on film deposition processes on surfaces of varied wettability.

REFERENCES

[1] K. A. Triplett, S. M. Ghiaasiaan, S. I. Abdel-Khalik, and D. L. Sadowski. Gas-liquid two-phase flow in microchannels. Part I: two-phase flow patterns. *International Journal of Multiphase Flow*, 25(3):377–394, 1999.

[2] C. A. Damianides and J. W. Westwater. Two-phase flow patterns in a compact heat exchanger and in small tubes. page 1257, Glasgow, Scotl, 1988.

[3] A. B. Barajas and R. L. Panton. Effects of contact angle on two-phase flow in capillary tubes. *International Journal of Multiphase Flow*, 19(2):337–346, 1993.

[4] Weilin Qu, Seok-Mann Yoon, and Issam Mudawar. Two-phase flow and heat transfer in rectangular micro-channels. volume 2003 of *Proceedings of the ASME Summer Heat Transfer Conference*, pages 397–410, Las Vegas, NV, United States, 2003.

[5] Anna-Maria Morgante and Jean Fabre. Two-phase flow in square mini-channels: Flow pattern transition. volume PART A of *Proceedings of the 3rd International Conference on Microchannels and Minichannels, 2005*, pages 691–695, Toronto, ON, Canada, 2005.

[6] J. P. Owejan, T. A. Trabold, and T. W. Tighe. Hydrogen-water flow regime

123

transitions applied to anode flow phenomena in a PEMFC. volume PART A of *Proceedings of the 3rd International Conference on Microchannels and Minichannels, 2005*, pages 685–689, Toronto, ON, Canada, 2005.

[7] Severin Waelchli and Philipp Rudolf von Rohr. Two-phase flow characteristics in gas-liquid microreactors. *International Journal of Multiphase Flow*, 32(7): 791–806, 2006.

[8] P. Aussillous and D. Quere. Quick deposition of a fluid on the wall of a tube. *Physics of Fluids*, 12(10):2367–2371, 2000.

[9] I. Hassan, M. Vaillancourt, and K. Pehlivan. Two-phase flow regime transitions in microchannels: A comparative experimental study. *Microscale Thermophysical Engineering*, 9(2):165–182, 2005.

[10] John W. Coleman and Srinivas Garimella. Characterization of two-phase flow patterns in small diameter round and rectangular tubes. *International Journal of Heat and Mass Transfer*, 42(15):2869–2881, 1999.

[11] M. Kawaji and P. M. Y. Chung. Adiabatic gas-liquid flow in microchannels. *Microscale Thermophysical Engineering*, 8(3):239–257, 2004.

[12] A. Kawahara, P. M. Y. Chung, and M. Kawaji. Investigation of two-phase flow pattern, void fraction and pressure drop in a microchannel. *International Journal of Multiphase Flow*, 28(9):1411–1435, 2002.

[13] A. Tabatabai and A. Faghri. A new two-phase flow map and transition boundary accounting for surface tension effects in horizontal miniature and micro tubes. *Journal of Heat Transfer*, 123(5):958–968, 2001.

124

[14] M. K. Akbar, D. A. Plummer, and S. M. Ghiaasiaan. Gas-liquid two-phase flow regimes in microchannels. volume 372 of *American Society of Mechanical Engineers, Heat Transfer Division, (Publication) HTD*, pages 527–534, New Orleans, LA, United States, 2002.

[15] Alexandru Herescu and Jeffrey S. Allen. Wetting effects on two-phase flow in a microchannel. volume 11 PART B of *ASME International Mechanical Engineering Congress and Exposition, Proceedings*, pages 863–868, Seattle, WA, United states, 2008.

[16] A. Bazylak. Liquid water visualization in PEM fuel cells: A review. *International Journal of Hydrogen Energy*, 34(9):3845 – 3857, 2009.

[17] R. Mukundan and R.L. Borup. Visualising liquid water in PEM fuel cells using neutron imaging. *Fuel Cells*, 9(5):499 – 505, 2009.

[18] T. A. Trabold, J. P. Owejan, J. J. Gagliardo, D. L. Jacobson, D. S. Hussey, and M. Arif. *Use of neutron imaging for proton exchange membrane fuel cell (PEMFC) performance analysis and design*, chapter 44, pages 1–15. John Wiley & Sons, Ltd, 2009.

[19] Hui Li, Yanghua Tang, Zhenwei Wang, Zheng Shi, Shaohong Wu, Datong Song, Jianlu Zhang, Khalid Fatih, Jiujun Zhang, Haijiang Wang, Zhongsheng Liu, Rami Abouatallah, and Antonio Mazza. A review of water flooding issues in the proton exchange membrane fuel cell. *Journal of Power Sources*, 178(1):103 – 117, 2008.

[20] J. P. Owejan, T. A. Trabold, D. L. Jacobson, M. Arif, and S. G. Kandlikar.

Effects of flow field and diffusion layer properties on water accumulation in a PEM fuel cell. *International Journal of Hydrogen Energy*, 32(Compendex): 4489–4502, 2007.

[21] K. Brakke. Surface Evolver, Ver. 2.14, 2003.

[22] F. Fairbrother and A. E. Stubbs. Studies in electro-endosmosis. Part VI. The 'bubble-tubeŠmethod of measurement. *J. Chem. Soc*, 1:527Ű529, 1935.

[23] L. Landau and B. Levich. Dragging of a liquid by a moving plate. *Acta Physicochim. URSS*, 17:42Ű54, 1942.

[24] B. V. Derjaguin. On the thickness of a layer of liquid remaining on the walls of vessels after their emptying, and the theory of the application of photoemulsion after coating on the cine film. *Acta physico-chemica USSR*, 20:349–352, 1943.

[25] F. P. Bretherton. Motion of long bubbles in tubes. *Journal of Fluid Mechanics*, 10(Part 2):166–188, 1961.

[26] G. F. Teletzke. *Thin liquid films: molecular theory and hydrodynamic implications.* PhD thesis, University of Minnesota, 1983.

[27] J. H. Snoeijer, J. Ziegler, B. Andreotti, M. Fermigier, and J. Eggers. Thick films of viscous fluid coating a plate withdrawn from a liquid reservoir. *Physical Review Letters*, 100(24), 2008.

[28] L. W. Schwartz, H. M. Princen, and A. D. Kiss. On the motion of bubbles in capillary tubes. *Journal of Fluid Mechanics Digital Archive*, 172(-1):259–275, 1986.

[29] Alexandru Herescu and Jeffrey S. Allen. The Effect of Surface Wettability on Viscous Film Deposition. Proceedings of the 7th International ASME Conference on Nanochannels, Microchannels and Minichannels, ICNMM2009, Pohang, Korea, 2009.

[30] J. Ratulowski and H. C. Chang. Marangoni effects of trace impurities on the motion of long gas bubbles in capillaries. *Journal of Fluid Mechanics Digital Archive*, 210(1):303–328, 1990.

[31] O. O. Ramdane and D. Quere. Thickening factor in Marangoni coating. *Langmuir*, 13(11):2911–2916, 1997.

[32] R. Krechetnikov and G. M. Homsy. Surfactant effects in the LandauŰLevich problem. *Journal of Fluid Mechanics*, 559:429–450, 2006.

[33] Irfan S. Hussaini and Chao-Yang Wang. Visualization and quantification of cathode channel flooding in PEM fuel cells. *Journal of Power Sources*, 187(2): 444 – 451, 2009.

[34] Z. Lu, S.G. Kandlikar, C. Rath, M. Grimm, W. Domigan, A.D. White, M. Hardbarger, J.P. Owejan, and T.A. Trabold. Water management studies in PEM fuel cells, Part II: Ex situ investigation of flow maldistribution, pressure drop and two-phase flow pattern in gas channels. *International Journal of Hydrogen Energy*, 34(8):3445 – 3456, 2009.

[35] Li-jun Yu, Wen-can Chen, Ming-jun Qin, and Geng-po Ren. Experimental research on water management in proton exchange membrane fuel cells. *Journal of Power Sources*, 189(2):882 – 887, 2009.

127

[36] Jon P. Owejan, Jeffrey J. Gagliardo, Jacqueline M. Sergi, Satish G. Kandlikar, and Thomas A. Trabold. Water management studies in PEM fuel cells, Part I: Fuel cell design and in situ water distributions. *International Journal of Hydrogen Energy*, 34(8):3436 – 3444, 2009.

[37] Anderson. A critical review of two-phase flow in gas flow channels of proton exchange membrane fuel cells. *Journal of Power Sources*, 195(15):4531–4553., 2010.

[38] Sang Young Son and Jeffrey S. Allen. Visualization and predictive modeling of two-phase flow regime transition with application towards water management in the gas-flow channels of pem fuel cells, paper no. imece2005-82422. In *2005 ASME International Mechanical Engineering Congress and Exposition*, Orlando, Florida, 2005.

[39] Son S. Y. Allen, J. S. and S. H. Collicott. *Handbook of Fuel Cells: Advances in Electrocatalysis, Materials, Diagnostics and Durability*, volume 6, pages 687–698. Ed. Vielstich, W., Gasteiger, H.A. and Yokokawa, H., John Wiley & Sons Ltd, Chichester, UK, 2009.

[40] Paul Concus and Robert Finn. On the Behavior of a Capillary Surface in a Wedge. *Proceedings of the National Academy of Sciences of the United States of America*, 63(2):292–299, 1969.

[41] A. Bazylak, J. Heinrich, N. Djilali, and D. Sinton. Liquid water transport between graphite paper and a solid surface. *Journal of Power Sources*, 185(2): 1147–1153, 2008.

128

[42] Y. Ding, H.T. Bi, and D.P. Wilkinson. Three dimensional numerical simulation of gas-liquid two-phase flow patterns in a polymer-electrolyte membrane fuel cells gas flow channel. *Journal of Power Sources*, 196(15):6284 – 6292, 2011.

[43] Y.H. Cai, J. Hu, H.P. Ma, B.L. Yi, and H.M. Zhang. Effects of hydrophilic/hydrophobic properties on the water behavior in the micro-channels of a proton exchange membrane fuel cell. *Journal of Power Sources*, 161(2):843 – 848, 2006.

[44] Peng Quan and Ming-Chia Lai. Numerical study of water management in the air flow channel of a PEM fuel cell cathode. *Journal of Power Sources*, 164(1): 222 – 237, 2007.

[45] Zijie Lu, Cody Rath, Guangsheng Zhang, and Satish G. Kandlikar. Water management studies in PEM fuel cells, part IV: Effects of channel surface wettability, geometry and orientation on the two-phase flow in parallel gas channels. *International Journal of Hydrogen Energy*, 36(16):9864 – 9875, 2011.

[46] A. Mukherjee and J. S. Allen. Numerical study of liquid slug stability during adiabatic two phase flow inside a minichannel. In *Proc. ASME International Mechanical Engineering Congress and Exposition, IMECE 2007*, volume 8 PART B, pages 1631–1638. American Society of Mechanical Engineers, 2007.

[47] Carlos E. Colosqui, May J. Cheah, Ioannis G. Kevrekidis, and Jay B. Benziger. Droplet and slug formation in polymer electrolyte membrane fuel cell flow channels: The role of interfacial forces. *Journal of Power Sources*, 196(23):10057 – 10068, 2011.

[48] A. Herescu and J. S. Allen. Liquid holdup in the bipolar plate channels of a PEM fuel cell. *ECS Transactions*, 26(1):219–225, 2010. Fuel Cell Seminar and Exposition 2009.

[49] Steven H. Collicott, William G. Lindsley, and David G. Frazer. Zero-gravity liquid-vapor interfaces in circular cylinders. *Physics of Fluids*, 18(8), 2006.

[50] S. H. Collicott and J. P. . Braun. Stability of droplets and bubbles in a bent tube. In *44th AIAA Aerospace Sciences Meeting*, 2006.

[51] Robert Manning, Steven Collicott, and Robert Finn. Occlusion criteria in tubes under transverse body forces. *Journal of Fluid Mechanics*, 682:397–414, 2011.

[52] K. Brakke. The surface evolver. *Experimental Mathematics*, 1(2):141–165, 1992.

[53] J. Roth. *Water Transport in Gas Diffusion Media for PEM Fuel Cells: Experimental and Numerical Investigation*. PhD thesis, Universität Duisburg-Essen, 2010.

[54] E.B. Dussan V. On the Spreading of Liquids on Solid Surfaces: Static and Dynamic Contact Lines. *Annual Review of Fluid Mechanics*, 11:371–400, 1979.

[55] M. M. Weislogel and S. Lichter. Capillary flow in an interior corner. *Journal of Fluid Mechanics*, 373:349–378, 1998.

[56] M. M. Weislogel and C. L. Nardin. Capillary driven flow along interior corners formed by planar walls of varying wettability. *Microgravity Science and Technology*, 17(3):45–55, 2005.

[57] Erin Kimball, Tamara Whitaker, Yannis G. Kevrekidis, and Jay B. Benziger. Drops, slugs, and flooding in polymer electrolyte membrane fuel cells. *AIChE Journal*, 54(5):1313–1332, 2008.

[58] P. G. De Gennes, F. Brochard-Wyart, D. Quere, and A. Reisinger. *Capillarity and wetting phenomena: drops, bubbles, pearls, waves*. Springer Verlag, 2004.

[59] C. Y. Lee and S. Y. Lee. Pressure drop of two-phase plug flow in round mini-channels: Influence of surface wettability. *Experimental Thermal and Fluid Science*, 32(8):1716–1722, 2008.

[60] C. Y. Lee and S. Y. Lee. Pressure drop of two-phase dry-plug flow in round mini-channels: Effect of moving contact line. *Experimental Thermal and Fluid Science*, 34(1):1–9, 2010.

[61] P. S. Hammond. Nonlinear adjustment of a thin annular film of viscous fluid surrounding a thread of another within a circular cylindrical pipe. *J. Fluid Mechanics*, 137:363–384, 1983.

[62] T. C. Ransohoff, P.A. Gauglitz, and C.J. Radke. Snap-off of gas bubbles in smoothly constricted noncircular capillaries. *AIChE J.*, 33(5):753–765, 1987.

[63] S. L. Goren. The instability of an annular thread of fluid. *J. Fluid Mechanics*, 12:309–319, 1962.

[64] H. H. Hu and D. D. Joseph. Lubricating pipelining: Stability of core-annular flow. part 2. *Journal of Fluid Mechanics*, 205:359–396, 1989.

[65] P.A. Gauglitz and C.J. Radke. The dynamics of liquid film breakup in constricted cylindrical capillaries. *Journal of Colloid and Interface Science*, 134 (1):14–40, 1990.

[66] D. H. Everett and J. M. Haynes. Model studies of capillary condensation; 1. cylindrical pore model with zero contact angle. *J. Colloid and Interface Science*, 38(1):125–137, 1972.

[67] F. A. de Bruijn, V. A. T. Dam, and G. J. M. Janssen. Review: Durability and Degradation Issues of PEM Fuel Cell Components. *Fuel Cells*, 8(1):3–22, 2008.

[68] Jeffrey S. Allen, Sang Young Son, and Kenneth D. Kihm. Characterization and control of two-phase flow in microchannels (pem fuel cell channels and manifolds) research for design annual report. Technical report, National Center for Microgravity Research, November 2003.

[69] James J. Kriegsmann, Michael J. Miksis, and Jean-Marc Vanden-Broeck. Pressure driven disturbances on a thin viscous film. *Physics of Fluids*, 10(6):1249–1255, 1998.

[70] R.M. Pols, S. Hibberd, and B.J. Azzopardi. Discontinuous wave solutions in stratified and annular two-phase flows. In *Third International Conference on Multiphase Flow (ICMFi98)*, Lyon, France, 1998.

[71] Sang Young Son, Jeffrey S. Allen, and Kenneth D. Kihm. Low bond number two-phase flow regime transition from slug to annular wavy flow in a microchannel," journal of heat transfer, vol. 125, issue 4, pp. 544. *Journal of Heat Transfer*, 125(4):544, 2003.

132

[72] Jeffrey S. Allen and Sang Young Son. Observation of low bond number two-phase flow regime transition from slug to annular wavy flow in a microchannel, April 24-25 2003.

[73] Shoji and Esashi. Microflow devices and systems. *Journal of Micromechanics and Microengineering*, 4(4):157–171, 1994.

[74] Gravesen, Branebjerg, and Jensen. Microfluidics - a review. *Journal of Micromechanics and Microengineering*, 3(4):168–182, 1993.

[75] Strook-Abraham D. Stone, H.A. and A. Ajdari. Engineering flows in small devices: Microfluidics toward a lab-on-a-chip. *Annual Review of Fluid Mechanics*, 36:381–411, 2004.

[76] Todd M. Quake and Stephen R. Squires. Microfluidics: Fluid physics at the nanoliter scale. *Reviews of Modern Physics*, 77:977–1026, 2005.

[77] Elisabeth M. J. Verpoorte, Bart H. van der Schoot, Sylvain Jeanneret, Andreas Manz, H. M. Widmer, and Nico F. de Rooij. Three-dimensional micro flow manifolds for miniaturized chemical analysis systems. *Journal of Micromechanics and Microengineering*, 4:246–256, 1994.

[78] T.A. Trabold. Minichannels in polymer electrolyte membrane fuel cells. *Heat Transfer Engineering*, 26(3):1–10, 2005.

[79] Suo and Griffith. Two-phase flow in capillary tubes. *Journal of Basic Engineering*, 86:576–582, 1964.

133

[80] Jaydeep Biswas and P. F. Geenfield. A two phase flow through vertical capillaries - existence of a stratified flow pattern. *International Journal of Multiphase Flow*, 11(4):553–563, 1985.

[81] Killion Garimella and Coleman. An experimentally validated model for two-phase pressure drop in the intermittent flow regime for circular microchannels. *Journal of Fluids Engineering, Transactions of the ASME*, 124:205–214, 2002.

[82] K. Mishima and T. Hibiki. Some characteristics of air-water two-phase flow in small diameter vertical tubes. *International Journal of Multiphase Flow*, 22(4): 703–712, 1996.

[83] Dreyer Wölk and Hans. Flow patterns in small diameter vertical non-circular channels. *International Journal of Multiphase Flow*, 26(6):1037–1061, 2000.

[84] J. L. Xu, P. Cheng, and T. S. Zhao. Gas-liquid two-phase flow regimes in rectangular channels with mini/micro gaps. *International Journal of Multiphase Flow*, 25:411–432, 1999.

[85] T. S. Zhao and Q. C. Bi. Co-current air-water two-phase flow patterns in vertical triangular microchannels. *International Journal of Multiphase Flow*, 27 (5):765–782, 2001.

[86] J. S. Allen. Two-phase flow in small channels and the implications for pem fuel cell operation. In *210th Meeting of The Electrochemical Society*, 2006.

[87] Miksis Zhang and Bankoff. Nonlinear dynamics of a two-dimensional viscous drop under shear flow. *Physics of Fluids*, 18(072106):1–10, 2006.

[88] M. L. Minges. *Electronic materials handbook packaging, vol. 1*. ASM International, 1989.

[89] Jacco H. Snoeijer, Giles Delon, Marc Fermigier, and Bruno Andreotti. Avoided critical behavior in dynamically forced wetting. *Physical Review Letters*, 96(17): 174504, 2006.

APPENDICES

Appendix A

Contact Angle Formulation In Surface Evolver
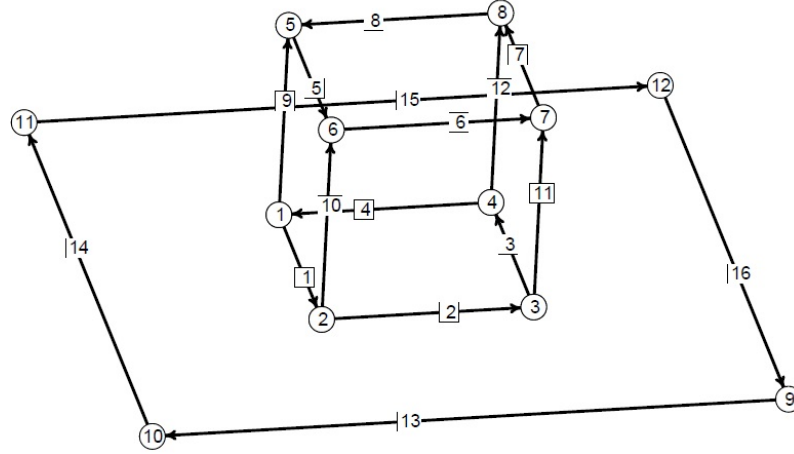
Figure 0.1. Surface Evolver Droplet Model.

A Surface Evolver model of a droplet sitting on a plane surface is shown in Figure 0.1. The initial liquid configuration is a cube described by the vertices 1 through 8, and the corresponding oriented edges and faces. The face number 6 on the horizontal plane is given by 1->2->3->4. The energy density of the faces 1 - 5 is one and the energy on the face 6 should have a value different than one such that the surface tension balance on the contact line 1->2->3->4 is satisfied. Therefore the virtual tension of the facet on the plane is $T = -cos((angle) * pi/180)$, where "angle" is the contact angle.

To avoid convergence issues, facet 6 is removed and the corresponding energy is assigned to the bordering edges 1, 2, 3 and 4. This energy can be calculated in SE through an energy line integral, as long as an appropriate energy formulation is found. We are looking therefore for a vector field $\mathbf{w}$ such that $\iint_{face6} T\hat{k} \cdot d\mathbf{S} =$

```
#define WALLT  (-cos(angle*pi/180)) // virtual tension of facet on plane


constraint 1   /* the table top */

formula: x3 = 0

energy: // for contact angle

e1: -(WALLT*y)

e2: 0

e3: 0
```

Figure 0.2. Contact Angle As A Surface Energy Constraint.

$\int_{\partial face6} \mathbf{w} \cdot d\mathbf{l}$, where $\hat{j}$ and $\hat{k}$ are the y and z axes unit vectors. According to Green's theorem we find $\mathbf{w} = -Ty\hat{i}$. We can now implement the contact angle as an energy constraint in the plane $z = 0$, as shown in the code facsimile in Figure 0.2. This constraint has to be satisfied at vertices 1 - 4 and the corresponding edges in the horizontal plane. For more SE examples and a comprehensive tutorial the reader is referred to Brakke [21].

Appendix B

Copyright Agreements

The following letter pertains to *Chapter 2.*

ELSEVIER LICENSE
TERMS AND CONDITIONS

Apr 01, 2013

This is a License Agreement between Alexandru Herescu ("You") and Elsevier ("Elsevier") provided by Copyright Clearance Center ("CCC"). The license consists of your order details, the terms and conditions provided by Elsevier, and the payment terms and conditions.

All payments must be made in full to CCC. For payment instructions, please see information listed at the bottom of this form.

Supplier	Elsevier Limited The Boulevard,Langford Lane Kidlington,Oxford,OX5 1GB,UK
Registered Company Number	1982084
Customer name	Alexandru Herescu
Customer address	300 W Pier Dr.
	Sault Ste Marie, MI 49783
License number	3120361475932
License date	Apr 01, 2013
Licensed content publisher	Elsevier
Licensed content publication	Journal of Power Sources
Licensed content title	The influence of channel wettability and geometry on water plug formation and drop location in a proton exchange membrane fuel cell flow field
Licensed content author	Alexandru Herescu,Jeffrey S. Allen
Licensed content date	15 October 2012
Licensed content volume number	216
Licensed content issue number	
Number of pages	8
Start Page	337
End Page	344
Type of Use	reuse in a thesis/dissertation
Portion	full article
Format	both print and electronic
Are you the author of this Elsevier article?	Yes
Will you be translating?	No

143

Order reference number

Title of your thesis/dissertation	Two Phase Flow in Microchannels: Morphology and Interface Phenomena
Expected completion date	Apr 2013
Estimated size (number of pages)	135
Elsevier VAT number	GB 494 6272 12
Permissions price	0.00 USD
VAT/Local Sales Tax	0.0 USD / 0.0 GBP
Total	0.00 USD

Terms and Conditions

INTRODUCTION

1. The publisher for this copyrighted material is Elsevier. By clicking "accept" in connection with completing this licensing transaction, you agree that the following terms and conditions apply to this transaction (along with the Billing and Payment terms and conditions established by Copyright Clearance Center, Inc. ("CCC"), at the time that you opened your Rightslink account and that are available at any time at http://myaccount.copyright.com).

GENERAL TERMS

2. Elsevier hereby grants you permission to reproduce the aforementioned material subject to the terms and conditions indicated.

3. Acknowledgement: If any part of the material to be used (for example, figures) has appeared in our publication with credit or acknowledgement to another source, permission must also be sought from that source. If such permission is not obtained then that material may not be included in your publication/copies. Suitable acknowledgement to the source must be made, either as a footnote or in a reference list at the end of your publication, as follows:

"Reprinted from Publication title, Vol /edition number, Author(s), Title of article / title of chapter, Pages No., Copyright (Year), with permission from Elsevier [OR APPLICABLE SOCIETY COPYRIGHT OWNER]." Also Lancet special credit - "Reprinted from The Lancet, Vol. number, Author(s), Title of article, Pages No., Copyright (Year), with permission from Elsevier."

4. Reproduction of this material is confined to the purpose and/or media for which permission is hereby given.

5. Altering/Modifying Material: Not Permitted. However figures and illustrations may be altered/adapted minimally to serve your work. Any other abbreviations, additions, deletions and/or any other alterations shall be made only with prior written authorization of Elsevier Ltd. (Please contact Elsevier at permissions@elsevier.com)

6. If the permission fee for the requested use of our material is waived in this instance, please be advised that your future requests for Elsevier materials may attract a fee.

7. Reservation of Rights: Publisher reserves all rights not specifically granted in the combination of (i) the license details provided by you and accepted in the course of this licensing transaction, (ii) these terms and conditions and (iii) CCC's Billing and Payment terms and conditions.

8. License Contingent Upon Payment: While you may exercise the rights licensed immediately upon issuance of the license at the end of the licensing process for the transaction, provided that you have disclosed complete and accurate details of your proposed use, no license is finally effective unless and until full payment is received from you (either by publisher or by CCC) as provided in CCC's Billing and Payment terms and conditions. If full payment is not received on a timely basis, then any license preliminarily granted shall be deemed automatically revoked and shall be void as if never granted. Further, in the event that you breach any of these terms and conditions or any of CCC's Billing and Payment terms and conditions, the license is automatically revoked and shall be void as if never granted. Use of materials as described in a revoked license, as well as any use of the materials beyond the scope of an unrevoked license, may constitute copyright infringement and publisher reserves the right to take any and all action to protect its copyright in the materials.

9. Warranties: Publisher makes no representations or warranties with respect to the licensed material.

10. Indemnity: You hereby indemnify and agree to hold harmless publisher and CCC, and their respective officers, directors, employees and agents, from and against any and all claims arising out of your use of the licensed material other than as specifically authorized pursuant to this license.

11. No Transfer of License: This license is personal to you and may not be sublicensed, assigned, or transferred by you to any other person without publisher's written permission.

12. No Amendment Except in Writing: This license may not be amended except in a writing signed by both parties (or, in the case of publisher, by CCC on publisher's behalf).

13. Objection to Contrary Terms: Publisher hereby objects to any terms contained in any purchase order, acknowledgment, check endorsement or other writing prepared by you, which terms are inconsistent with these terms and conditions or CCC's Billing and Payment terms and conditions. These terms and conditions, together with CCC's Billing and Payment terms and conditions (which are incorporated herein), comprise the entire agreement between you and publisher (and CCC) concerning this licensing transaction. In the event of any conflict between your obligations established by these terms and conditions and those established by CCC's Billing and Payment terms and conditions, these terms and conditions shall control.

14. Revocation: Elsevier or Copyright Clearance Center may deny the permissions described in this License at their sole discretion, for any reason or no reason, with a full refund payable to you. Notice of such denial will be made using the contact information provided by you. Failure to receive such notice will not alter or invalidate the denial. In no event will Elsevier or Copyright Clearance Center be responsible or liable for any costs, expenses or damage incurred by you as a result of a denial of your permission request, other than a refund of the amount(s) paid by you to Elsevier and/or Copyright Clearance Center for denied permissions.

LIMITED LICENSE

145

The following terms and conditions apply only to specific license types:

15. **Translation**: This permission is granted for non-exclusive world **English** rights only unless your license was granted for translation rights. If you licensed translation rights you may only translate this content into the languages you requested. A professional translator must perform all translations and reproduce the content word for word preserving the integrity of the article. If this license is to re-use 1 or 2 figures then permission is granted for non-exclusive world rights in all languages.

16. **Website**: The following terms and conditions apply to electronic reserve and author websites:
Electronic reserve: If licensed material is to be posted to website, the web site is to be password-protected and made available only to bona fide students registered on a relevant course if:
This license was made in connection with a course,
This permission is granted for 1 year only. You may obtain a license for future website posting,
All content posted to the web site must maintain the copyright information line on the bottom of each image,
A hyper-text must be included to the Homepage of the journal from which you are licensing at http://www.sciencedirect.com/science/journal/xxxxx or the Elsevier homepage for books at http://www.elsevier.com , and
Central Storage: This license does not include permission for a scanned version of the material to be stored in a central repository such as that provided by Heron/XanEdu.

17. **Author website** for journals with the following additional clauses:

All content posted to the web site must maintain the copyright information line on the bottom of each image, and the permission granted is limited to the personal version of your paper. You are not allowed to download and post the published electronic version of your article (whether PDF or HTML, proof or final version), nor may you scan the printed edition to create an electronic version. A hyper-text must be included to the Homepage of the journal from which you are licensing at http://www.sciencedirect.com/science/journal/xxxxx . As part of our normal production process, you will receive an e-mail notice when your article appears on Elsevier's online service ScienceDirect (www.sciencedirect.com). That e-mail will include the article's Digital Object Identifier (DOI). This number provides the electronic link to the published article and should be included in the posting of your personal version. We ask that you wait until you receive this e-mail and have the DOI to do any posting.

Central Storage: This license does not include permission for a scanned version of the material to be stored in a central repository such as that provided by Heron/XanEdu.

18. **Author website** for books with the following additional clauses:
Authors are permitted to place a brief summary of their work online only.
A hyper-text must be included to the Elsevier homepage at http://www.elsevier.com . All content posted to the web site must maintain the copyright information line on the bottom of each image.
You are not allowed to download and post the published electronic version of your chapter, nor may you scan the printed edition to create an electronic version.

Central Storage: This license does not include permission for a scanned version of the material to be stored in a central repository such as that provided by Heron/XanEdu.

19. **Website** (regular and for author): A hyper-text must be included to the Homepage of the journal from which you are licensing at http://www.sciencedirect.com/science/journal/xxxxx. or for books to the Elsevier homepage at http://www.elsevier.com

20. **Thesis/Dissertation**: If your license is for use in a thesis/dissertation your thesis may be submitted to your institution in either print or electronic form. Should your thesis be published commercially, please reapply for permission. These requirements include permission for the Library and Archives of Canada to supply single copies, on demand, of the complete thesis and include permission for UMI to supply single copies, on demand, of the complete thesis. Should your thesis be published commercially, please reapply for permission.

21. **Other Conditions**:

v1.6

The following letter pertains to *Chapter 3, Section 4.2* and *Chapter 5.*

LAKE SUPERIOR
STATE UNIVERSITY

Alexandru Herescu <aherescu@lssu.edu>

Fwd: FW: ASME PUBLICATIONS PERMISSION REQUEST FORM SUBMISSION
2 messages

Alexandru Herescu <aherescu@mtu.edu>   Wed, Mar 27, 2013 at 8:17 PM
To: aherescu@lssu.edu

————— Forwarded message —————
From: **Beth Darchi** <DarchiB@asme.org>
Date: Wed, Mar 14, 2012 at 11:38 AM
Subject: FW: ASME PUBLICATIONS PERMISSION REQUEST FORM SUBMISSION
To: "aherescu@mtu.edu" <aherescu@mtu.edu>

Dear Mr. Herescu:

It is our pleasure to grant you permission to use the following ASME materials:

- "Periodic Interface Destabilization in High-Speed Gas-Liquid Flows at the Capillary Scale,"by Alexandru Herescu, Jeffrey S. Allen, Proceedings of The Fourth International Conference on Nanochannels, Microchannels and Minichannels, Paper Number ICNMM2006-96183

- "Compressibility Effects in the Gas Phase for Unsteady Annular Two-Phase Flow in a Microchannel," by Alexandru Herescu, Jeffrey S. Allen, Proceedings of the ASME International Mechanical Engineering Congress and Exposition, Fluids Engineering Division, Paper Number IMECE2006-15528,

- "Wetting Effects on Two-Phase Flow in a Microchannel," by Alexandru Herescu, Jeffrey S. Allen, Proceedings of the ASME International Mechanical Engineering Congress and Exposition, Fluids Engineering Division, Paper Number IMECE2007-42050

- "The Effect of Surface Wettability on Viscous Film Deposition," by Alexandru Herescu, Jeffrey S. Allen, Proceedings of The Seventh International Conference on Nanochannels, Microchannels and Minichannels, Paper Number ICNMM2009-82263

- "Implications of Contact Line Dynamics on Taylor Bubble Flow Morphology," by Alexandru Herescu, Jeffrey S. Allen, Proceedings The Eighth International Conference on Nanochannels, Microchannels and Minichannels, Paper Number FEDSM-ICNMM2010-30911

cited in your letter for inclusion in a Doctoral Thesis entitled <u>Two-phase Flow in Microchannels: Morphology and Interface Phenomena</u> to be published by ProQuest/ UMI Dissertation Services.

149

As is customary, we ask that you ensure full acknowledgment of this material, the author(s), source and ASME as original publisher on all printed copies being distributed.

Many thanks for your interest in ASME publications.

Sincerely,

Beth Darchi

Permissions & Copyrights

ASME, 3 Park Avenue

New York, NY 10016

T: 212-591-7700

F: 212-591-7841

E: darchib@asme.org

——Original Message——
From: webmaster@asme.org [mailto:webmaster@asme.org]
Sent: Tuesday, March 13, 2012 2:27 PM
To: permissions@asme.org
Cc: aherescu@mtu.edu
Subject: ASME PUBLICATIONS PERMISSION REQUEST FORM SUBMISSION

ASME PUBLICATIONS PERMISSION REQUEST FORM HAS BEEN SUBMITTED:

ASME Publication Title: Proceedings of The Fourth International Conference on Nanochannels, Microchannels and Minichannels, June 19-21, 2006, Limerick, Ireland

Complete List of Authors: Alexandru Herescu, Jeffrey S. Allen

Paper Title (Conference/Journal): Periodic Interface Destabilization in High-Speed Gas-Liquid Flows at the Capillary Scale

Paper Number (Conference):   ICNMM2006-96183

Volume Number (Journal):   0

150

Page(s) in the publication of

the permission request:

Year of Publication: 2006

I would like to... Republish in a Doctoral Thesis

Portion to be used: Entire Article

List Figure Numbers: 0

List Table Numbers: 0

Number of Copies:

Usage: Both

Title of outside publication: Two-phase Flow in Microchannels: Morphology and Interface Phenomena

Publisher: ProQuest/ UMI Dissertation Services

Comments: Thank you!

Author: yes

First Name: Alexandru

Last Name: Herescu

Address Line 1: 1911 A Woodmar Dr.

Address Line 2:

City: Houghton

State: MI

Zip: 49931

Phone: 906-483-8248

Fax:

Email: aherescu@mtu.edu

ASME PUBLICATIONS PERMISSION REQUEST FORM HAS BEEN SUBMITTED:

ASME Publication Title: Proceedings of the ASME International Mechanical Engineering Congress and Exposition, Fluids Engineering Division, November 5-10, 2006, Chicago, Illinois

Complete List of Authors: Alexandru Herescu, Jeffrey S. Allen

Paper Title (Conference/Journal): Compressibility Effects in the Gas Phase for Unsteady Annular Two-Phase

Flow in a Microchannel

Paper Number (Conference):   IMECE2006-15528

Volume Number (Journal):   0

Page(s) in the publication of

the permission request:

Year of Publication: 2006

I would like to...   Republish in a Doctoral Thesis

Portion to be used: Entire Article

List Figure Numbers: 0

List Table Numbers: 0

Number of Copies:

Usage: Both

Title of outside publication: Two-phase Flow in Microchannels: Morphology and Interface Phenomena

Publisher: ProQuest/ UMI

Comments: Thank you!

Author: yes

First Name: Alexandru

Last Name: Herescu

Address Line 1:   1911 A Woodmar Dr

Address Line 2:

City: Houghton

State: MI

Zip: 49931

Phone: 906-483-8248

Fax:

Email: aherescu@mtu.edu

ASME PUBLICATIONS PERMISSION REQUEST FORM HAS BEEN SUBMITTED:

ASME Publication Title: Proceedings of the ASME International Mechanical Engineering Congress and

Exposition, Fluids Engineering Division, November 11-15, 2007, Seattle, Washington.

Complete List of Authors: Alexandru Herescu, Jeffrey S. Allen

Paper Title (Conference/Journal): Wetting Effects on Two-Phase Flow in a Microchannel

Paper Number (Conference):   IMECE2007-42050

Volume Number (Journal):   0

Page(s) in the publication of

the permission request:

Year of Publication: 2007

I would like to...   Republish in a Doctoral Thesis

Portion to be used: Entire Article

List Figure Numbers: 0

List Table Numbers: 0

Number of Copies:

Usage: Both

Title of outside publication: Two-phase Flow in Microchannels: Morphology and Interface Phenomena

Publisher: ProQuest/ UMI

Comments: Thank you!

Author: yes

First Name: Alexandru

Last Name: Herescu

Address Line 1:   1911 A Woodmar Dr

Address Line 2:

City: Houghton

State: MI

Zip: 49931

Phone: 906-483-8248

Fax:

Email: aherescu@mtu.edu

ASME PUBLICATIONS PERMISSION REQUEST FORM HAS BEEN SUBMITTED:

ASME Publication Title: Proceedings of The Seventh International Conference on Nanochannels, Microchannels and Minichannels, June 22-24, 2009, Pohang, South Korea.

Complete List of Authors: Alexandru Herescu, Jeffrey S. Allen

Paper Title (Conference/Journal): The Effect of Surface Wettability on Viscous Film Deposition

Paper Number (Conference):   ICNMM2009-82263

Volume Number (Journal):   0

Page(s) in the publication of

the permission request:

Year of Publication: 2009

I would like to...   Republish in a Doctoral Thesis

Portion to be used: Entire Article

List Figure Numbers: 0

List Table Numbers: 0

Number of Copies:

Usage: Both

Title of outside publication: Two-phase Flow in Microchannels: Morphology and Interface Phenomena

Publisher: ProQuest/ UMI

Comments: Thank you!

Author: yes

First Name: Alexandru

Last Name: Herescu

Address Line 1:   1911 A Woodmar Dr

Address Line 2:

City: Houghton

State: MI

Zip: 49931

Phone: 906-483-8248

Fax:

Email: aherescu@mtu.edu

154